Field layout and dispatch optimisation strategies for a concentrating solar thermal plant providing high-temperature process heat

by
Tristan Mckechnie

Thesis presented in partial fulfilment of the requirements for the degree of Master of Engineering (Mechanical) in the Faculty of Engineering at Stellenbosch University

Supervisor: Prof. Craig McGregor
Co-supervisor: Prof. Gerhard Venter

March 2021

Declaration

By submitting this thesis electronically, I declare that the entirety of the work contained therein is my own, original work, that I am the sole author thereof (save to the extent explicitly otherwise stated), that reproduction and publication thereof by Stellenbosch University will not infringe any third party rights and that I have not previously in its entirety or in part submitted it for obtaining any qualification.

Date: March 2021

Abstract

The world is moving towards a more environmentally sustainable future. To achieve this energy intensive sectors must transition to sustainable, alternative energy sources. The high-temperature industrial process heat sector relies heavily on fossil fuel combustion for their energy needs. A potential sustainable alternative to this is concentrating solar technologies, which have proven capabilities of providing high-temperature energy without the emission of Green House Gases. In this thesis concentrating solar technologies are investigated for application in the high-temperature industrial process heat sector. Next generation concentrating solar technology utilising ceramic particles as the heat transfer medium and a central receiver reflector system, are capable of reaching temperatures in excess of 1 000 °C. In this thesis, these technologies are investigated around the concept of a concentrating solar plant providing high-temperature process heat for Manganese ore pre-heating, prior to smelting.

In order to evaluate the concept an optical, energy and economic model is developed for the concentrating solar plant. From these models, optimisation studies are performed to determine optimal plant operation and heliostat field layouts, to design a plant which provides the required heat at lowest cost. The plant utilises electric backup heaters to ensure a steady heat supply to the ore pre-heater. This occurs in the context of a time-of-use electric tariff. The plant's operating strategy is determined using an optimal thermal energy storage dispatch profile which ensures backup electric heat is purchased for least cost. It is shown that the optimal dispatch profile reduces the cost of the plant's supplied heat from 43.03 $\$/\mathrm{MWh_{th}}$ to 37.96 $\$/\mathrm{MWh_{th}}$, compared to an heuristic strategy. A novel heliostat technology, the HelioPod™ which has six heliostats fixed on a common base structure, is used in this work. This technology has not been extensively studied for application in the large field sizes required for this work. An optimisation study of HelioPod™ field layouts is undertaken to determine how to design the field layout to deliver the required energy with the lowest number of heliostats. This work adapts the existing optimised field layout knowledge from literature, based on individual heliostat fields, to pod fields. It was found that the plant's tower height significantly influences the field design. For a shorter tower height a more sophisticated layout is required to reduce blocking and shading optical losses. For this shorter tower the optimised HelioPod™ field layout developed improved the plant's economic performance by 11.18 % compared to an heuristic layout.

A case study for a Manganese smelter with concentrating solar derived process heat for ore pre-heating was developed. The case study investigated a smelter located in the Northern Cape of South Africa. The region has world class solar resource, as well as the largest land based Manganese ore reserves in the world. The concentrating solar plant in this case study was capable of providing process heat at lower cost than diesel combustion, but at nearly double the cost of coal combustion. However if the current trend for concentrating solar cost reduction continues, the technology could reach cost parity with coal in the future.

Uittreksel

Tans is daar ‘n globale beweging na ‘n meer omgewings volhoubare toekoms. Ten einde dit te bereik, vereis dit die oorskakeling van energie-intensiewe sektore na volhoubare, alternatiewe bronne van energie. Industrië in die hoë temperatuur hitte prosessering sektor is hoofsaaklik afhanklik van fosielbrandstof vir die ontwikkeling van hulle energiebehoeftes. ‘n Potensiele volhoubare alternatief hiervoor is sonkragkonsentrasie tegnologie wat alreeds bewys gelewer het van die vermoë om hoë temperatuur energie te verskaf sonder enige kweekhuisgasvrystellings. In hierdie proefskrif word sonkragkonsentrasie tegnologie ondersoek vir toepassing in die hoë temperatuur industriële proseshitte sektor. Nuwe generasie sonkragkonsentrasie tegnologie wat gebruikmaak van keramiekpartikels as hittegeleiers en ‘n sentrale opvangs weerkaatsingstelsel, het die vermoë om temperature hoër as 1 000 °C te bereik. In hiedie proefskrif word hierdie tegnologië ondersoek rondom die konsep van ‘n sonkragkonsentrasiestelsel wat hoë temperatuur hitte verskaf vir die voorverhitting van Mangaan voor die smeltingproses.

Om die konsep te kan evalueer is ‘n optiese, energie en ekonomiese model ontwerp vir die sonkragkonsentrasie aanleg. Met hierdie modelle word optimaliseringstudies uitgevoer om die optimale aanleg en heliostaatveld uitleg te bepaal om sodoende ‘n aanleg te onwerp wat die hitte aanvraag teen die laagste koste sal verskaf. Die aanleg maak gebruik van elektriese ondersteuningsverwarmers om ‘n konstante hitte voorsiening vir die voorverhitting van die erts te verseker. Dit gebeur in die konteks van ‘n tyd-van-gebruik tarief vir elektriesiteit. Die operasionele strategie van die aanleg word bepaal deur die gebruik van ‘n optimale termiese energie opgaarversendingsprofiel wat verseker dat ondersteunings elektriese hitte teen die laagste koste bekom word. Dit word aangetoon dat die optimale versendingsprofiel die koste van die hitte wat aan die aanleg verskaf word verminder van 43.03 $\$/\mathrm{MWh_{th}}$ tot 37.96 $\$/\mathrm{MWh_{th}}$. ‘n Nuwe unieke heliostaat tegnologie, die HelioPod™, wat bestaan uit ses heliostate wat aan ‘n gemeenskaplike basisstruktuur gemonteer is, word in hierdie werke gebruik. Hierdie tegnologie is nog nie omvattend bestudeer vir die gebruik daarvan in die veld grotes wat op hierdie werke van toepassing is nie. ‘n Optimaliseringstudie van die uitleg van die HelioPod™–velde word onderneem ten einde te bepaal hoe om die uitleg van die velde te ontwerp om die benodigde energie te voorsien met die minste aantal heliostate. Hierdie werke neem die kennis beskikbaar in die literatuur oor die uitleg van bestaande optimaliseringsvelde gebaseer op individuele heliostaatvelde, en pas dit toe op “Pod”-velde. Daar is bevind dat die hoogte van die aanleg se toring, ‘n aansienlike invloed het op die ontwerp van die veld. Vir ‘n korter toring word ‘n meer gesofistikeerde uitleg benodig om optiese verliese as gevolg van blokkering en skaduwees te verminder. Vir hierdie korter toring het die geoptimaliseerde HelioPod™ veld uitleg wat ontwikkel is die ekonomiese prestasie van die uitleg met 11.18 % verbeter in vergelyking met ‘n heuristiese uitleg.

‘n Gevallestudie vir ‘n Mangaansmeltery wat gebruik maak van sonkragkonsentrasie hitteprosesse vir die voorverhitting van erts is ontwikkel. Die gevallestudie is uitgevoer by ‘n smeltery in die Noordkaap in Suid-Afrika. Die area beskik oor wereldklas sonkragbronne asook die grootste aanlandse Mangaan ertsneerslae in die wereld. Die sonkragkonsentrasie aanleg in hierdie gevallestudie was instaat om proseshitte teen ‘n koste laer as die van diesel te voorsien, maar teen byna dubbel die koste van steenkoolverbranding.

Acknowledgements

I would like to express my gratitude toward the following people and institutions at the Department of Mechanical and Mechatronic Engineering at Stellenbosch University:

To my supervisors. Prof. Gerhard Venter, thank you for your continued support and interest in the work. I am grateful to have worked under your guidance, your experience has made this academic journey an enjoyable one. I have learnt many lessons from you which I will carry with me into my professional career. Prof. Craig McGregor, thank you for always providing stimulating contributions and really thinking about any questions I brought to you. Your enthusiasm and availability for discussions was greatly appreciated.

To all my colleagues and peers at the Solar Thermal Energy Research Group (STERG). Thank you for providing a fantastic and intellectually stimulating environment. Many of you inspired me through your great work, I will dearly miss our office discussions. I will always look back fondly to my time with STERG.

I would also like to express my gratitude to Dr Matti Lubkoll and Dr Willie Smit for providing financial support via the PreMa project for my studies. I am grateful for the opportunities this has provided me.

Table of Contents

List of Figures

List of Tables

Nomenclature

Variables

$\dot{Q}$	Thermal power
A_i	Azimuth angle
A_{sf}	Solar field aperture area
C_i	Electric tariff price
E	Energy
h_{tower}	Tower height
k_d	Discount rate
k_{ins}	Insurance rate
L	Pod side length
N	Year day number
n	Plant lifetime
n_{helios}	Number of heliostats
Q	Heat energy
q	Direct normal irradiance
R	Circle radius
t	Time
W	Row width
x	Optimisation design variable
Z	Number of rows

Greek symbols

α	Elevation angle
δ	Declination angle
η	Efficiency
ω	Hour angle
ϕ	Latitude
ρ	Penalty value
τ	Time horizon length

Subscripts

at	Attenuation

bl	Blocking
cos	Cosine
e	Electric
i	Time step
opt, a	Annual optical efficiency
s	Solar
$shad$	Shading
sp	Spillage
t	Time
z	Row number

Acronyms and abbreviations

CAPEX	Capital Expenditure
CSP	Concentrating Solar Power
CST	Concentrating Solar Thermal
DLR	German Aerospace Research Centre
DNI	Direct Normal Irradiance
FEM	Finite Element Methods
LCOH	Levelised Cost of Heat
O&M	Operating and Maintenance
SM	Solar Multiple
STERG	Solar Thermal Energy Research Group
TES	Thermal Energy Storage
TMY	Typical Meteorological Year

1 Introduction

The purpose of this thesis is to investigate the application of concentrating solar thermal (CST) technologies as a high-temperature process heat source for industry. CST technologies are being investigated for this application as they are capable of concentrating irradiation to heat mediums and materials to over 1 000 °C. Additionally this high-temperature energy can be efficiently stored for long hours, decoupling the heat generation from its use. The concept is evaluated in this thesis in the context of providing high-temperature process heat to a minerals beneficiation process: Manganese smelting.

Concentrated solar power (CSP) is the application of CST technologies for the generation of electrical energy from captured solar energy. This prominent renewable energy technology has been developed for decades and at the time of writing has a total global installed capacity of 5.5 GW (REN21, 2018). Recently the International Renewable Energy Agency announced CSP generation costs had decreased by 47 % between 2010 and 2019 (IRENA, 2020). The principal drivers for the decreasing cost of the technology is the incorporation of low-cost thermal energy storage. One of the largest CSP plants in the world, Ivanpah Solar Electric Generating System, rated at 377 MW has no thermal storage. This plant was developed in 2010. In 2019 the majority of new build plants were installed with at least four hours of rated load thermal storage, and many with more than eight hours (IRENA, 2020). Thermal energy storage has allowed CSP plants to cost-effectively increase their capacity factor. Again between 2010 and 2019 the average CSP plant capacity factor has increased from 30 % to 45 %. This showcases the speed at which the industry has, and is changing, to be more competitive.

CST relies on the same technology to produce thermal energy, and therefore benefits from the same improvements CSP has experienced the last few years. The ability of CST to reach high-temperatures, store this energy for when it is needed and use the storage to provide near constant heat supply, positions the technology to be a competitor in the high-temperature industrial process heat sector. Compared to fossil fuel combustion, the traditional high-temperature heat source, CST would provide this heat with no Green House Gas (GHG) emissions.

Minerals processing is an energy intensive industry where high-temperature process heat is required and commonly delivered by combustion of fossil fuels. Previous high level studies by Lubkoll et al. (2018), Hockaday et al. (2016) and Hockaday et al. (2018) for CST process heat applications to Manganese ore sintering showed CST to be a promising alternative to fossil fuel derived process heat. Research is now under way to investigate CST derived process heat for Manganese ore smelting, to produce Manganese ferroalloy. Manganese ferroalloy is an irreplaceable component in steel production. It acts as a deoxidization agent in the steel making process. The ferroalloy is produced through a high-temperature smelting process, typically in an electrical submerged-arc furnace (SAF). The South African SAFs used for Manganese smelting have electrical loads in multi-megawatt range, typically operate 24/7, every day of the year and require temperatures up to 1 500 °C (Steenkamp and Basson, 2013). This makes Manganese smelting an extremely energy intensive process and a large GHG emitter, due to direct (combustion of fossil fuels) and indirect (electricity) sources.

The vast majority of Manganese mined in South Africa is exported as raw ore, without

going through the smelting process to make the ferroalloy. In 2001 50 % of South Africa's Manganese ore was smelted before sale and by 2014 84 % of the ore was exported without smelting (Steenkamp et al., 2018a). This represents huge potential revenue loss, as the beneficiated mineral is significantly more valuable. According to Steenkamp et al. (2018a) reasons for not beneficiating are the rising costs of electricity and increased production capacity in Asia and Oceania.

It has been reported that pre-heating Manganese to 600 °C prior to smelting can lead to a 25-35 % reduction in energy consumption of the furnace (Tangstad et al., 2015). CST technologies have the capability to deliver this high-temperature heat, and with the addition of thermal storage could provide a near constant supply, whenever it is required. The addition of a CST plant to pre-heat Manganese ore before smelting could aid in reducing the operating costs of the smelting process, and by providing clean energy, reduce the carbon emissions of the process.

CST derived process heat in South Africa is an attractive proposition because the country enjoys some of the world's best solar resource, and many of the large minerals smelting complexes are located in regions of good solar resource. Even regions with 'average' solar resources by South African standard, are still better than many countries best regions. With the current uncertainty of electricity availability and the fact that some industries rely on expensive fossil fuels such as diesel, CST derived heat has the potential to be cost competitive.

1.1 Background

The research presented in this thesis was funded by the PreMa project, which is part of the European Union's Horizon 2020 research and innovation programme. The aim of the PreMa project is to investigate and demonstrate the ability of several technologies to reduce the energy consumption and CO_2 emissions of Manganese ferroalloy production. The means of achieving these goals are to incorporate pre-heating of Manganese ore prior to smelting. Where the pre-heating energy is to be sourced from sustainable sources. The technologies investigated for this purpose are: industrial off-gas, bio-carbon and solar thermal.

The thesis falls under the work aimed at investigating solar thermal heat as the sustainable energy source for pre-heating. Stellenbosch University's involvement in the project is through the Solar Thermal Energy Research Group (STERG). STERG's HelioPod™ , high-performance heliostat technology was identified as the reflector technology for the envisaged CST system. The German Aerospace Centre's (DLR) Institute of Solar Research's centrifugal particle receiver (CentRec©) was the receiver technology selected for the project. The CentRec© is a direct absorption ceramic particle receiver, meaning the irradiation is reflected directly onto the heat transfer medium which is ceramic particles. These technologies make up the system components for the CST plant this thesis will investigate.

In 2013 the steel industry used 5 % of the world's primary energy and emitted 7 % of the world's CO_2 (Laplace Conceil, 2013). Manganese ferroalloy is predominantly used for steel production. This enormous impact of the steel industry and energy intensive nature of smelting operations is the motivation for PreMa's work to improve the sustainability of Manganese ferroalloy production, and consequently steel production.

1.2 Motivation

Renewable energy technologies are becoming the least cost option for electricity generation in many parts of the world. In 2016 and 2017, 63 % and 70 % of new added power generation was renewable energy technologies. According to REN21 (2018) the energy transition is well under way to move from traditional electricity generation to renewable energy. However, electricity generation is just one component of global energy usage. Currently about 20 % of total world energy use is for electricity generation, the remaining 80 % is shared between heating, cooling and transportation. In order to achieve the climate goals set out by the Paris Agreement, focus must be placed on transformation of all major energy sectors. To achieve this renewable energy technologies must achieve greater market penetration in the other major energy sectors as well.

South Africa is a country that relies heavily on energy intensive industries such as mining and manufacturing, which together contributed to 20 % of the country's GDP in 2017 (Stats SA, 2018). The industrial sector represents approximately 40 % of the country's total energy use, and of that, process heat generation consumes over 66 % of the energy (South Africa Department of Energy, 2019). Due to the large amount of energy consumed by process heat generation and the current sources from which this energy is obtained, a substantial environmental improvement could be achieved by implementing alternate sources of heat, potentially CST derived process heat.

Not only are renewable energy technologies desirable due to their environmental impacts, but they also have the potential to provide a lower cost of energy, compared to traditional fossil fuels. Renewable technologies have a different economic model than fossil fuels. The energy cost is predominantly based on the capital expenditure, with low operating and maintenance cost, relatively speaking. This results in a fixed energy cost over the life of the technology. Fossil fuel or traditional electrical energy costs are a strong function of the variable cost of the fuel source. These costs can be difficult to accurately predict over a project's multi-decade lifetime and often have the potential to increase. Renewable technologies may therefore allow greater certainty for long term financial planning.

The motivation for this thesis is to explore the feasibility and benefit of renewable technologies in new applications, that could aid in creating a more sustainable future.

1.3 Research aim and objectives

The aim of this research was to investigate the potential for CST technologies to provide high-temperature process heat to a Manganese smelter pre-heater unit. This research investigates the configuration of such a CST plant and how the plant could operate to leverage the technologies benefits, to deliver the least cost heat. These results will allow the PreMa project to compare CST based pre-heating to the alternate sustainable process heat sources the project is investigating.

The thesis aims to answer the following research initiating question:

What is a suitable configuration and operating strategy for a CST plant based on the CentRec© particle technology and HelioPod™ heliostat technology, and at what cost can it deliver heat?

Based on the question above, the following objectives have been formulated:

1. Develop an optical, energy and economic model for the CST plant to predict the plant performance.
2. Determine the optimal operating strategy of the CST plant that minimizes the cost of the provided energy.
3. Investigate optimised large HelioPod™ field layouts.
4. Conduct a case study for a CST plant providing process heat to a Manganese smelter in South Africa.

1.4 Research methodology

A case study of a minerals beneficiation plant will be conducted to determine the potential of CST based pre-heating for Manganese smelting. This will also provide reference material for the energy and techno-economic analysis of the plant. Information from the case study will include parameters such as required thermal input to the beneficiation plant and meteorological conditions (solar radiation).

A plant optical and energy model will be developed; this will be used to determine performance of the plant given a certain configuration. The impact of changing the configuration can then be investigated. In order to understand the feasibility of the technology for the application the characteristics of the plant output must be understood. Furthermore, the output is required to determine the cost of the produced heat. The optical model will make use of existing sophisticated solar ray tracing tools. The energy model will be self developed in Python.

Determining the lowest cost energy possible from the CST plant requires determining how best to use the captured solar energy. To investigate this an optimisation study of thermal energy discharge from the thermal energy storage (TES) will be completed. This will make use of the optical and energy model to determine how much energy is available, and when it is available. This problem will be solved in Python, in order to couple to the optical and energy model.

The collector field of a CST plant represents a substantial contribution to the total capital expenditure of the plant and the few previous investigations of HelioPod™ fields have been for relatively small fields. For these reasons the field layout will be investigated, to determine a suitable large scale HelioPod™ field layout. The goal will be to design a field capable of delivering the required solar energy whilst utilising the smallest number of heliostats possible. New algorithms will be developed for HelioPod™ field layout design. In order to carry out this optimisation work, this thesis will make use of the Sunflower ray tracer (Richter et al., 2018) to analyse the optical performance of a set field, as this tool can be called from Python, in which the optimisation routine will be developed.

To evaluate the economic performance of a CST plant providing process heat, a case study will be conducted for a Manganese smelter. For the technology to be attractive and feasible for implementation it must exhibit favourable economic performance. The levelised cost of energy concept will be used to evaluate the economic performance of the plant. This allows the technology to be compared against other sources of heat, which might have different costs involved or even plant lifetimes. The best configuration of the plant, in terms of

its solar field size and amount of thermal energy storage will be determined through a parametric study of these parameters and the resulting levelised cost of heat.

The methodology that is to be used for this thesis is summarised in Figure 1.1 below. The models that are developed are shown as blue blocks. Optimisation tasks are shown as red blocks, and input data is shown as yellow blocks. Figure 1.1 shows how the various components interact to determine the best plant configuration for the case study. The plant configurations are evaluated based on the resulting levelised cost of heat (LCOH). Plant configuration are iterated to achieve a configuration resulting in the lowest LCOH.

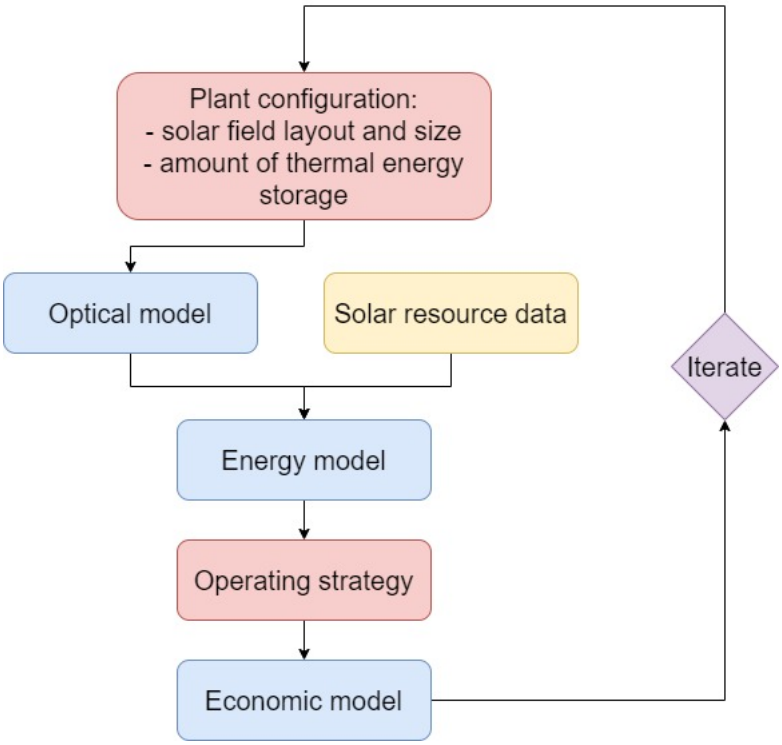

Figure 1.1: Research methodology.

2 Literature review

2.1 Manganese

Manganese is a ferrous metal that is primarily used as an alloy component in the production of steel (Steenkamp and Basson, 2013). Manganese serves as a desulfurizing and deoxidizing component in steel production. According to a report by the United States Geological Survery, Manganese is an irreplaceable alloy in steel production, with no substitutes for its use known (Cannon et al., 2017).

Cannon et al. (2017) state that Manganese is a plentiful resource, with the element being the 12th most abundant on the planet and can be found in vast quantities on land and in the seabed (however there is currently no production from seabed resources). The authors continue to state that although there is plenty of Manganese deposits around the world (resources) the amount of Manganese that can be economically extracted (reserves) are far less, and highly unequally distributed. Furthermore the ore deposits contain varying concentrations of Manganese, ore that is sold on the world market contains 38 - 55 % Manganese. For this reason many countries with Manganese resources do not extract the ore due to its low grade.

According to Cannon et al. (2017) South Africa, Ukraine and Brazil have the largest Manganese ore resources and together accounted for 65 % of all reserves in 2013. The Kalahari Manganese Field in South Africa's Northern Cape accounts for over 70 % of the worlds Manganese resources and its high grade ore is typically 40 % Manganese, this is the world's largest concentration of land-based Manganese deposit (Steenkamp and Basson (2013) and Cannon et al. (2017)). The second and third largest land based deposits are much smaller in size and offer lower grade Manganese - the Molango district in Mexico and the Bolshe Tokmak district in the Ukraine contain 9 % and 6 % of the world's resources respectively, with typical ore grades of 28 % and 18 %.

2.1.1 Manganese beneficiation

Minerals beneficiation is the process of adding economic value to the extracted mineral, typically by increasing the concentration/ grade of the desired mineral. In 2014 the export value of Manganese ore and Manganese ferroalloy was R 1 539 per kiloton and R 10 632 per kiloton, respectively (Department Mineral Resources, 2016). One form of Manganese beneficiation is smelting, this is a carbothermic reduction process that produces Manganese ferroalloys, which in turn is used in steel production (Steenkamp and Basson, 2013). The main ferroalloys used around the world are High-Carbon ferromanganese (HCFeMn) and Silicomanganese (SiMn), these alloys differ in the quantities of Manganese, Silicon and Carbon present. Both HCFeMn and SiMn are produced at smelter plants in South Africa.

2.1.2 Smelting

Manganese ore contains oxides, carbonates and other minerals that are not desirable constituents of Manganese ferroalloy. Smelting is a carbothermic reduction process in which the oxides are reduced from the Manganese ore resulting in a Manganese ferroalloy of desired Manganese concentration (Steenkamp and Basson, 2013).

Manganese ore, reductant (carbon) and fluxes are the input to the furnace and Manganese alloy, slag and off gases are the output (Tangstad et al., 2015). Slag is the minerals found in the ore that do not reduce and are not required as components to the desired ferroalloy and so are discarded. The off gases consist of oxygen and carbon that has bonded during the reduction processes. The energy required for the process is supplied in the form of electrical energy.

2.1.3 Submerged arc furnace

In South Africa Manganese ferroalloys are produced in submerged arc furnaces. These furnaces utilise electrodes that extend down into the feed (ore, reductant and flux), current moves from the electrodes to the slag and reductants and through resistive heating generates sufficient energy for the process (Steenkamp et al., 2016). In South Africa all furnaces used for Manganese ferroalloy production use AC electricity. According to Steenkamp and Basson (2013) the smelting process of HCFeMn and SiMn takes place at $1\,400 - 1\,450$ °C and $1\,500 - 1\,600$ °C respectively. Figure 2.1 illustrates the workings of a submerged arc furnace.

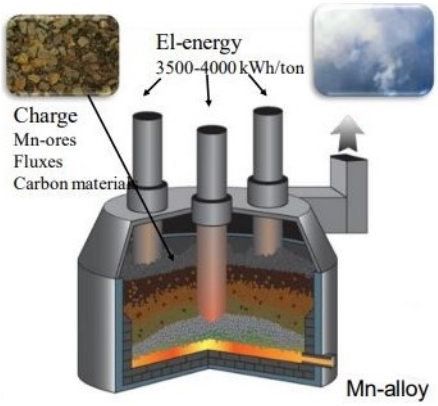

Figure 2.1: Submerged arc furnace (A.SPIRE, 2019).

The furnaces are extremely energy intensive as they operate continuously near full power. Barker (2011) describes the furnaces as base load systems due to the large electrical demand they place on the grid and their steady operation. In South Africa the installed furnaces ratings range from 4.4 - 80 MW (Steenkamp and Basson, 2013). Steenkamp et al. (2018b) reports that at the Transalloys smelter complex the furnaces are operated 24 hours a day, every day of year with very little down time for maintenance. The furnaces are capable of long term continuous operation as the electrodes are continuously replaced by more material as they are consumed (Tupkary and Tupkary, 2018).

Due to the large electrical demand submerged arc furnaces are only feasible if low cost, stable electricity is available. As an example of the electrical demand of a typical smelter, Sithole et al. (2018) reported that a single furnace at Mogale Alloys in South Africa has an operating power of 13.75 MW and utilises 3.5-4 MWh/t of metal produced. At the time of writing the smelting operations had two such furnaces producing 55 000 tons of SiMn per annum - this equates to atleast 192.5 GWh of annual electricity use. For context this is more than some utility scale photovoltaic plants in South Africa generate per annum.

2.1.4 Manganese production in South Africa

As Manganese's primary use is as an alloy for steel production the demand of Manganese closely follows the demand for steel (Steenkamp and Basson, 2013) and (Department of Mineral Resources, 2013). According to the Department of Mineral Resources (2013) the South African steel market has been in decline, resulting in local Manganese sales being in decline for both ore and alloys. Figure 2.2 shows the production, local sales and export sales of Manganese ore over a number of years. From Figure 2.2 it can be seen that the production and export of the ore has increased whilst local sales has remained steady pre- and post- 2008 economic recession. As a percentage this represents a decrease in local sales as production has increased but local sales volume has not.

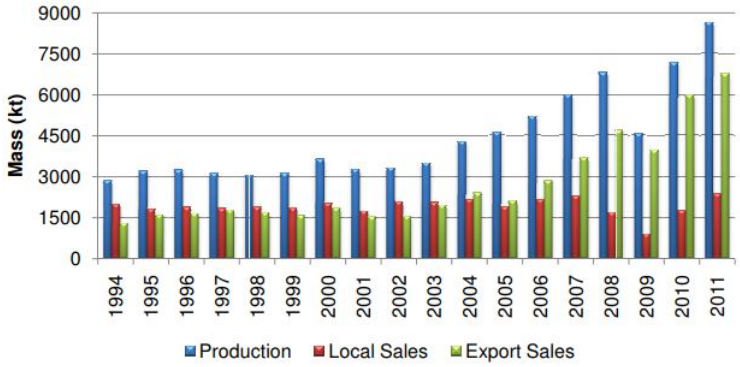

Figure 2.2: Manganese ore production and sales for South Africa (Department of Mineral Resources, 2013).

Figure 2.3 shows the production, local sales and export sales of Manganese ferroalloys, as well as the local steel production. It can be seen that the local market for ferroalloy sales has been in decline, which is in-line with the local steel production market. Furthermore production and export sales are relatively steady pre- and post- 2008 economic recession.

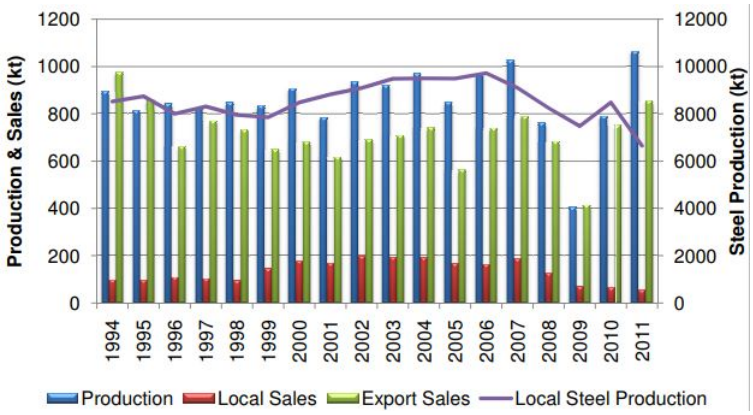

Figure 2.3: Manganese ferroalloy production and sales for South Africa (Department of Mineral Resources, 2013).

Comparing Figures 2.2 and 2.3 it can be seen that the majority of South African Manganese products are exported. Furthermore it can be seen that the amount of ore extracted

has increased but the amount of Manganese ferroalloy produced through beneficiation processes has not.

Figure 2.4 shows the Manganese ore production for the world's largest producers as well as the total world production. Figure 2.5 shows the Manganese ferroalloys production by the world's largest producers. These two figures have been compiled using data from USGS (n.d.).

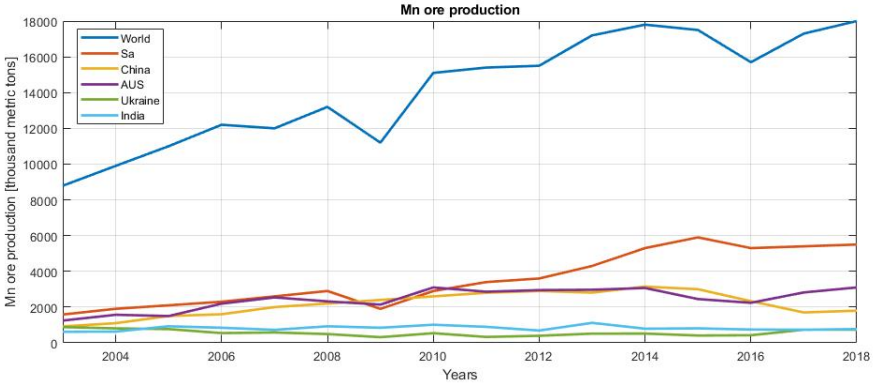

Figure 2.4: Manganese ore production by leading countries.

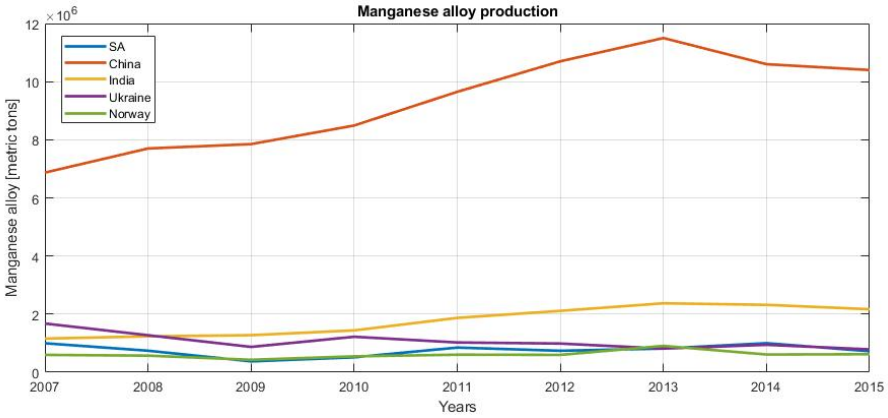

Figure 2.5: Manganese alloy production by leading countries.

Comparing Figures 2.4 and 2.5 to Figures 2.2 and 2.3 it can be seen that South Africa has followed global trends in increasing its ore production. However its Manganese ferroalloy production has remained fairly unchanged in production capacity. At the same time the lead producers; China and India, have increased production. South Africa could stand to gain a significant economic benefit by benficiating more of its Manganese ore before export. According to Cannon et al. (2017) the vast majority of Manganese ore is used around the world is beneficiated before use, which makes perfect sense as more than 90 % of Manganese is used for steel production, where it is required as Manganese ferroalloy. Therefore it is likely that the ore exported from South Africa is beneficiated elsewhere.

2.1.5 Manganese ferroalloy production plants in South Africa

In South Africa there are four Manganese ferroalloy smelter complexes in operation. Mogale Alloys located in Krugerdorp, Gauteng, can produce SiMn in two 20 MVA submerged arc furnaces for a total annual production of 55 kilotons. Their ore is sourced from mines in the Hotazel area of the Northern Cape (Sithole et al., 2018).

Transalloys is located near eMalahleni, Mpumalanga. Their smelter complex produces SiMn and consists of five submerged arc furnaces; one 15 MVA, two 22 MVA and two 48 MVA furnaces. Production is rated at 180 kilotons per annum. The Manganese ore is delivered by rail and sourced from a number of mines in the Northern Cape, as well as from mines in the Postmasburg area (Steenkamp et al., 2018b).

Metalloys are the largest Manganese ferroalloy producers in South Africa. Their smelter complex is located in Meyerton, Gauteng. They have four submerged arc furnaces installed; two 75 MVA and two 81 MVA furnaces, for a total installed annual capacity of 480 kilotons per annum of HCFeMn (Steenkamp and Basson, 2013).

Assmang have two smelter complexes, one in Cato Ridge, Kwazulu-Natal and a second in Machadodorp, Mpumalanga. There are five furnaces at Cato Ridge; two 12 MVA, one 22 MVA and two 24 MVA furnaces, capable of producing 200-240 kiloton of HCFeMn per annum. There are four furnaces at Machadodorp, but not all are used for Manganese ferroalloy production. The two furnaces used are rated at 24 MVA and 30 MVA and produce 130 kiloton of HCFeMn per annum (Steenkamp and Basson, 2013).

2.1.6 Challenges facing the South African Manganese ferroalloy industry

van Zyl et al. (2016) researched barriers faced by the South African Manganese industry. Their research separately identified barriers for the Manganese ore and alloy sectors. The main challenges faced by the Manganese ferroalloy industry were identified to be poor market conditions, rising electrical tariffs, electricity availability and productivity and stability of the workforce.

Due to the long operating hours and high electrical demands these smelters are some of the largest electricity users in South Africa. In 2010 Assmang and Mogale Alloys were classified within the top 100 largest customers of Eskom (Hogan, 2010). Consequently, the smelters are classified as key industrial customers (KIC) by Eskom, these are the utility's largest customers, requiring more than 100 GWh a year (Eskom, 2019).

Due to their dependence on steady, low cost electricity and constant electrical supply the smelters face challenges posed by the current state of generation capacity, electricity availability and rising tariffs (Barker, 2011) and (van Zyl et al., 2016). Electricity availability is especially concerning at peak demand hours.

van Zyl et al. (2016) found in their research at least two of South Africa's Manganese ferroalloy smelters have decreased production due to the challenges facing the industry. Sithole et al. (2018) reported that in 2016 Mogale Alloys converted one of their two furnaces to the production of ferrochrome alloy from Manganese ferroalloy. As of 2017 only 40 % of the installed capacity for Manganese ferroalloy production is in use nationwide (Steenkamp et al., 2018a). This does not bode well for South Africa's Manganese beneficiation industry.

As a KIC the smelters are subject to Eskom's Megaflex tariff, which is subject to several cross-subsidies; affordability subsidy, electrification and rural subsidy and urban low voltage subsidy (Mahony and Baartmanm, 2018). These subsidies represent an extra cost component applied to the tariff, which are used to support economic development elsewhere. The subsidies have also increased as a percentage of the cost of electricity. This further compounds the challenges faced by the energy-intensive industries.

According to Mahony and Baartmanm (2018) Eskom's sale of electricity to key industrial customers has steadily been decreasing since 2011 which has the potential to increase the cost per unit of electricity as the demand will decrease but the installed capacity does not. The authors report that the KICs are struggling to remain globally competitive.

2.2 Concentrating solar thermal energy

Concentrating solar thermal technologies use reflectors to redirect the direct beam component of solar radiation, onto a receiver. The diffuse radiation scattered off clouds and other particles is not reflected. In the receiver a heat transfer medium absorbs the solar radiation, after which this captured solar energy can be used either for electricity generation or as a heat source. With the addition of thermal energy storage CST plants can provide dispatchable energy.

2.2.1 Concentrating technologies

A number of different technologies for reflecting the solar radiation exist; parabolic troughs, central receiver systems, linear Fresnel and parabolic dishes. All technologies track the sun in order to reflect the direct beam component of the solar radiation onto a receiver. The technologies differ in their degrees of motion of tracking, maximum theoretical concentration achievable and consequently, maximum temperatures the heat transfer medium can reach.

The technologies can be split into two categories; single axis trackers that line focus and two-axis trackers that point focus. Parabolic troughs and linear Fresnel are line focus concentrators, they track the sun along a single axis, east to west, and reflect the solar radiation onto a receiver that runs the length of the concentrator. Central receiver systems and parabolic dishes are point focus concentrators, they track the sun in two axes, azimuth (east to west) and elevation (vertically above the horizon), and reflect the solar radiation onto a single point. Lovegrove and Stein (2012) provided a thorough derivation detailing the thermodynamic limits on concentration for each type of focus system. The theoretical limits for the maximum theoretical ratio between the reflector surface and receiver surface are 46 250 for point focus systems and 215 for line focus systems. The higher this value the greater the temperatures that are achievable. Figure 2.6 shows the working principals of the two most common concentrating technologies, parabolic trough and central receivers. Islam et al. (2018) reported that by 2018 there was 77 and 13 parabolic trough and central receiver plants operational around the world, respectively. For future plants the authors reported 20 parabolic trough plants and 16 central receiver plants under construction and development. This showcases the uptake in central receiver technology.

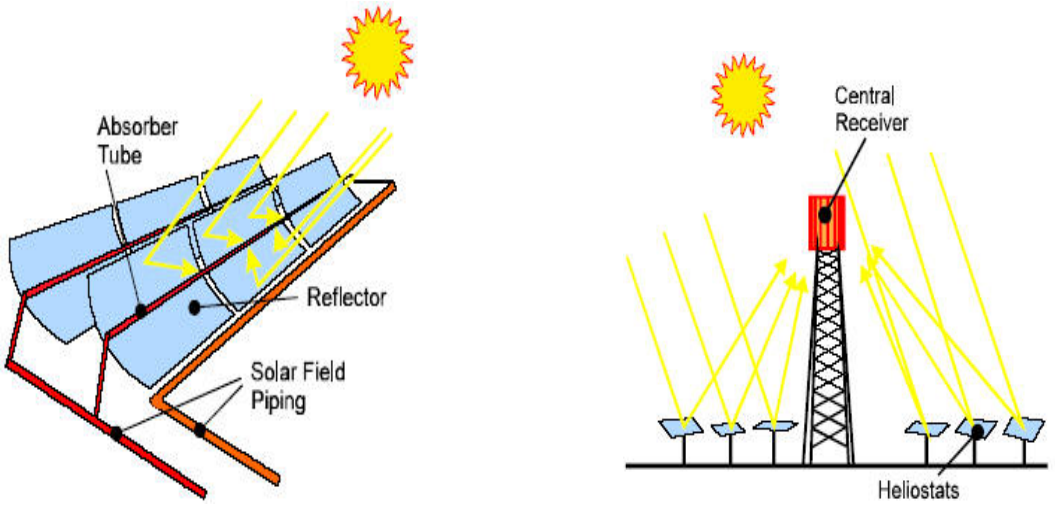

(a) Parabolic trough systems - line focus.

(b) Central receiver systems - point focus.

Figure 2.6: Working principles of primarily used concentrating technologies (How CSP Works, n.d.).

2.2.2 Solar energy

The sun is a giant gaseous sphere undergoing fusion reactions resulting in realised energy which radiates away from the surface. Given the black body temperature of the sun's surface (5 777 K), the distance between the sun and earth and simple black body radiation assumptions the solar constant (I_{sc}) can be calculated to be equal to 1 367 W/m^2 (Duffie and Beckman, 1991). This is the irradiance (incident radiation) that reaches Earth's atmosphere from the sun.

The irradiance reaching Earth's surface is the solar constant discounted by the amount of air the radiation travels through and particulates and molecules in the atmosphere that absorb and scatter the radiation (Lovegrove and Stein, 2012).

Irradiation consists of two components, direct normal (DNI) and diffuse irradiance. DNI would be the irradiance measured on a flat surface normal to the sun. Diffuse irradiation is radiation from scattered rays. Only DNI can be reflected and therefore this is the solar resource relevant to concentrating solar technologies. DNI is blocked by cloud cover, for this reason CST plants are best suited to low annual rainfall locations.

The most accessible solar resource data is satellite derived. This data is available as typical meteorological years (TMY). Each data point in a TMY's dataset's measurement should be within a 5 % tolerance of the long term climatological average (Lovegrove and Stein, 2012). Typical TMY files used for solar modelling have an hourly measurement resolution, with representative measurements taken over 10 years. This approach accounts for inter-year variations in solar energy as well as the seasonal variance. Figure 2.7 shows a DNI map of the world. South Africa can be seen to have some of the world's best solar resource.

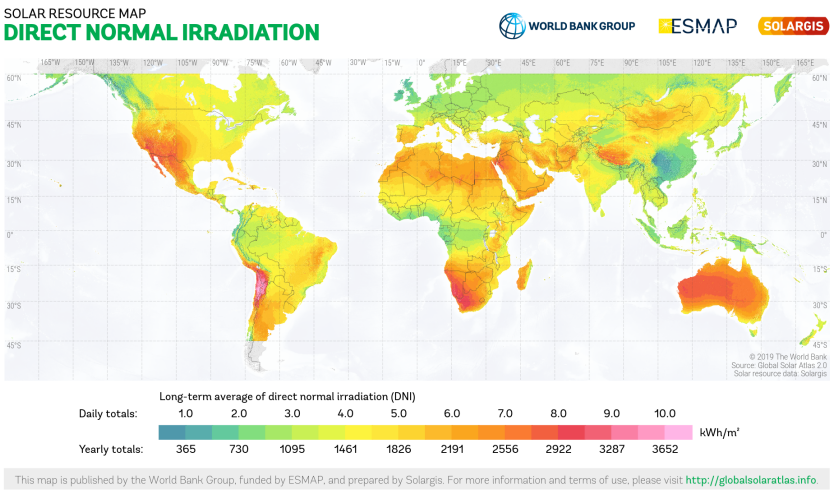

Figure 2.7: Solar resource map of the world, depicting annual average DNI (SolarGIS, 2019).

2.2.3 Central receiver designs

Since this thesis deals with central receiver technology, an overview of the technology's development, current state-of-the-art and future technologies are presented. Parabolic troughs are the most widespread used concentrator technology, but due to the higher temperatures achievable by central receiver systems this technology is gaining increasing market penetration. At the time of writing, Ho (2017) claimed 60 % of under-construction and planned CSP plants were central receivers. Ho and Iverson (2014), Ho (2016), Ho (2017) and Jiang et al. (2019) provide comprehensive overviews of the development of many different central receiver technologies.

Different central receiver technologies are developed for different heat transfer media. Water, steam, various molten-salts, solid particles, gases and liquid metals have been investigated. Steam and molten-salt plants are currently being operated at utility scale power generation. All other mentioned heat transfer media are limited to research or pilot plant scale operation. Each heat transfer media requires specific receiver designs. Table 2.1 provides an overview of the temperatures achievable by the various technologies.

Table 2.1: Receiver heat transfer media outlet temperatures, adapted from Ho (2017).

Heat transfer media	Outlet temperature °C	Stage of development
Steam	$390 - 560$	multiple operating utility-scale operations
Molten-salt	~ 600	multiple operating utility-scale operations
Liquid sodium	~ 800	past research facilities, present small commercial plant operational
Ceramic particles	$> 1\,000$	research facilities
Air	$700 - 1\,000$	research facilities

Figure 2.8 show various different receiver technologies. Figure 2.8a illustrates a panel of tubes through which a heat transfer fluid flows, where the outer surfaces are subjected to the reflected irradiance. Figure 2.8b shows a falling curtain of ceramic particles. This receiver is classified as a direct absorption receiver as the heat transfer media is directly heated by the irradiance. Figure 2.8c shows an external receiver. This receiver uses panels of tubes with the heat transfer media passing through. The benefit of this design is it does not limit line of sight to the heliostat field. Figure 2.8d shows a cavity receiver, the tube panels are placed inside a cavity to minimize convection and radiative heat losses. The cavity does limit line of sight of heliostats, this is overcome by employing taller towers.

The first central receiver plants that were built generated superheated steam in the receivers. However steam is difficult to store in large energy quantities due to its energy density. Recent trends are for plants to incorporate thermal energy storage due to its significant economic benefit by increasing the plant's capacity factor. As a consequence newer tower plants utilize molten salt as the heat transfer medium due to its lower storage cost. Molten salt, typically a mixture of potassium and sodium nitrate, has operating temperatures between 200 to 600 °C. Below this range the salt solidifies and becomes corrosive and above this range the salt becomes chemically unstable (Ho and Iverson, 2014).

2.2.4 Thermal energy storage

Concentrating solar power, like many renewable energy technologies, has variable power generation. This is simply because power generation is coupled to the energy resource availability. Incorporating thermal energy storage (TES) allows concentrating solar plants to store their thermal energy to shift power generation to match demand (often resulting in higher energy purchase prices (Kuravi et al., 2013)) or to supply energy when no irradiation is available (Nithyanandam and Pitchumani, 2014). Compared to electrical or mechanical storage, TES has lower capital costs and higher round trip efficiencies (Kuravi et al., 2013). The TES efficiency refers to the amount of energy placed in storage, compared to the amount that can be extracted.

A number of thermal energy solutions are available in literature; sensible, latent or thermochemical storage, but only sensible is currently installed at plants (Liu et al., 2016). Current state of the art TES for utility scale CSP plants is a two-tank molten salt sensible storage (Nithyanandam and Pitchumani, 2014; Liu et al., 2016). In this configuration hot molten salt from the receiver is pumped into a storage tank. When the stored energy is required a heat exchanger is used to heat the power block working fluid, after which the molten salt enters the cold storage tank. When irradiation is available molten salt is pumped from the cold storage tank to the receiver to be heated.

Sioshansi and Denholm (2010) and Madaeni et al. (2012a) completed techno-economic studies of CSP plants incorporating TES which showed that the addition increases the value of CSP plants as power generation can be decoupled from the resource availability and more energy captured by the solar field can be used (by avoiding curtailment during times where the solar field thermal power is greater than the rated load). The authors discuss a number of ways that the operating strategy can be used to increase value. Power generation can be focussed to high value periods, yielding more revenue for the same

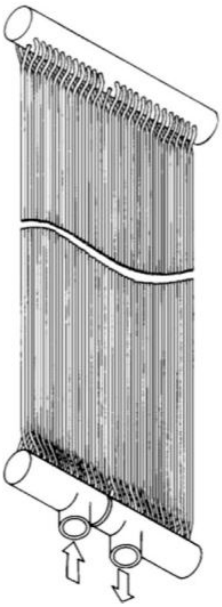

(a) Panel of tubes for fluid based receiver (Ho and Iverson, 2014).

(b) Falling particle curtain (Ho, 2017).

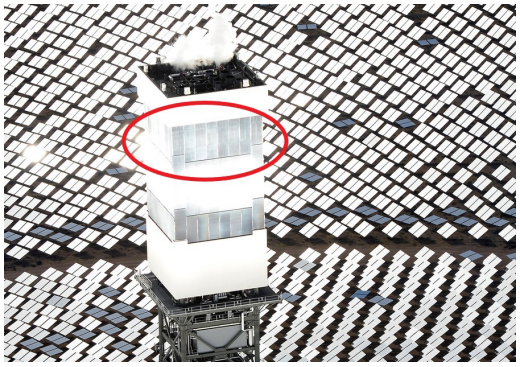

(c) Tubular steam receiver (Taylor, 2014).

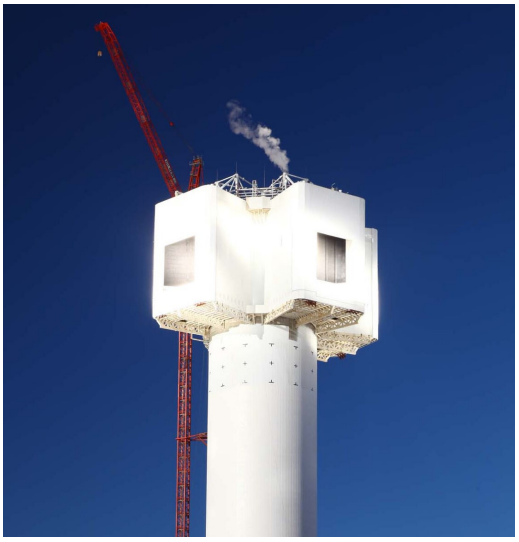

(d) Cavity receiver (Abengoa, 2020).

Figure 2.8: Various receiver technologies.

amount of energy sold. Another interesting point made is that many renewable plants are situated away from the users, requiring new transmission lines. TES can change the plant generation to output a lower rate over a longer time period, rather than a higher rate over a short time period. This reduces the size and cost of transmission lines.

In 2010 the construction of the largest CSP plant (at that time) started, Ivanpah Solar Electric Generating Systems, with a rated power output of 377 MW(National Renewable Energy Laboratory, 2020b). This plant contains no TES. Liu et al. (2016) reported that in 2016 80 % of concentrating solar plants under construction incorporated TES. In 2020

multinational CSP developer Abengoa started retrofitting TES to older plants that were originally constructed without these systems (Chamberlain, 2020).

2.2.5 Particle receiver technology

In 2017 the National Renewable Energy Laboratory and Sandia National Laboratory released a roadmap for next generation concentrating solar technologies (Mehos et al., 2017). The roadmap discusses the development of three new central receiver technologies, based on new heat transfer mediums. The goal of these new technologies is to increase the efficiency of concentrating solar plants by combing super-critical carbon dioxide Brayton cycles with the higher temperature (> 720 °C) heat transfer mediums from the receiver. The roadmap is an extensive document which details the areas of these technologies that require development. One of the technologies identified to reach these temperatures are particle receivers. The roadmap's conclusion on particle technology is that many technologies required are already commercially available, such as; particle elevators, particle to fluid heat exchangers, particle storage bins and particle feeders. Furthermore the roadmap compared a 10 MW_e central receiver plant using molten-salt and particle technologies, and concluded the particle based system would be 30 % cheaper to build.

A comprehensive overview of particle receiver technologies can be found in the work of Ho (2016) and Jiang et al. (2019). Particle receivers are classified as either direct or indirect absorption - describing whether the irradiation directly hits the particle or piping transporting the particles. The benefits of particle receivers are high potential temperatures ($> 1\,000$ °C), inexpensive storage if particles are directly stored in insulated containers and a higher maximum flux limit on the receiver (Mehos et al., 2017).

2.3 PreMa CST equipment

This section provides a description of the concentrating solar technologies from the PreMa project, which form the system components for the work of this thesis.

2.3.1 HelioPod™ technology

STERG's Heliopod™ heliostat technology is the reflector technology for the PreMa project. A single Heliopod™ consists of 6 individual heliostats on a common equilateral triangle base structure. Currently 4.6 m and 6 m pod side length varieties exist. The individual heliostats contain only a single, small 2.23 m^2 facet (mirror). The benefits of the technology are summarised by Larmuth et al. (2016) and Kotzé et al. (2016): no ground preparation or supporting foundations are required, easy assembly possible by unskilled labour and a modular design allowing application in large or small fields (aided by wireless control and communication).

Figure 2.9 shows the HelioPod™ technology. Figure 2.9a shows a single HelioPod™, where the six heliostats on the accompanying base structure can be seen. Figure 2.9b shows the test site, Helio100, where the technology has been demonstrated since 2015 with a total of 120 heliostats or 20 pods.

(a) A single HelioPod™.

(b) Helio100 HelioPod™ field.

Figure 2.9: HelioPod™ technology.

2.3.2 Particle receiver

The German Aerospace Research Centre's (DLR) Institute of Solar Research has developed the centrifugal particle receiver or CentRec©. The receiver consists of a rotating cylinder, angled downward from the horizontal, with an aperture (an opening), to allow reflected irradiation in (Wu et al., 2015a). Particles enter the cylinder from above and due to; the downward tilt and centrifugal forces generated by the spin, form a dense, downward moving film, on the inside cylinder wall. The particles move downward, absorb the irradiation and then fall into a collector ring where they are moved to a storage bin. Figure 2.10a shows the workings of the receiver. The CentRec's© rate of rotation can be set to control the residence time of the particles to the irradiation, allowing the receiver to maintain steady particle outlet temperatures under a variety of incoming fluxes.

The CentRec© receiver has been under development for a number of years. In 2013 a 10 kW_{th} proof of concept lab-scale prototype was manufactured and tested. The prototype tests confirmed the particle mass flow rate could be controlled to achieve constant outlet temperature under varying incoming solar fluxes and outlet temperatures of 900 °C were possible (Wu et al., 2013).

Successful proof of concept and numerical model validation lead to the manufacturing and testing of a full scale, commercially sized 2.5 MW_{th} unit (Ebert et al., 2016). The full scale prototype accumulated 70 hours of on-sun operation during 2017 and 2018, and achieved periods of maximum average particle temperatures of 965 °C. Ebert et al. (2018) stated the tests yielded no significant problems with the concept. Figure 2.10b shows the receiver in a tower at a test facility. It is noted from this figure that there is a significant amount of spillage as a result of the heliostat field that is not designed for small high flux density receivers (Ebert et al., 2018).

2.4 CST process heat applications

High temperature process heat (> 400 °C) accounts for 10 % of the total world energy use (Farjana et al., 2018). There is little information regarding high temperature process heat demand in South Africa. According to Lauterbach et al. (2012) 65 % of Germany's process heat requirements are above 500 °C, with the following industries involved; chemicals, basic metals and non-metallic minerals industries. These industries are also found in

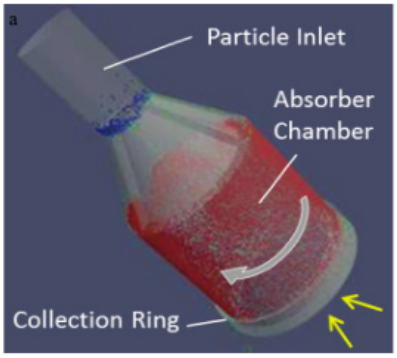

(a) CentRec© receiver operation principles.

(b) CentRec© receiver in tower configuration.

Figure 2.10: CentRec© receiver (Ebert et al., 2018).

South Africa so it is likely there is a demand for high temperature process heat.

Uhlig et al. (2015) performed a study of industrial applications where high temperature concentrating solar thermal heat could be useful. The authors identified the oil and the minerals industries. In the oil industry CST process heat could replace natural gas or other intermediate oil products combustion as a heat source, this frees up more fuel for sale and reduces plant emissions. In the minerals industry pre-heating of minerals with extremely high melting temperatures (1 350 °C – 1 675 °C) before being placed in electric arc furnaces would reduce furnace energy use. CST process heat is well suited to these industrial application due to the high temperatures it can produce.

Eglinton et al. (2013) investigated the potential for concentrated solar thermal technologies for application in the Australian minerals and mining industry. The authors identified solar thermal decomposition of alumina, calcination of limestone and magnesia as potential applications. The potential of the technology is enhanced due to proposed carbon taxes and the isolated locations of the mineral industries, which drives up the price of competing fossil fuels as a heat source.

The DLR has produced a number of papers outlining potential applications for their particle receiver technology. Amsbeck et al. (2015) discuss the application of CST process heat for the pre-heating of scrap metal to 600 °C prior to melting in induction furnaces, resulting in a reduction of up to a third of the electrical energy demand for the furnace. Amsbeck et al. (2017) discuss the application of CST process heat to phosphate sludge drying. According to the authors the sludge is currently heated to temperatures up to 750 °C, and this heat is delivered through natural gas or light heating oil combustion. Amsbeck et al. (2014b) discusses the application of CST process heat for a plasterboard manufacturing plant. Plasterboard manufacturing requires temperatures up to 700 °C, and this heat is typically supplied from gas or oil burners. The authors completed a cost-optimised design for a CST plant based on the CentRec© receiver. It was shown that for a variety of potential solar resource locations that the CST system could deliver lower cost heat than oil burners, even when assuming prototype costs of the receiver and heliostats.

A couple of interesting pilot scale test projects have been developed to showcase CST

process heat capabilities. The SolarGas project in Australia utilises a small heliostat field to deliver heat at 850 °C to a reactor. In the reactor methane and water are turned into carbon monoxide and hydrogen (Eglinton et al., 2013). CSP developer BrightSource energy developed a central receiver system for Chevron in Coalinga, California. Here the CST plant delivered high-temperature and high-pressure steam for enhanced oil recovery (Glance, 2011). The CST system was rated at 29 MW_{th}. Figure 2.11 shows these demonstration plants.

(a) CST for hydrogen production (Eglinton et al., 2013).

(b) Enhanced oil recovery using CST derived steam (Glance, 2011).

Figure 2.11: CST process heat pilot projects.

2.5 Heliostat field optical theory

This section provides the necessary theory for understanding the optical analysis of solar ray-tracing for optical characterization.

Heliostat field layouts are evaluated by a metric called the field optical efficiency. This metric is the quotient of the solar irradiation incident on the field and the reflected energy reaching the receiver. A number of different losses occur in the optical system. These losses are: cosine, spillage, blocking, shading and attenuation. Stine and Geyer (2001) provide a good overview of the various loss mechanisms.

The total field optical efficiency is defined as follow:

$$\eta_{opt} = \frac{\dot{Q}_{rec}}{\dot{q}_{dni} A_{sf}} \tag{1}$$

$$\eta_{opt} = \eta_{cos} \cdot \eta_{sp} \cdot \eta_{shad} \cdot \eta_{bl} \cdot \eta_{at} \cdot \eta_{int} \tag{2}$$

where $\dot{Q}_{rec}$ is the reflected irradiation reaching the receiver, $\dot{q}_{dni}$ is the solar energy, A_{sf} is the total solar field reflector area, η_{cos} is the cosine efficiency, η_{sp} is the spillage efficiency, η_{shad} is the shading efficiency, η_{bl} is the blocking efficiency, η_{at} is the attenuation efficiency and η_{int} is the intercept efficiency. The values can be instantaneous or time averaged.

The optical efficiency is calculated using solar ray tracing software. Equation 1 is then used in conjunction with the known solar field size and weather data to calculate the energy incident on the receiver.

The next few paragraphs describe each optical loss in more detail. Unless otherwise stated all information is from Stine and Geyer (2001).

2.5.1 Cosine losses

Cosine losses are the losses associated with varying reflection area of the heliostats as it tracks the sun. Figure 2.12a illustrate the loss well. Figure 2.12b provides an annualized map showing the performance of different locations around the tower in terms of cosine efficiency.

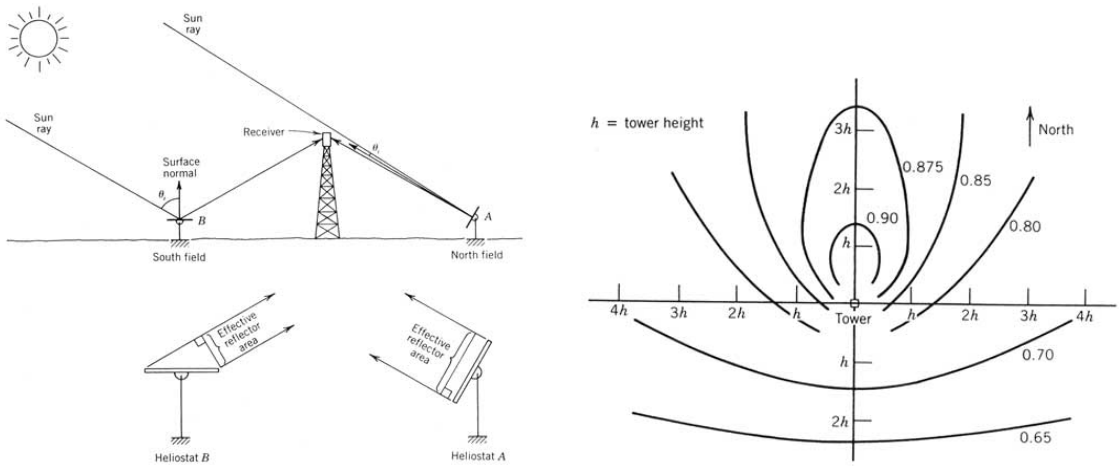

(a) Effective reflective area for heliostats.

(b) Annual average heliostat cosine losses.

Figure 2.12: Cosine losses (Stine and Geyer, 2001).

2.5.2 Spillage

Some reflected irradiation does not hit the receiver, these are called spillage losses. Spillage occurs due to beam spread, tracking inaccuracies and surface errors. Beam spread is a consequence of the sun being a finite disk in the sky. Rays hitting a heliostat are non-parallel and therefore the reflected image is a cone, Figure 2.13 illustrates this phenomena. The further a heliostat is from the receiver the larger the image spread, and therefore the worse the spillage loss.

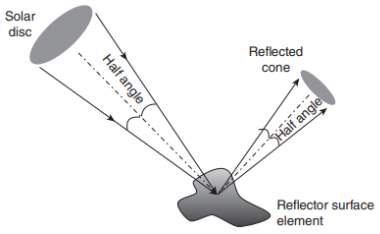

Figure 2.13: Reflected image from a heliostat surface (Lovegrove and Stein, 2012).

2.5.3 Shading and blocking

Shading losses occur when heliostats prevents solar irradiation from reaching another heliostat. Blocking occurs when a heliostat prevents reflected irradiation from another heliostat of reaching the receiver. Figure 2.14 illustrates these losses.

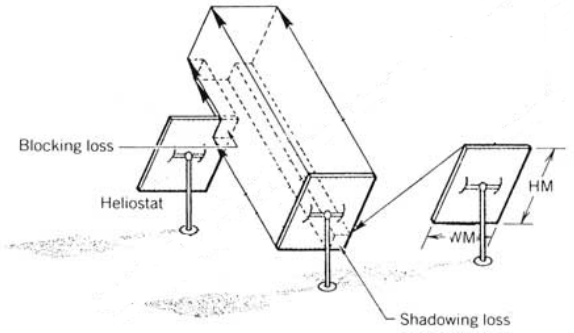

Figure 2.14: Shading and blocking within a heliostat field (Stine and Geyer, 2001).

2.5.4 Attenuation

Attenuation losses account for the decrease in reflected energy throughout the air. The further the irradiance is reflected the greater the attenuation loss.

2.5.5 Surface and tracking errors

Some loss in performance is caused by imperfection in the shape of the reflector surface, and in the tracking system, these are termed surface slope errors (SSE) and tracking errors (Lovegrove and Stein, 2012). SSE is the standard deviation of the surface normals compared to the ideal normals. Tracking errors are the standard deviation of the difference between the ideal tracking position and actual position over time.

2.6 Solar optical modelling tools

This section provides an overview of tools available for the optical performance characterization and design of heliostat fields. This work is used to determine what software is available for use in this thesis. Concentrating collectors are modelled using ray tracing techniques. Duffie and Beckman (1991) provide a concise overview of ray tracing. The authors described ray tracing as the process of following the vector paths of rays from their source through their reflections, onto the receiver. Ray tracing allows the intensity distribution of energy to be determined on the intersected surfaces.

Cruz et al. (2017) provides a detailed overview of 18 tools. These tools range from in-house developed codes by research entities, to freeware and commercially available software. The first codes date back to the original heliostat field design studies completed in the seventies. Jafrancesco et al. (2018) completed a detailed comparison of the functionality

of 4 tools. Additionally, the authors compared the simulation results of these tools on a test scenario, simulating the Small Solar Power System - Central Receiver System based at Plataforma Solar de Almeria in Spain. The resulting receiver flux profile and total incident power is compared across the various tools. Of the four tools tested, one is the author's own developed code. Bode and Gauché (2012) provide an overview of ten tools, and a comparison of the functionality of each tool.

Available tools can be split into one of two categories, detailed heliostat field optical performance analysis and heliostat field layout design and optimisation. Cruz et al. (2017) explains that the difference is in the optical model applied. For optimisation of field layout, computationally faster analytic methods are used to characterize a field's optical performance. For detailed optical analysis of an existing field, more accurate but computationally intensive, ray tracing methods are implemented.

As commented on by Bode and Gauché (2012), many of the tools discussed in the above mentioned studies are not widely available to researchers. These codes are either in-house developed codes, whose results and validations can be found in literature, or are commercially available, or have depreciated. A subset of the tools reviewed are compared in Table 2.2. The categories for comparison are the purpose of the tool, detailed optical analysis or field layout design, and the type of optical model implemented.

A tool that is fairly new is SolarPilot. Unlike any of the tools discussed in the studies above, SolarPilot has both ray tracing and analytic methods available (Wagner and Wendelin, 2018). This allows the tool to perform efficient heliostat field layout optimisation as well as detailed optical performance characterization. SolarPilot is able to provide more functionality as it incorporates and builds upon the work done in DELSOL and SolTrace, a field layout design and solar ray tracing tool, respectively. Additionally SolarPilot provides an easy to use parametric study functionality of plant design parameters.

Table 2.2: Comparison of central receiver modelling software tools.

Tool	Layout optimisation	Optical characterization	Raytracing	Analytical optical model	Availability
Delsol	Yes	No	No	Yes	Freeware
HFLCAL	Yes	No	No	Yes	Commercially avail.
Tonatiuh	No	Yes	Yes	No	Freeware, open-source
SolTrace	No	Yes	Yes	No	Freeware
SolarPilot	Yes	Yes	Yes	Yes	Freeware
Stral	No	Yes	Yes	No	Commercially avail.

Both Cruz et al. (2017) and Jafrancesco et al. (2018) advise the use of either Tonatiuh or SolTrace for detailed optical analysis. The authors note that there is no clear preferred tool for heliostat field layout design / optimisation that is readily available. Cruz et al. (2017) notes HFLCAL is a good option if acquiring a commercial tool is viable, otherwise replicating the optimisation work of well documented published work (but unavailable as a tool) via a self coded implementation is a good alternative. To this end Collado and Guallar (2012) and Noone et al. (2012) are good sources.

2.7 Heliostat field layout

This section covers literature on heliostat field layout design and optimisation. Different optimisation approaches are covered. Given the lack of literature on pod field layout optimisation, the purpose of this work is to determine applicable approaches which can be applied toward HelioPod™ field layout optimisation.

There exists a large body of research relating to heliostat field layout design and optimisation. The existing work focusses almost exclusively on fields where heliostats are not constrained together in a pod, like the HelioPod™. In this section the state of the art field layout design methodology will be discussed, as well as the limited work on field layout design of pod heliostats.

Lutchman et al. (2014) reviewed three methods available for heliostat field layout design. The methods are: patterns, field growth and free variable. The field growth method is summarised in Figure 2.15. The pattern method defines the layout by a set of parameters. The layout is then optimised by only optimizing these parameters, whilst the free variable method allows the co-ordinates of individual heliostats to be investigated as the design variables of an optimisation problem.

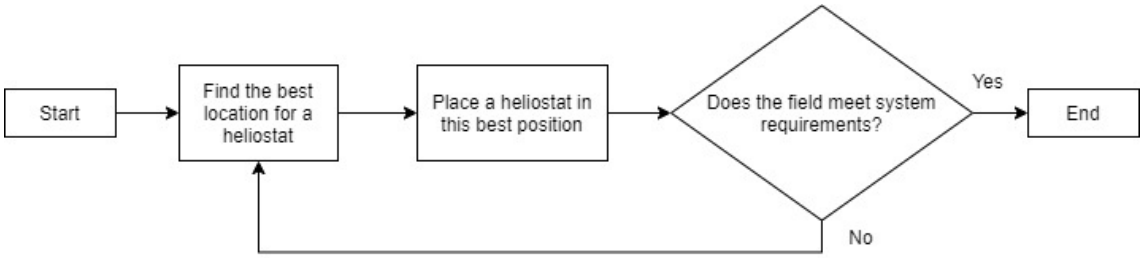

Figure 2.15: Field growth algorithm (Lutchman et al., 2014).

2.7.1 Pattern method

Pattern layouts reduce the number of design variables from many thousands for large heliostat fields to only those which define the pattern, this is usually orders of magnitude fewer (Collado and Guallar, 2012). This is the most widely used approach to heliostat field layout design optimisation (Lutchman et al., 2014).

The radial staggered layout was proposed by Lipps and Vant-Hull (1978). The radial stagger layout consists of placing heliostats on a radial grid, where the heliostats are staggered on consecutive radial rows (Stine and Geyer, 2001). The pattern is shown in Figure 2.16a. The purpose of the pattern is to reduce blocking and shading between distal and proximal heliostats, as shown in Figure 2.16b. The radial spacing is a function of the row's radial distance from the tower and the tower height. This is the most common heliostat field layout found in literature.

The Campo code developed by Collado and Guallar (2012) is a popular heliostat field layout code. The authors developed their own analytic optical model for fast optical performance characterization to be used for field layout design optimisation. The idea behind the Campo code is to start with a dense field layout, with least cosine, spillage and attenuation losses, but worst shading and blocking. Then expand the field to improve the

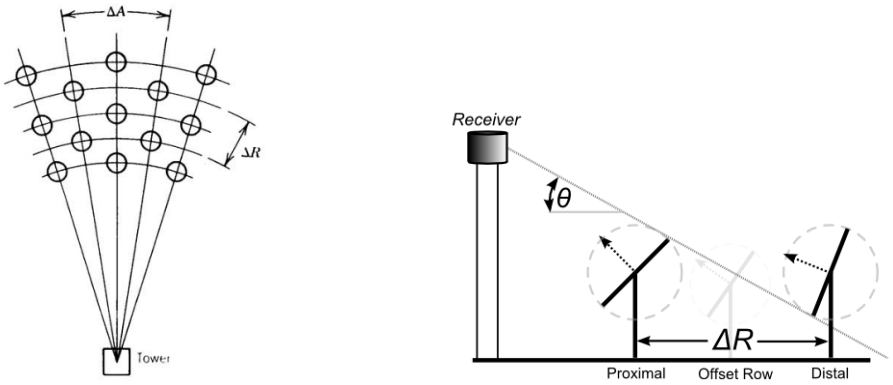

(a) Radial stagger pattern (Stine and Geyer, 2001).

(b) Radial spacing to eliminate blocking (National Renewable Energy Laboratory, 2015).

Figure 2.16: Radial stagger pattern.

shading and blocking losses, in a trade off between improving shading and blocking and worsening other efficiencies.

The densest radial stagger fields have constant ΔR (the distance between rows, as seen in Figure 2.16b) throughout the field. The parameter is determined to prevent heliostats colliding and an additional predetermined separation distance between rows to allow for maintenance. The densest layout is expanded by increasing the radial distance between consecutive rows.

Collado and Guallar (2013) redesigned the field layout of Gemasolar to investigate the improvement resulting from the Campo code. Gemasolar was the first high-temperature molten salt receiver tower plant (National Renewable Energy Laboratory, 2020a). The optimisation routine can be seen in Figure 2.17. Figure 2.17a shows the initial dense field. Figure 2.17b shows the optimal field, with each of the three zones with different radial lengths, ΔR. The radial spread increases from the nearest to furthest zones. Figure 2.17c summarises the optimisation routine's search results. It can be seen that for the optimal field each zone has its own radial spacing, which increases from the tower. To summarize the optimal field design is to keep the field dense near the tower and expand moving from the tower.

Noone et al. (2012) introduced a Phyllotaxis Spiral pattern to be used for heliostat field layout design. This is a biomimetic heuristic based on the spirals of a sunflower's seeds. The authors compared the Phyllotaxis Spiral to the radial stagger layout from DELSOL, as well as their own parameter optimised radial stagger layout. The comparison was done by redesigning the field layout of PS10, the first electrical-grid connected central receiver plant (National Renewable Energy Laboratory, 2020c). Additionally the authors developed their own optical model, specifically designed for optimisation work.

Figure 2.18 shows the original PS10 field and its redesign by optimizing the radial and azimuthal spacing parameters (Figure 2.18b) and by implementing a parameter optimised Phyllotaxis spiral (Figure 2.18c). The spiral layout improves the field optical efficiency by 0.36 % and reduces the land area by 15.8 %.

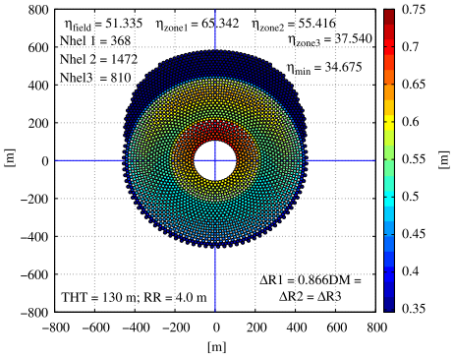

(a) Initial dense radial stagger field.

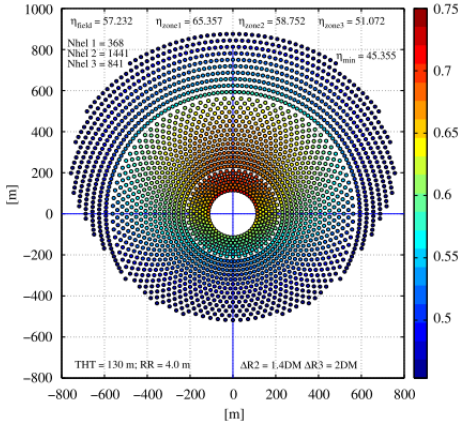

(b) Optimised expanded radial stagger field.

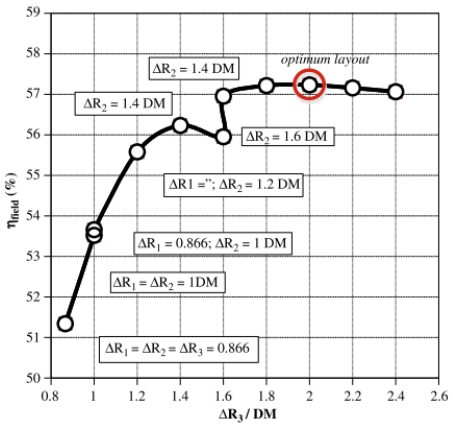

(c) Expanding the field and the result effect, here DM is the minimum distance between neighbouring heliostat centres to avoid collision.

Figure 2.17: Redesign of GemaSolar field using the Campo code (Collado and Guallar, 2013).

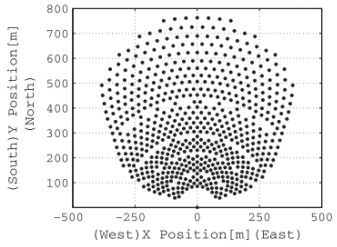

(a) PS10 field recreation using DELSOL.

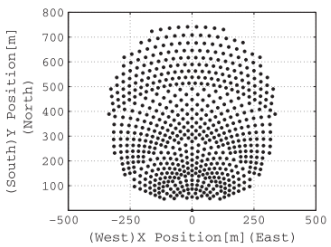

(b) PS10 optimised radial stagger layout.

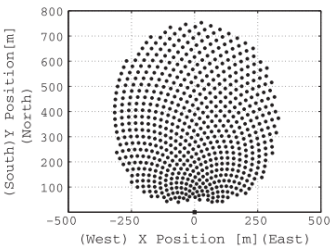

(c) Phyllotaxis spiral layout.

Figure 2.18: Comparison of PS10 field redesign (Noone et al., 2012).

Figure 2.19 shows plots of the radial stagger and spiral layouts. The colour in these plot depicts the minimum distance between a heliostat and its neighbours. It can be seen that the spiral layout has a continuously varying heliostat field density as a function of radial

distance from the tower. Whereas the radial stagger field, due its zones, is discontinuous. The continuous function better matches the efficiency of the field as a function of radial distance. For this reason the author claims that the field area of the spiral pattern is significantly less than the radial stagger layout.

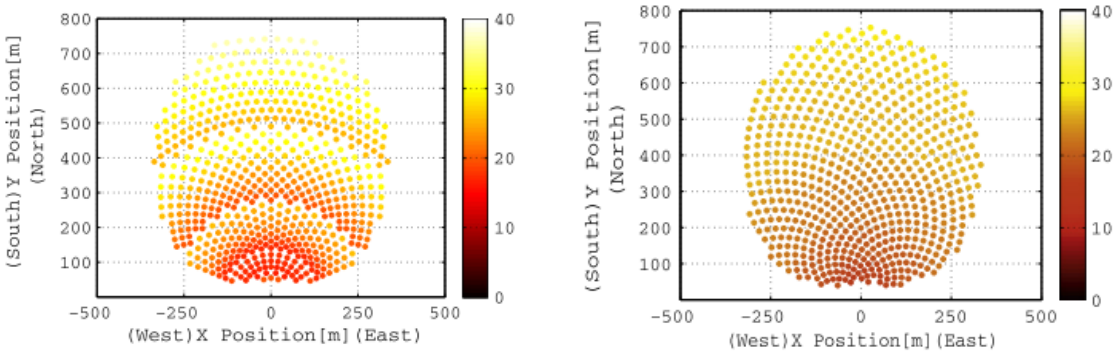

(a) Radial stagger layout.

(b) Phyllotaxis spiral layout.

Figure 2.19: Minimum distance between heliostats and neighbours (Noone et al., 2012).

2.7.2 Free variable method

Free variable heliostat field layout design optimisation, defines the design variables of the optimisation problem as the co-ordinates of every heliostat in the field. Therefore the number of design variables, n_{design}, are:

$$n_{design} = 2 \times n_{helios}, \tag{3}$$

where n_{helios} is the number of heliostats in the field. This approach leads to complex optimisation problems for large fields due to the curse of dimensionality.

Lutchman et al. (2014) applied a gradient based optimiser to show that the free variable approach leads to more optimal fields than an optimised pattern layout. The authors tested their approach by re-designing PS10 and reported an improvement in the optical efficiency of 1.2 % after 120 iterations, at a computational cost of approximately 1 hour per iteration. The free variable approach is clearly computationally extremely expensive, to this end the authors did advise this approach should only be selected if sophisticated optimisation algorithms and high performance computers were available (Lutchman et al., 2014). The original PS10 field layout and the Lutchman et al. (2014) redesign are shown in Figure 2.20.

2.7.3 Field growth method

The field growth method was implemented and explained by Sánchez and Romero (2006). The method divides the field into a grid of potential heliostat positions. Before any heliostats are placed the method determines the best positions in the field on a "yearly normalised energy surface" (YNES) based on the cosine, spillage and attenuation efficiencies of each grid position. The first heliostat is then placed at the best possible location. Next a new YNES is calculated, including the yearly-normalized shading and blocking effect of the first heliostat. Again, a heliostat is placed at the best location. This process

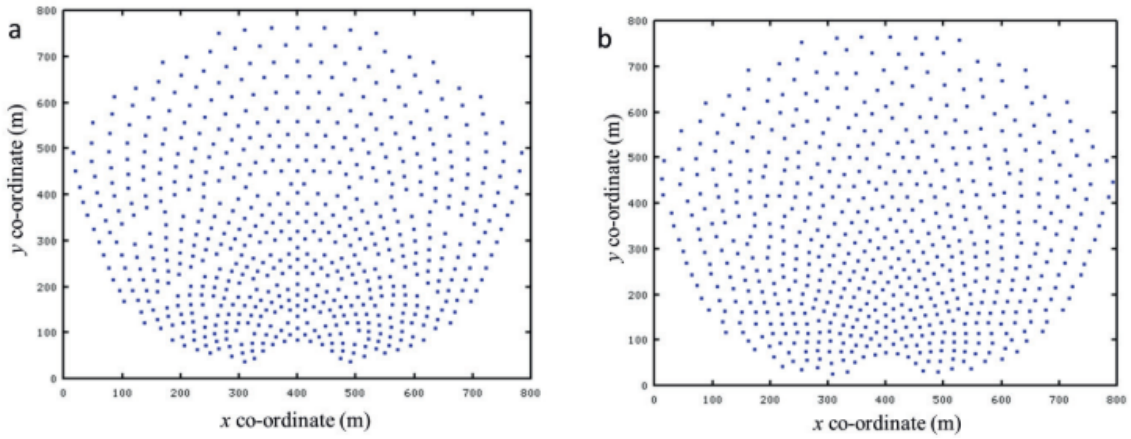

(a) PS10 field layout.

(b) Redesign PS10 field layout.

Figure 2.20: Free variable approach to heliostat field layout design optimisation (Lutchman et al., 2014).

is repeated, recalculating a new YNES after each heliostat is placed, until a sufficient number of heliostats are placed to meet the thermal demand.

Figure 2.21 shows the heliostat growth method implemented by Sánchez and Romero (2006). The figures show the annual optical efficiency potential of each position in the field. This is the so-called YNES, and must be recalculated after every heliostat placement.

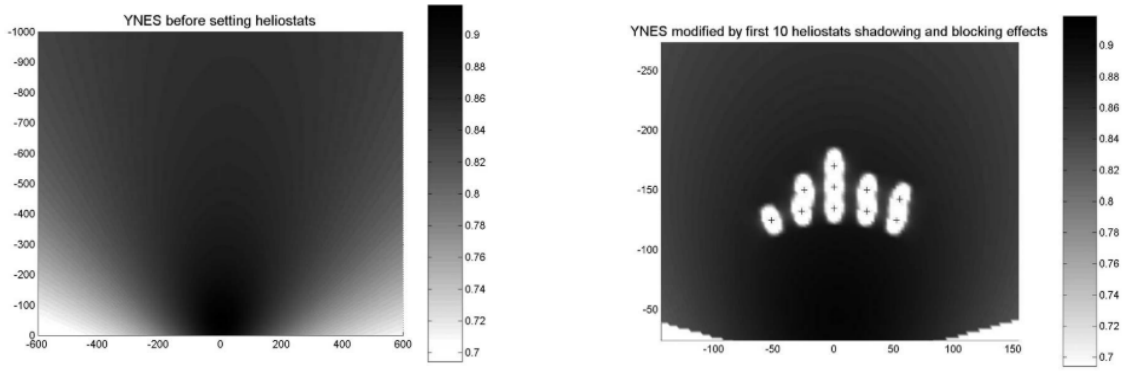

(a) Original YNES prior to heliostat placement.

(b) YNES, including shading and blocking effects.

Figure 2.21: Heliostat field growth method (Sánchez and Romero, 2006).

Sánchez and Romero (2006) compared their heliostat growth method against the field delivered by DELSOL. The two resulting field layouts are shown in Figure 2.22. The annual optical efficiency improves from 75.02 % to 78.84 %. However as can be see the field is significantly larger, 40 % larger.

2.7.4 Comparison of field layout routines

This sections compares the field layouts determined by various field layout design methodologies. Mutuberria et al. (2015) compared several heliostat field layout methodologies

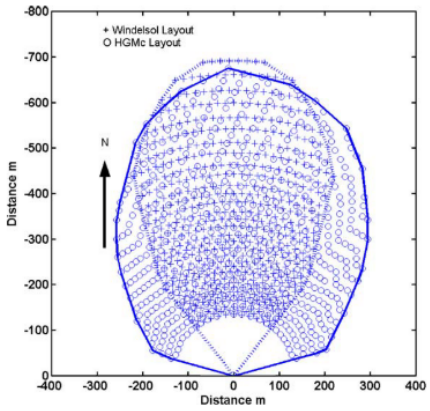

Figure 2.22: Field growth method (circles) vs DELSOL (pluses) radial stagger (Sánchez and Romero, 2006).

across three different plant sizes. A dense radial stagger, the Campo code, DELSOL and the biomimetic spiral (itself a Fermat spiral) were compared. The results showed that the Campo code and the biomimetic spiral consistently out perform the other field design methodologies. The authors compared the methodologies in terms of two competing objectives, annual optical efficiency and annual energy delivery. The results are shown on a Pareto front in Figure 2.23. The result may look strange at first as the energy collected is highest for fields with least optical efficiency. This is a consequence of field size, larger fields are required to collect more energy, but for increasing field sizes, the optical efficiency decreases as a consequence of guaranteed increasing attenuation and spillage losses.

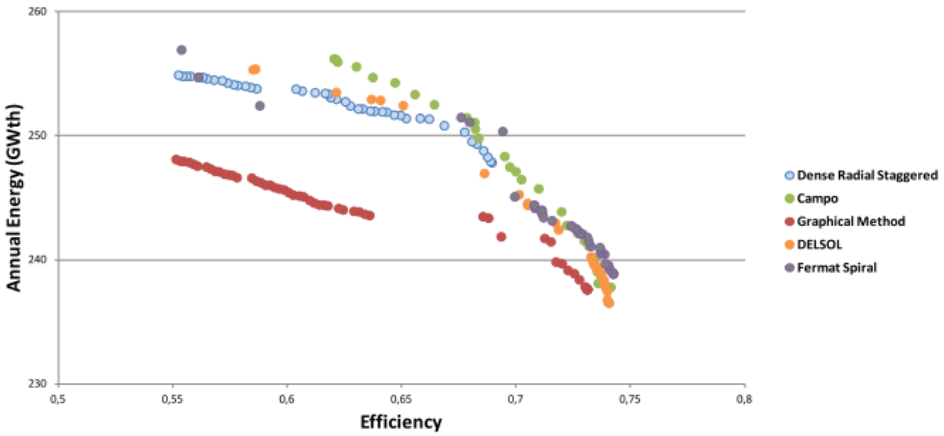

Figure 2.23: Comparison of field design methodologies (Mutuberria et al., 2015).

2.7.5 HelioPod™ field layout

There is very limited literature regarding the design of pod based heliostat field layouts. Domínguez-Bravo et al. (2016) discuss pod field layouts in the context of the Helio100 project, this field is limited to only 20 pods. The authors compared the existing field consisting of straight rows to three new designs. A new pattern method places the pods on radial rows, a free variable approach using a genetic algorithm and a field growth

method using a Greedy algorithm. The resulting fields are shown in Figure 2.24. The fields are ranked in order of descending performance; Greedy, genetic, radial pattern and cornfield. There was a 2 % difference in optical efficiency between the best and worst field.

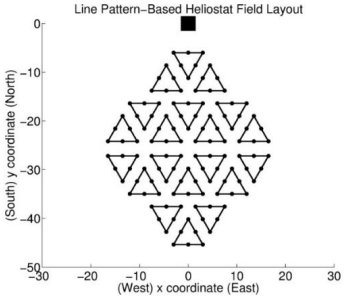

(a) Cornfield design.

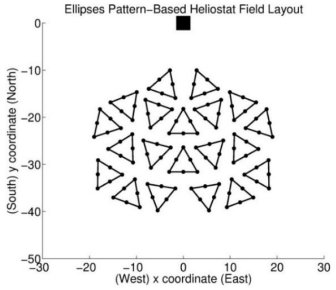

(b) Radial row field design.

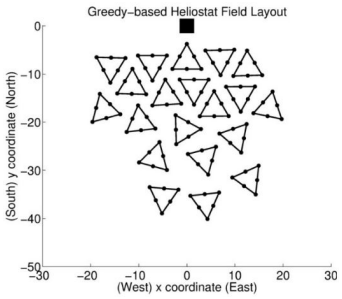

(c) Field growth design using a Greedy algorithm.

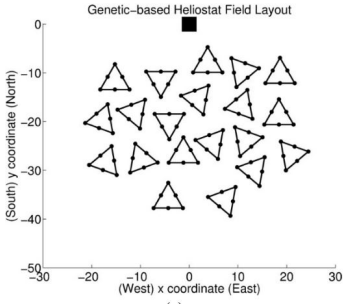

(d) Free variable design using a genetic algorithm.

Figure 2.24: Small HelioPod™ field designs (Domínguez-Bravo et al., 2016).

Ricklin et al. (2014) discussed the design methodology behind eSolar's pod based heliostat system. The system is shown in Figure 2.25. No diagram of the field layout is presented or any details of the field design methodology, but the authors do state that the envisaged field would consist of cornfield layout (straight lines with multiple rows) pods.

Figure 2.25: eSolar pod heliostat technology (Ricklin et al., 2014).

The only known work on the field layout for larger pod based fields is by Lubkoll et al.

(2018). The authors present a densely packed circular field layout. The pods are placed on straight rows in the same manner as Figure 2.24a, and the number of rows and width of each row is determined by a bounding circle. The layout can be seen in Figure 2.26, the presented fields contains 370 HelioPods™. The authors note no optimisation of the field layout was performed, this work represents an heuristic approach to the field layout design.

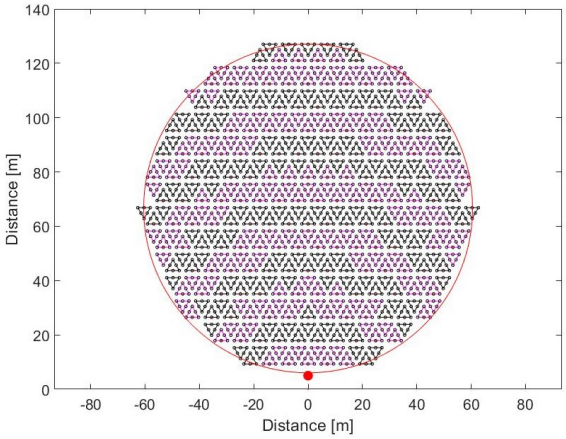

Figure 2.26: Densely packed pod field within a bounding circle (adapted from Lubkoll et al. (2018)).

2.8 Thermal energy storage dispatch optimisation

This section provides an overview of the TES dispatch methods implemented in literature. This is covered to aid in the formulation of the TES dispatch optimisation problem.

A body of literature exists for developing optimal TES dispatch profiles in order to shift electrical power production to higher value time periods (Wagner, 2015), (Sioshansi and Denholm, 2010) and (Wittmann et al., 2008). These models all optimise the profile separately for every day of the year, but optimise over an extended time-horizon to ensure the optimisation does not prioritize short-term gain and lose out on potential longer-term benefits, such as holding thermal energy back overnight to sell at a higher value period in the morning. This approach is called a rolling time-horizon optimisation. The models all assume perfect foresight of future available solar energy and electrical tariff prices.

Wagner (2015) developed a mixed-integer linear program as a solution to the dispatch optimisation problem for a CSP plant. The optimisation problem aims to maximize plant profits by determining the optimal discharge TES profile whilst penalizing the objective function to enforce some desirable operational requirements such as limiting power block and solar receiver cycling. The result of this work is the dispatch optimisation engine for the popular CSP modelling tool SAM (Blair et al., 2018). The authors showed that increasing the extended time-horizon for optimisation improved the result, up to a point, at which the increased dimensionality of the problem lead to worsening results. A 48 hour time-horizon was recommended to allow for foresight and realistic prediction of weather. The author investigated the value of the optimisation on various electrical tariff markets

(shown in Figure 2.27) and found the optimisation yielded most significant improvements compared to a heuristic strategy, for the two-tier and pool price tariffs.

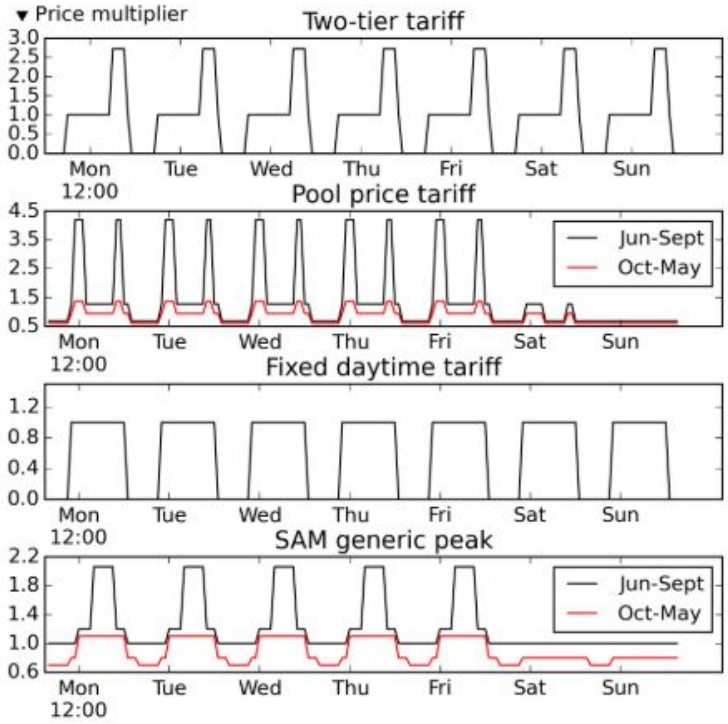

Figure 2.27: Various electrical tariff markets against which Wagner (2015) tested the dispatch optimisation.

Sioshansi and Denholm (2010) investigated the benefit of adding TES to CSP plants. The authors developed an energy flow model for the plant and implemented a mixed-integer program to determine an optimal TES dispatch profile, aimed at maximising revenue from electricity sold. The authors work showed that the TES increases the value of a CSP plant by allowing electricity production to be shifted to higher value hours. The authors also determined that by coupling TES to a set powerblock rating, that the solar field should be increased so that more energy can be captured (through TES charging) and shifted to higher value time periods.

Wittmann et al. (2008) developed an optimal TES discharge model for a CSP plant in Spain. At the time of writing renewable energy projects were paid a flat tariff for their energy, while conventional power plants operated in a so-called electricity stock exchange market, where the price paid to power producers depends on current demand. The authors investigated whether a CSP plant could achieve more revenue by competing on the electricity stock exchange, by utilizing TES to shift energy production to higher value periods. They developed an optimal discharge model for the plant in this market and showed improved revenue compared the flat tariff model. The authors showed that increasing TES for a set solar field size and power block rating leads to greater revenue as more high-value energy can be sold. The authors also investigated the impact of the length of foresight and found that increasing the number of days of foresight improved the result, but two days of foresight achieved the majority of the benefit.

Guedez et al. (2016) developed heuristic strategies for TES dispatch. These were tested on the first three electrical tariffs shown in Figure 2.27. Their heuristic focusses dispatch on peak tariff periods, and includes a method for determining peak hours. The heuristic methods work well, but both Wagner (2015) and Sioshansi and Denholm (2010) showed that optimised dispatch profiles outperform heuristic methods.

2.9 Identified gap in research

In Chapter 2.4 literature covering CST technologies for use as a process heat source were discussed. It was found that in the majority of these papers the specifics with regard to plant modelling, TES use and field layout design were only briefly mentioned. The central idea behind the bulk of the work is rather to use existing modelling tools to showcase the potential use case of the technology.

The author therefore identifies the gap in the existing research to be the specifics of TES dispatch and field layout design. Specifically this thesis requires the use of the HelioPod technology, for which the size fields required for the application (Manganese pre heating) have not been studied. The dispatch optimisation is performed in the unique context of providing a steady heat supply given the constraints of the local electric tariff. This is different to the bulk of TES dispatch optimisation literature, which focusses on providing a heat supply to a thermal-to-electric conversion process, so as to meet the electric power demand during peak demand hours.

The dispatch and field layout optimisation are the gaps identified where the plant's resulting LCOH, given the preselected components, could be most reduced by this research effort. These optimisation studies are an endeavour to investigate the best case scenario for CST provided process heat in the context of it being compared to low cost fossil fuel combustion.

3 Solar plant model

The CST plant model consists of three components: optical, energy and economic models. The optical model implements ray tracing methods to determine how much of the solar energy intercepted by the heliostat field reaches the receiver. This model accounts for all the optical losses experienced in the heliostat field, as well as the optical properties of the heliostats. The energy model is based on heat flows. The model tracks the energy incident on the receiver, through the TES and onto the pre-heater unit. The energy model utilizes efficiency terms to account for energy loss to the environment. The economic model determines the cost of heat produced over the plant's lifetime, accounting for all capital and operating costs.

The solar resource varies throughout the year and so does the sun's apparent position in the sky. This influences the optical performance of the heliostat field. To account for this influence solar thermal plant operations are simulated for a full year. This is typically implemented as a pseudo steady-state model, where the solar resource and sun position changes with hourly resolution (Lovegrove and Stein, 2012).

Figure 3.1 depicts the various components of the plant. The plant consists of the heliostat field, receiver, thermal energy storage and back-up electrical heaters. Incorporating pre-heating into the furnace operations requires that the ore is always pre-heated in order to keep the furnace operating conditions steady. Therefore the plant design includes auxiliary backup electric heaters. At any point when the receiver and/or TES cannot deliver the rated load, the backup heaters will supplement the output.

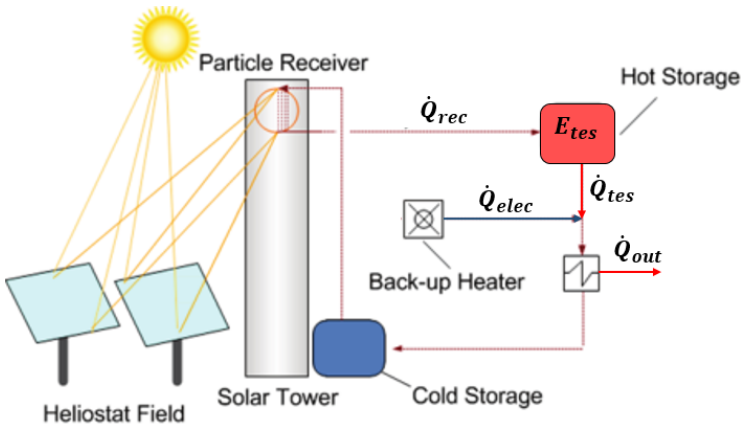

Figure 3.1: CST plant layout (adapted from Amsbeck et al. (2017)).

The next few subsections describe the optical, energy and economic models, this provides a comprehensive overview of how the models interact. After this some further detail about the optical model implementation and validation are presented.

The work presented in this chapter has been published as a peer-reviewed conference paper from the American Society of Mechanical Engineers International Conference on Energy Sustainability 2020 (Mckechnie, McGregor, and Venter, 2020).

3.1 Optical model

The optical model determines how much of the irradiation incident on the heliostat field is successfully reflected onto the receiver aperture. This is dependent on the available solar energy, the sun's position, the field layout geometry and the heliostat's optical properties. The model accounts for all the optical losses: blocking, shading, spillage, attenuation and cosine. The optics of the field is modelled using a solar ray tracer tool called SunFlower (Richter et al., 2018). The tool was developed by a research group at RWTH Aachen University, and a beta version was shared for use in this thesis. This ray tracer was validated against two popular existing tools, Tonatiuh and SolarPilot, in Appendix B.

The ray tracer requires the user to input the sun position, the amount of solar radiation, the receiver geometry, the heliostat field geometry and optical properties. For the given plant geometry the tool then determines the energy incident onto the receiver. This is repeated for each time-step. Therefore solar resource data and the sun's location must be determined for input to the ray tracer.

3.1.1 Sun's energy

The energy of the sun has two aspects: the amount of irradiation reaching the ground and the variation of intensity of irradiation across the sun's face, known as the sunshape (Stine and Geyer, 2001). As discussed in section 2.2.2, the available irradiation (W/m^2), in hourly resolution for the entire year, can be retrieved from a TMY file. For the work in this thesis the TMY data is retrieved from Meteotest (n.d.), a commercial solar resource database. A typical sunshape model, the Buie sunshape, is used to model the varying intensity across the sun's surface (Buie et al., 2003).

3.1.2 Sun's position

The sun's apparent position in the sky is determined using an algorithm from Stine and Geyer (2001). The position of the sun is defined using two angles, the azimuth (A) and elevation (α) angles. These angles can be seen in Figure 3.2. To determine the sun's apparent position for a certain location and time, a number of intermediate angles and parameters are first calculated before azimuth and elevation angles can be determined.

The declination angle, δ, defines the angle between a line from the sun's centre to the earth's centre and the equator. This varies throughout the year to a maximum at the solstices, and a minimum (zero) on the equinoxes. The declination angle can be determined for each day:

$$\sin(\delta) = 0.39795 \cos(0.98563(N - 173)), \tag{4}$$

where N is the day number of the year, with 1st January starting at 1.

The sun's elevation, α, is the angle at which the sun is above the horizon. The elevation is a function of the declination angle, site latitude and the time of day:

$$\sin(\alpha) = \sin(\delta)\sin(\phi) + \cos(\omega)\cos(\phi), \tag{5}$$

where ϕ is the latitude of a location and ω is the hour angle.

The hour angle is a function of the solar time, t_S. Solar time defines solar noon when the sun is directly North, therefore solar time is location specific. As a consequence of

standardizing time for large geographical regions solar time and local clock time differs. The hour angle is determined from the solar time:

$$\omega = 15(t_s - 12) \tag{6}$$

Once the previous angles are known the sun's azimuth angle, A, can be found.

$$A = \begin{cases} 360° - \arccos\left(\frac{\sin\delta\cos\phi - \cos\delta\cos\omega\sin\phi}{\cos\omega}\right), & \text{if } \sin\omega > 0 \\ \arccos\left(\frac{\sin\delta\cos\phi - \cos\delta\cos\omega\sin\phi}{\cos\omega}\right), & \text{if } \sin\omega \leq 0 \end{cases} \tag{7}$$

Using these equations the sun's position in terms of azimuth and elevation angles can be determined for every hour of the year, as required for the model. The azimuth and elevation angles are shown in Figure 3.2.

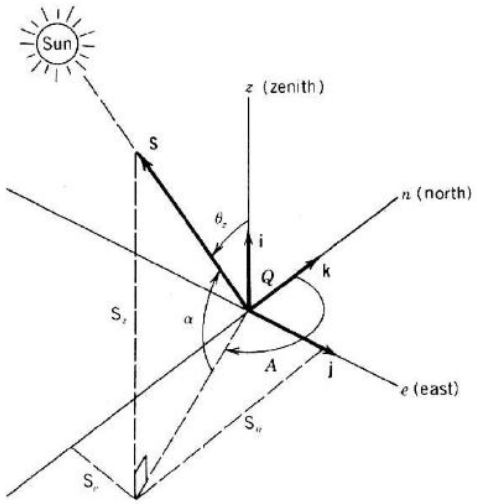

Figure 3.2: Angles defining the sun's apparent location in the sky (Stine and Geyer, 2001).

3.1.3 Optical efficiency determination

The sun's location and the available irradiation is passed to the ray tracer, from which the incident power on the receiver aperture is determined. From these values the heliostat field's instantaneous optical efficiency can be calculated. The optical efficiency parameter, η_{opt}, describes the fraction of irradiance incident on the heliostat field that reaches the receiver. This parameter encapsulates all the optical losses of the heliostat field. The instantaneous optical efficiency is determined as:

$$\eta_{opt_i} = \frac{\dot{Q}_{rec_i}}{\dot{q}_{dni_i} A_{sf}}, \tag{8}$$

where $\dot{Q}_{rec_i}$ is the power reflected onto the receiver aperture, $\dot{q}_{dni_i}$ is the direct normal irradiance for each time-step i and A_{sf} is the total solar field aperture area. In other words the numerator represents the power reaching the receiver and the denominator represents the power incident on the field.

3.1.4 Annual optical efficiency meta-modelling

The optical model requires the optical efficiency for every sun hour of a year. Ray tracing is computationally expensive therefore a subset of the sun hours of the year are simulated and a meta-model is fitted to this data. Future instantaneous optical efficiency data is then obtained from the meta-model. This meta-modelling approach is compared to a full year simulation to evaluate the meta-model accuracy.

The model defines the field optical efficiency in terms of the sun's location; azimuth and elevation angles. Three days are simulated; winter and summer solstice and spring equinox. The solstices define the maximum (summer) and minimum (winter) elevation and azimuth angles for the year. Equinox is the day exactly in-between the solstices and so has sun angles in-between the maxima and minima angles of the solstices. These days were simulated with hourly resolution using the ray tracer to determine the the optical efficiency. A piece-wise linear interpolant surface was then fitted to this data as shown in Figure 3.3. The LinearNDInterpolator function from Python's scientific computing package, SciPy, was used for this (Oliphant, 2007). The pink circles from Figure 3.3 shows the data from the optical model for the three completely simulated days. Each 'horseshoe' of pink circles represents a day. The meta-model optical efficiency for any time of the year will be found on this surface, as the surface bounds around all possible sun angles. This approach was used by Lubkoll et al. (2018). Note that the terms elevation and altitude angle is used interchangeably in solar literature.

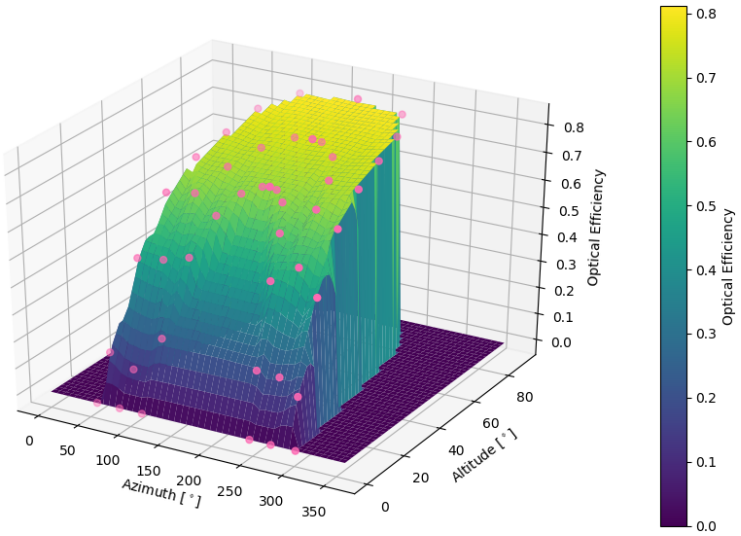

Figure 3.3: Field optical efficiency as a function of sun position.

The hourly simulation determines the optical efficiency for each hour of the day in terms of local clock time, not solar time. This means solar noon, which represents the moment when the sun is due north and highest in the sky, might not be simulated. This would cause the meta-model to be incorrect as it would not provide a true bound of possible sun angles. For this reason solar noon is additionally simulated.

After the meta-model has been fitted to the simulated data, the instantaneous optical

efficiency, η_{opt_i}, is a function of the sun's position:

$$\eta_{opt_i} = f\left(\alpha_i, A_i\right), \tag{9}$$

where α_i is the elevation angle and A_i is the azimuth angle.

Once the meta-model has been determined, a TMY file containing solar resource data, the meta-model function and the reflective area of the heliostat field can be used to determine the power incident on the receiver for every sun light hour of the year (using Equation 8). This data is then passed to the energy model. This meta-model is only valid for the simulated heliostat field, and must be regenerated for any change. Changes in heliostat field layout, optical properties, geometry or plant location would necessitate a new meta-model.

3.1.5 HelioPod™ optical characteristics

In order to model the HelioPod™ a number of optical parameters are required. These are used by the ray tracer to define the optical performance of the heliostat. Table 3.1 provides the technical specifications for the HelioPod™ technology. Of relevance to optical modelling are the surface slope and tracking error and reflectivity.

Table 3.1: HelioPod™ specifications.

Parameter	Value	Units
Number of heliostats per pod	6	
Single facet aperture area	1.83×1.22	m^2
Facet focal length	Variable	
Tracking	Dual axis	
Drives	2×Linear actuators	
Foundations	None	
Combined surface slope and tracking error	< 1.5	mrad
Reflectivity	95	%

All data from Lubkoll et al. (2018).

3.2 Energy model

Figure 3.1 includes labels for all energy flows relevant to the model. The energy model for the plant is based on energy balances of the various plant components. The receiver and thermal energy storage are modelled with efficiency values to account for the thermal losses experienced by these components.

The optical model determines the optical efficiency of the heliostat field by simulating a subset of days of the year and producing a meta-model. Next, the sun's position for every hour of the year is determined using equations 4 - 7. The sun positions and meta-model are then used to determine the power incident on the receiver for every hour of the year:

$$\dot{Q}_{rec_i} = \eta_{opt_i} q_{dni_i} A_{sf} \text{ [W]}, \tag{10}$$

where η_{opt_i} is the field optical efficiency as determined by the optical model, q_{dni_i} is the available direct normal irradiation which is taken from a TMY file and A_{sf} is the aperture area of the heliostat field.

The energy in the thermal energy storage is determined by accounting for the energy loss between the receiver aperture and the ceramic particles, the energy already in storage, the heat loss from storage and how much is energy has been discharged. The energy balance for the TES is:

$$E_{tes_i} = \eta_{rec_i} \dot{Q}_{rec_i} \Delta t + \eta_{tes} E_{tes_{i-1}} - \dot{Q}_{tes_{i-1}} \Delta t \text{ [Wh]}, \tag{11}$$

where E_{tes_i} is the energy in storage, η_{rec_i} accounts for heat losses from the receiver, η_{tes} accounts for heat loss from storage and $\dot{Q}_{tes_{i-1}}$ is the discharge from storage. Δt is the time-step for which all variables are assumed constant. The subscripts indicate the relevant time-steps. This energy balance follows the modelling methodology of Wagner (2015), Sioshansi and Denholm (2010), Wittmann et al. (2008) and Lubkoll et al. (2018).

In cases where the power incident on the receiver exceeds its thermal rating, the energy model will curtail this excess energy. In reality the heliostat field would defocus, avoiding overloading the receiver. If energy is available to the TES but the TES is at full capacity, the energy will also be curtailed.

The thermal energy output to process is the combination of heat from the thermal energy storage and the back up electrical heaters:

$$\dot{Q}_{out} = \dot{Q}_{tes_i} + \dot{Q}_{elec_i} \text{ [W]}, \tag{12}$$

where $\dot{Q}_{out}$ is the output to process and $\dot{Q}_{elec}$ required backup electrical derived heat. The exact amount of heat supplied from storage and from the electrical backup heaters is determined by the operating strategy of the plant, this is discussed in the following chapter.

Note that for the purpose of this work the electric-to-thermal conversion efficiency, η_{conv}, for hot air generation by the auxiliary heaters is assumed to be 100 %. Therefore:

$$Q_e = \eta_{conv} P_e \tag{13}$$

where P_e is the electric energy.

In concentrating solar literature a parameter known as the solar multiple (SM) is used to define the size of the solar field relative to its load, typically a turbine for a CSP plant. SM is defined by Lovegrove and Stein (2012) as:

$$SM = \frac{\dot{Q}_{des,field}}{\dot{Q}_{out}}, \tag{14}$$

where $\dot{Q}_{des,field}$ is the power delivered to the receiver at a design condition and $\dot{Q}_{out}$ is the power demanded by the pre-heater unit, the field's load. In this thesis the solar design condition for the fields is 1 000 W/m^2 at solar noon on equinox. Typically the denominator is the constraint on equation 14 (a thermal requirement for a desired turbine size in a CSP plant) but the optimal demand from the CST plant will be determined through a parametric study in order to design the CST plant for the case study.

3.2.1 Receiver modelling parameters

Amsbeck et al. (2014a) and Wu et al. (2015b) state the CentRec© receiver is capable of achieving a near constant particle outlet temperature of 900 °C irrespective of the incident solar flux. This is achieved by controlling the mass flow rate of the particles, increasing the mass flow rate when the incident flux is high and decreasing the mass flow rate when the flux is low. This was confirmed during prototype testing Wu et al. (2015a). Ebert et al. (2018) discussed the performance of a full scale CentRec© during on-sun testing. The full scale testing showed that the desired particle outlet temperatures was possible for a range of solar fluxes.

For modelling purposes, the solar to particle heat transfer can be simplified as a solar to particle thermal efficiency, which is dependent on the incoming solar flux. The assumption is made that the particle outlet temperature is always 900 °C, irrespective of incident solar flux.

Wu et al. (2015b) developed a detailed FEM thermal model of the receiver. The results are shown in Figures 3.4a and 3.4b. These figures show the solar to particle thermal efficiency of the CentRec© receiver for a range of incident solar fluxes, and two different receiver tilt angles. The thermal losses of the receiver are also shown. These characteristic curves are used to determine the receiver thermal efficiency for the model. Additionally, it can be seen that there is little difference resulting from the different tilt angles.

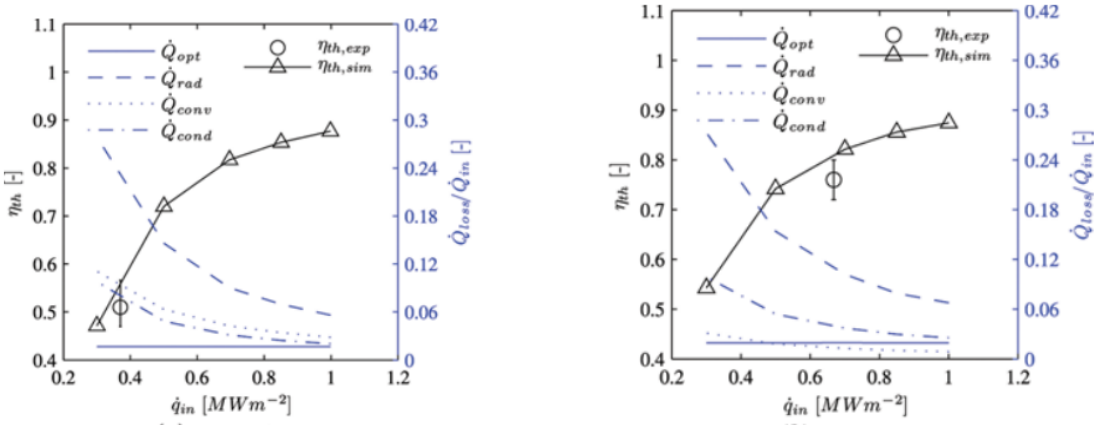

(a) Particle outlet temperature of 900 °C and inclined at 45 °.

(b) Particle outlet temperature of 900 °C and inclined at 90 °

Figure 3.4: CentRec© solar to particle thermal efficiency (Wu et al., 2015b).

Table 3.2 shows the specifications of the commercially sized 2.5 MW_{th} CentRec© receiver. These specifications will be used for modelling the receiver. For the optical model the receiver will be modelled in the ray tracing environment as a tilted disk. The disk represents the receiver aperture. This follows the modelling methodology of Lubkoll et al. (2018).

Table 3.2: CentRec© receiver specifications from (Ebert et al., 2016).

Parameter	Value	Units
Aperture area	1	m^2
Rated load	2.5	MW_{th}
Outlet temperature	900	°C

3.2.2 TES modelling parameter

The thermal energy storage (TES) consists of two insulated particle storage bins, a hot and a cold bin. Palacios et al. (2019) reports this storage concept is capable of storage temperatures in excess of 1 000 °C whilst using low-cost materials. El-Leathy et al. (2013) published test findings of a small scale rectangular particle storage bin consisting of insulating firebrick and concrete. The daily heat loss was reported to be 4.4 %. Al-Ansary et al. (2014) used these results to further develop the concept, introducing a cylindrical bin consisting of a concrete and refractory cement construction. The authors published results of a numerical model for this new design, where the daily heat loss was reported to be 4.3 %. El-Leathy et al. (2013) and Al-Ansary et al. (2014) both predict the heat loss to reduce to 1 % for a utility-scale TES bin. Therefore the hourly heat loss is modelled as a thermal efficiency, η_{tes} for the TES. The predicted value of 1 % energy loss over 24 hours for commercial bins is used.

3.3 Economic model

The economic model builds on the results from the optical and energy models. The plant's configuration and final energy discharge profile is used to determine the economic performance. These results are used as the objective function of the field layout optimisation and plant configuration design for the case study.

3.3.1 Levelised cost of heat

Levelised cost of heat (LCOH) is a parameter analogous to the widely used levelised cost of electricity. The parameter provides the cost per unit heat generated. LCOH is determined by accounting for the full lifetime costs of the plant; capital expenditure and operating and maintenance, and dividing these costs by all the energy generated by the plant over its lifetime. The LCOH allows different technologies with different operating principles and lifetimes to be compared (Short et al., 1995).

The combined solar-electric nature of the plant requires the calculation of an LCOH for both the solar and electric components. A combined LCOH is then determined by the energy weighted average of solar and electric heat respectively.

The solar levelised cost of heat, $LCOH_s$, is calculated as follows:

$$LCOH_s = \frac{\left(\frac{k_d(1+k_d)^n}{(1+k_d)^n-1} + k_{ins}\right) \times CAPEX + O\&M}{Q_s} \; [\$/\mathrm{MWh_t}], \tag{15}$$

where k_d is the discount rate, n is the discount period, k_{ins} is the insurance rate, $CAPEX$ is the total capital expenditure for all equipment, $O\&M$ is the operating and maintenance

cost and Q_s is the total solar energy produced by the plant. This equation is from the work of Short et al. (1995), and is based on the assumption that the plant will deliver the same energy for every year of its lifetime.

The electric plant costs are approximated as only the 'fuel' costs, i.e. the cost of purchased electricity. This approximation is used as the fuel cost is expected to be significantly larger than the equipment capital cost. The electric levelised cost of heat, $LCOH_e$, is calculated as follows:

$$LCOH_e = \frac{\sum_{i=1}^{8760} \dot{Q}_e C_i}{Q_e} \text{ [\$/MWh}_\text{t}\text{]}, \tag{16}$$

where $\dot{Q}_e$ is the electrical-derived thermal power bought at time-step i, C_i is the electric tariff cost at the relevant time-step and Q_e is the total electrical-derived thermal energy required over the year.

The combined solar-electric levelised cost of heat, $LCOH$, is computed as the energy weighted average of $LOCH_s$ and $LOCH_e$:

$$LCOH = \frac{LCOH_s Q_s + LCOH_e Q_e}{Q_s + Q_e} \text{ [\$/MWh}_\text{t}\text{]} \tag{17}$$

3.3.2 Plant cost assumptions

A number of different capital expenditures and other costs are assumed for the economic model. These costs are collectively shown in Table 3.3. The majority of the costs are CAPEX associated with the receiver and storage. These costs are estimated by Amsbeck et al. (2014a). These authors are from the DLR, the developer of the receiver technology. The heliostat field costs are taken from the economic model of Lubkoll et al. (2018).

Table 3.3: Economic model cost assumptions.

CAPEX	Value
Heliostat[1]	112.5 \$/m^2
Receiver[2]	138 130 \$/m^2
Vertical particle transport[2]	140 892 \$ per tower
Horizontal particle transport[2]	248 634 \$ per tower
Tower[2]	$8\,288 + 1.73 \times {h_{tower}}^{2.75}$ \$ per tower
Thermal energy storage[2]	20 443 \$/MWh$_\text{th}$
Particle-to-air heat exchanger[2]	138 130 \$ /MW$_\text{th}$
Plant lifetime[2]	25 years
Indirect costs[1]	22 % of CAPEX
O&M[1]	3.9 % of CAPEX
Insurance rate[1]	1 %
Discount rate[1]	7 %

[1] from Lubkoll et al. (2018)
[2] from Amsbeck et al. (2014a)

3.4 Model implementation and validation

This sections describes the details behind some aspects of the model implementation. The validation of the annual optical efficiency modelling methodology is provided. The Sunflower ray tracer does not provide the correct geometry for modelling the CentRec©, so a simple solution is described and the validation results are presented. Finally a convergence study for the number of simulated rays is presented.

3.4.1 Optical efficiency meta-model validation

To validate the meta-model approach detailed above a test scenario is simulated. The test scenario simulates a field with 216 HelioPods™, arranged in the field layout methodology described by Lubkoll et al. (2018).

To validate the meta-modelling approach for determining the optical efficiency, all 365 days are simulated with the Sunflower ray tracer to determine the power incident on the receiver. Next the meta-model method is implemented.

In Figure 3.5 the simulated and meta-model optical efficiency results can be seen for a subset of 5 days of the year. The difference between the simulated and meta-model results is indistinguishable. The second figure shows the relative difference between each simulated and meta-model point. All results are within 2 %.

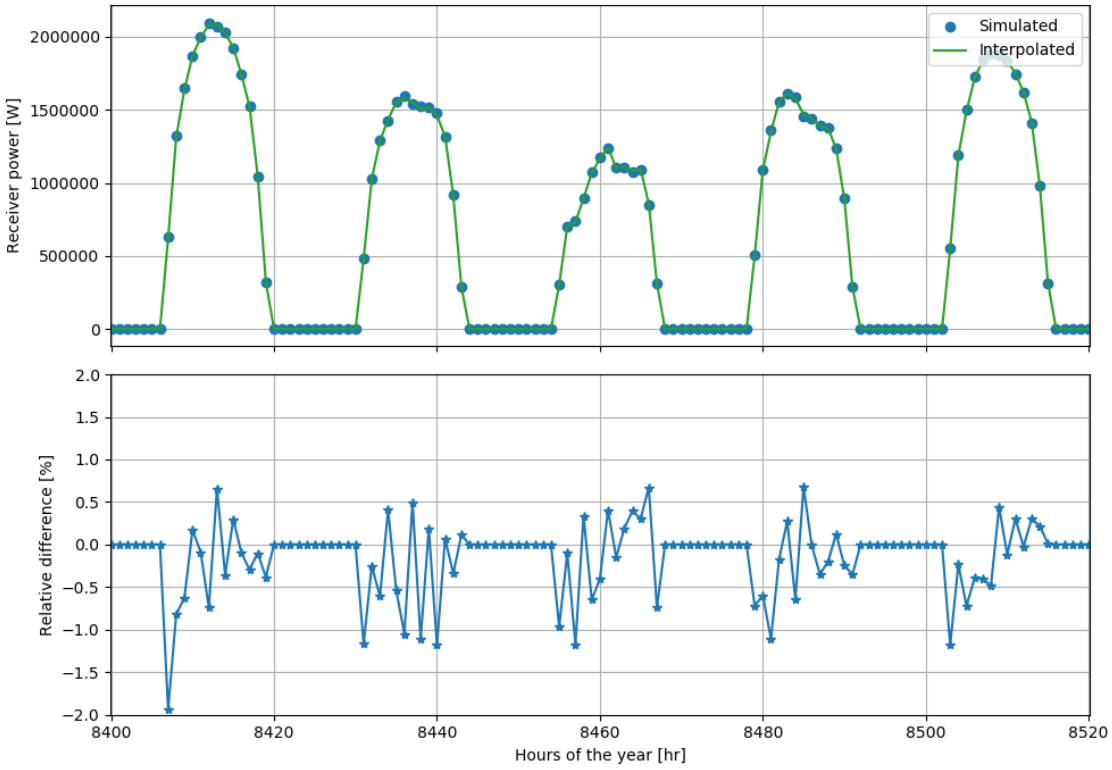

Figure 3.5: Field optical efficiency; meta-model vs simulated results.

Table 3.4 summarises the comparison between the simulation and meta-model results by considering the total annual result for each. The annual average difference for the receiver

energy and field optical efficiency amount to a 2.19 % lower value for the meta-model results. The instantaneous differences vary from lowest at the simulated days (solstices and equinox), where both methods provide the same results, to maximum, away from the simulated days, where the meta-model is least accurate. The overall difference of 2.19 % is deemed acceptable due to the decrease in computational time for an annual simulation. The reduced computational expense is required for the field layout optimisation in later chapters.

Table 3.4: Annual simulation.

Method	Simulation	Meta-model
Annual receiver energy	4 028 MWh	3 940 MWh
Annual optical efficiency	49.33 %	48.25 %
Computation time	26 115 s	278 s
Relative difference in energy and efficiency	-	-2.19 %

3.4.2 Sunflower receiver model shape correction

The receiver is modelled as a tilted flat disk - the shape of the aperture. However the Sunflower ray tracer only allows for rectangular tilted planes. A simple solution is to finely discretize a rectangular plane, and only keep the results for the discretized areas that fall within the area of the disk. This is possible as the Sunflower tool allows the user to specify the discretization of the receiver.

Figure 3.6a shows the implementation of this solution. The square grid represents the simulated receiver aperture. The green circle represents the area of the disk. Blue circles show the areas and their values which are kept toward the total incident power. Red squares fall outside the disk, meaning any reflected sun rays hitting these locations would miss the CentRec's© aperture, and therefore are not included toward the incident power. For each moment simulated the discretized receiver flux map is corrected using this approach. Figure 3.6b presents the results for a parametric study of the receiver discretization factor. Any grid finer than 10 by 10 is sufficient.

To validate this approach the test scenario as previously described is simulated in Tonatiuh and Sunflower. Tonatiuh has a large selection of geometries which can be simulated, including a disk. An annual simulation is performed using Tonatiuh with a disk, and Sunflower with the disk correction method. The results are shown in Table 3.5. The results for annual receiver energy and annual optical efficiency from the two ray tracers are within 2 %. This is deemed sufficiently accurate. Sunflower is the only ray tracer that can be used for the pod heliostat field layout optimisation as existing field layout optimisation tools do not allow for pods to be used. Detailed optical analysis can always be performed using Tonatiuh after the optimisation work to validate the final result. These results were produced using a 20 by 20 grid for the receiver in Sunflower.

Table 3.5: Comparing ray tracer results to validate receiver shape correction.

Ray Tracer	Annual receiver energy	Annual optical efficiency	% diff
Tonatiuh	3 875 MWh	47.44 %	-
Sunflower	3 940 MWh	48.25 %	+1.68 %

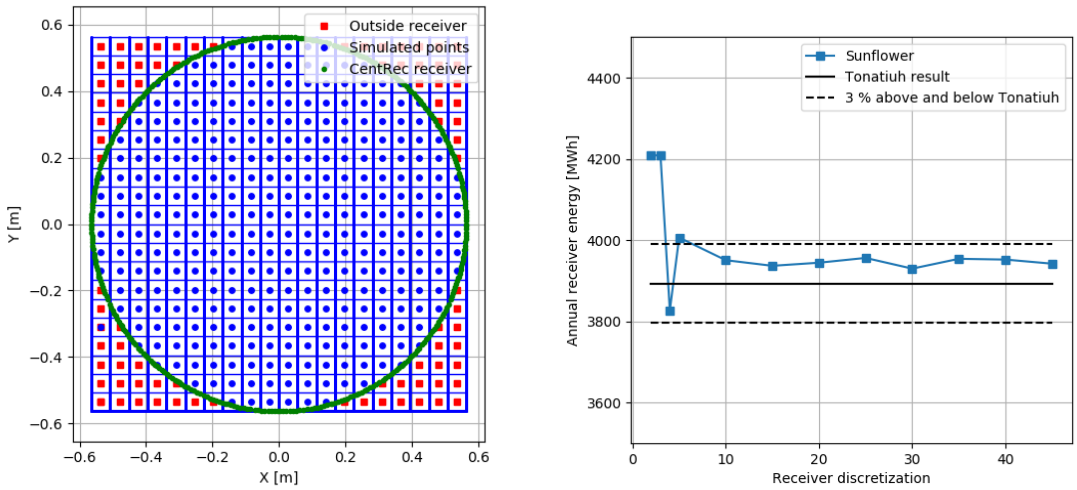

(a) Discretized receiver aperture.

(b) Receiver grid size parametric study.

Figure 3.6: Rectangular to circular receiver correction.

3.4.3 Ray tracer grid refinement

The Sunflower ray tracer implements hierarchical ray tracing. This approach is described in the work of Noone et al. (2012). Hierarchical ray tracing discretizes each facet surface and has ray origins at the center of each discretized area. Compared to traditional solar ray tracers which are Monte-Carlo simulations with rays originating at the sun's position, this approach is computationally faster. This is because less rays need to be simulated. Monte-carlo ray tracers rely on a large number of rays, some which do not intersect the heliostats and therefore do not contribute to the reflection modelling. For either ray tracer a sufficient number of rays are required to reach convergence of reported incident power on the receiver.

Figure 3.7 depicts the heliostat surface discretization employed by the Sunflower ray tracer and the parametric study results to determine the discretization required for the test scenario. From Figure 3.7b it can be seen that the results converge around a 5×5 grid. For the field layout optimisation a 4×4 grid is used due to the significant increase in computational expense for finer grids and the relatively small improvement in accuracy. The computational expense of simulating the points for the meta-model increases from 277 s to 809 s for a 4×4 versus 5×5 grid.

3.5 Modelling implementation conclusion

The modelling and optimization approaches developed in this thesis consist of a mix of off-the-shelf simulation tools and optimizers and self-implemented models. The energy and economic models, sun location algorithm, heuristic approach to annual field efficiency determination and field pattern layout algorithms are self-implemented. These codes are integrated with an off-the-shelf ray-tracing tool (Sunflower) and Scipy and DOT's optimisers (discussed in the next two chapters). This hybrid approach to modelling, simulation and optimisation is necessary due the use of the HelioPod technology and to model a

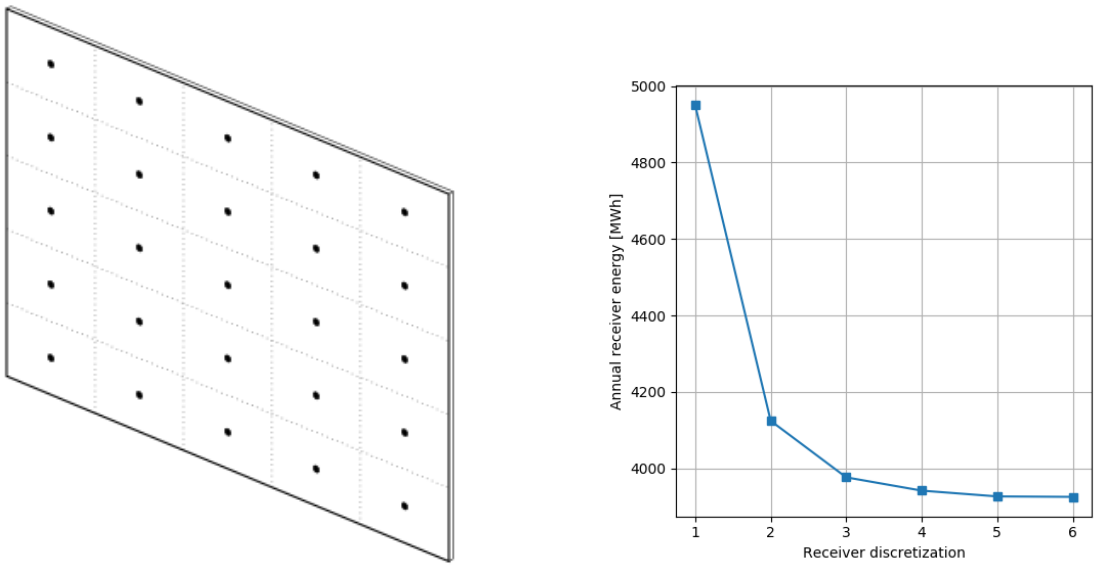

(a) Discretized facet (Richter et al., 2018).

(b) Facet discretization parametric study.

Figure 3.7: Heliostat discretization and result convergence study.

plant for process heat generation. At the time of writing existing modelling and solar ray-tracing tools such as SAM, SolarPILOT and Tonatiuh can not perform this analysis. These tools are aimed at modelling plants for power generation and generally only use standard heliostat fields, especially for field layout optimisation.

4 Operating strategy

This section describes the operating strategy developed for the CST plant. To meet the need for continuous process heat demand electric backup heaters are added to the plant. During times of insufficient solar derived heat the electric heaters will supplement the supply. The combined solar-electric system will ensure a 100 % capacity factor for the pre-heater unit.

In South Africa key industrial consumers (large power users) are subject to a time-of-use electric tariff. As a consequence the backup electric heat cost will depend on the time of purchase. In section 2.8 an overview of thermal energy storage dispatch optimisation schemes was presented. These schemes were implemented to maximise the revenue of CSP plants selling power. These works were used to develop a similar optimal dispatch profile but where the objective was to minimise the cost of supplied heat.

The main idea of TES dispatch optimisation is to decouple the use of solar heat from the time periods when the solar resource is available. The goal of this optimisation is to ensure electric heat is only bought when the tariff is low. As the solar derived heat cost is fixed irrespective of when its used, using the lowest cost electric heat provides the least cost combined solar-electric heat.

4.1 Electric tariff

Eskom's key industrial customers who operate energy intensive processes are subject to the Megaflex tariff (Mahony and Baartmanm, 2018). The tariff structure is shown in Figure 4.1. For Monday to Saturday, the tariff changes throughout the day, with a distinct morning and evening peak. Sunday's tariff is constant throughout the day, at the lowest rate. Two demand seasons are defined; a low and high demand season. The tariff structure remains similar between the two seasons, but the values are significantly increased during the high demand season. The high demand season is from June to August, with the rest of the year classified as low demand season.

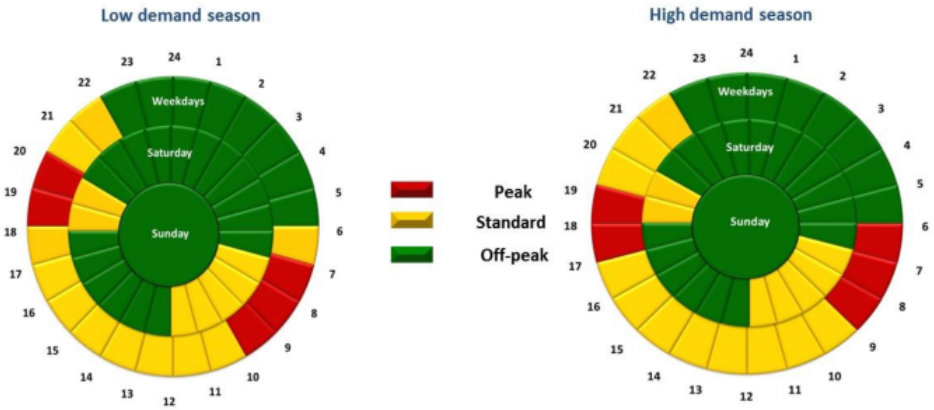

Figure 4.1: Megflex time-of-use electrical tariff structure (Eskom, 2019).

The tariff structure can be seen in more detail in Figure 4.2. The dataset used to generate this figure was constructed from the charts of Figure 4.1 and the cost tables from

Eskom's annual charges and tariffs booklet (Eskom, 2019). The weekday tariff structure is characterised by a peak tariff in the morning, followed by a mid-level tariff from late morning to afternoon, a second peak tariff period in the evening and then lowest tariff from late evening to early morning. Saturday's structure consists of a morning and evening mid-level, with the rest of the day at lowest rate. Sundays have a flat tariff at off-peak rates. The high-demand season peak tariffs are significantly higher than those for the low-demand season. The standard and off-peak tariffs differ, but not as significantly. The dispatch optimisation will aim to minimize the electric heat bought during the high tariff peaks, by discharging the TES during these periods.

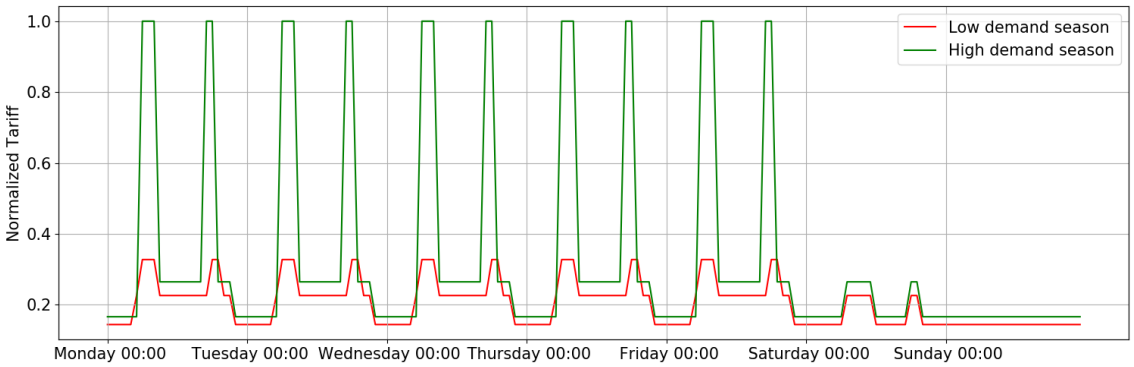

Figure 4.2: Megaflex time-of-use electrical tariff structure.

4.2 Heuristic dispatch strategy

Guedez et al. (2016) showed an heuristic strategy can be developed for determining an effective TES dispatch profile. A simple strategy would be to use any and all solar energy when it is available, to meet the process heat demand. Such a strategy would immediately start discharging solar heat to the process as soon as it is available, and would continue doing so until the TES is depleted in the evening. This is similar to the strategy used by Lubkoll et al. (2018). At times when the solar heat is insufficient to meet the full demand, the electric backup heaters would supplement the shortfall. This heuristic strategy will be used as a reference strategy for comparison against the optimised dispatch profile.

Figure 4.3 outlines how the simple heuristic strategy is implemented. Diamond blocks represent decisions and rectangular blocks represents actions. Each block is numbered for ease of reference. This logic is executed at each time-step of the simulation. Block 1.0 determines if the collective energy in storage and coming from the receiver is greater than or equal to the energy required by the process. In the case where this is false there is not sufficient energy available to meet demand, then block 1.1 is executed. The action in block 1.1 is to output the total energy from the receiver and in storage, to the process. The new storage level is then zero. In this scenario the electric backup heater will cover any shortfall. In the case where the decision in block 1.0 is true then there is more energy available than required by the process at this time-step, then block 1.2 is executed. The action of block 1.2 is to output the full demand to the process and use any excess energy to charge the TES. The new storage level is equal to the previous time-step's level, minus the output to process. In block 1.2.1, the TES level is checked to ensure it has not been filled over capacity, if this is true then block 1.2.2 is executed. Block 1.2.2 sets the TES

level to its max level and 'dumps' the extra heat. In this scenario the heliostat field would defocus enough heliostats to avoid this situation.

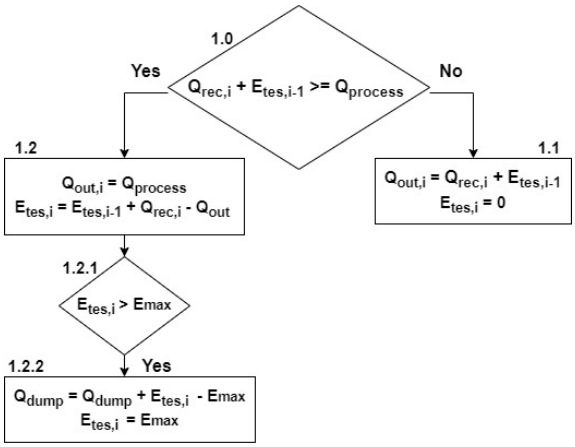

Figure 4.3: Heuristic dispatch strategy.

The strategy described is simple to implement and intuitive to understand. However this is likely a suboptimal strategy, as without extensive storage capacity it is likely to deplete the TES through the late afternoon and night. The backup electrical heaters would then be required to meet the demand in the early morning of the next day before new solar power is available. This is when the electrical tariff is at its first peak for the day, resulting in a higher cost of purchased backup power.

4.3 Dispatch optimisation

In Figure 4.4 an example of available receiver thermal power and the time-of-use electric tariff are shown over the same time period. It can be seen that the availability of solar-derived thermal power and the peak electric tariff do not overlap. Therefore a CST plant without TES would frequently need to purchase backup electrical heat at the highest tariff. The addition of TES allows a number of benefits. When the energy available during peak sun hours exceeds the demand the excess can be stored rather than curtailed. Critically, the TES also allows the plant operator to decouple the use of solar-derived heat from the solar resource availability, allowing the operator to shift solar-derived heat use to higher value periods.

The best TES dispatch profile is determined through an optimisation problem. The goal of the optimisation is to utilise the TES to shift lower-cost solar derived heat to periods of high electrical tariff, thereby minimizing the cost of backup electrical heat. As the cost of solar derived heat is determined mainly by the solar plant's CAPEX, the cost of the solar derived heat is constant over the plant's lifetime. By minimizing the cost of electrical heat, the combined solar-electric heat cost is minimized.

The dispatch optimisation requires a solar plant design, a heliostat field layout, size of TES and the heat requirement of the process. With these plant parameters set the dispatch optimisation can determine the dispatch profile which minimizes the cost of electrical backup heat, thereby minimizing the cost of combined solar-electric heat. The optical

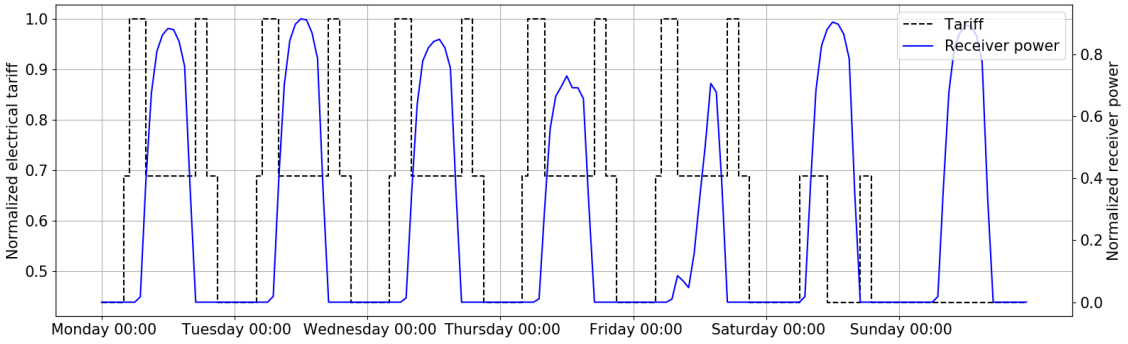

Figure 4.4: Receiver thermal power availability vs electric tariff shown for a sample week.

model provides the thermal power available from the receiver for each time-step of the year. From this the dispatch optimisation determines how the solar energy is best used.

4.3.1 Optimisation formulation

This sections provides the formulation of the dispatch optimisation problem. Figure 3.1 shows the CST plant layout with the associated variables for the dispatch optimisation problem.

The objective of the dispatch optimisation is to minimize the total cost of electrical backup heat for the year. The objective function is formulated as the summation of the required electrical heat multiplied by the tariff, for each time-step of the year:

$$min \left\{ \sum_{i=1}^{8760} (\dot{Q}_{out} - \dot{x}_i) C_i \right\} \tag{18}$$

where $\dot{Q}_{out}$ is the heat required by the process, $\dot{x}_i$ is the design variable (TES discharge) and C_i the electrical tariff for the relevant time-step. The terms in parenthesis represents the electrical heat required at each time-step (this is Equation 12 rearranged) however the symbol for discharge from storage has been changed from $\dot{Q}_{tes_i}$ to $\dot{x}_i$ to adhere with the convention of the symbol used for design optimisation variables.

The objective is subject to two constraints which enforce the energy balances for the system:

$$E_{tes_i} - \dot{x}_i \Delta t \geq 0 \tag{19}$$

$$\dot{Q}_{out} - \dot{x}_i \Delta t \geq 0 \tag{20}$$

where E_{tes_i} is the amount of energy in storage at a given time-step. Equation 19 ensures the system cannot discharge more heat than is available in storage. Equation 20 ensures the system does not discharge more heat than required by the process.

The energy in storage for each time-step is determined from the TES energy balance of Equation 11, presented in section 3.2.

4.3.2 Optimisation algorithms

A number of algorithms were tested on the optimisation problem. SciPy's Optimise function (Oliphant, 2007) and Vanderplaats Research and Development's DOT software (Vanderplaats Research and Development, n.d.) were tested. Both optimisation packages contain multiple algorithms. SciPy is a free open source Python module for scientific computing. DOT is a commercial optimisation software.

SciPy's Optimise function contains the trust-constr and Sequential Least SQuares Programming (SLSQP) methods for constrained non-linear minimization. DOT contains the Modified Method of Feasible Directions (MMFD), Sequential Linear Programming (SLP) and Sequential Quadratic Programming (SQP) methods for constrained non-linear minimization. These fives algorithms were tested on the optimisation problem, to determine the most suitable one.

Appendix E describes the general approach of gradient based optimisation and provides further detail on the most used optimisers; SLSQP and MMFD.

The various algorithms were implemented on a test scenario, for a 3 000 hour problem which represents 3 000 design variables. It proved infeasible to solve the full 8 760 hour problem (full year with hourly resolution) with any of the algorithms in a reasonable amount of time. For each algorithm the resulting cost of electrical heat (objective function value) and total execution time are reported in Table 4.1. The electric cost is normalized with the heuristic strategy's value. This was done as the results have little meaning by themselves, the value is in the relative performance between the algorithms. Only two algorithms successfully improved on the result of the heuristic strategy, DOT's SLP and Scipy's SLSQP. Between SLP and SLSQP, the latter returned slightly better results for less computational time. It is noted that the trust-constr algorithm performed exceptionally poorly. However the algorithm reached its maximum allowed iterations before convergence and so the reported result may be viewed as incomplete.

Table 4.1: Performance of various optimisers on a 3 000 hour problem.

Optimiser	Source	Execution time	Normalized electrical heat cost
MMFD	DOT	1 620 s	1.095
SLP	DOT	16 324 s	0.840
SQP	DOT	677 s	1.293
trust-constr	Scipy	37 111 s	1.699
SLSQP	Scipy	7 756 s	0.836
Heuristic	-	-	1

4.3.3 Rolling time-horizon optimisation

The dispatch profile must be determined for a full year, with an hourly resolution this leads to a 8 760 design variable problem. The execution time results from Table 4.1 show that this problem is too large to solve in a suitable amount of time. The dispatch optimisation will be called by the field design optimiser (developed in later chapters) for each function evaluation. For this reason the computational expense must be significantly reduced.

To reduce computational expense the large optimisation problem is broken into smaller

sub-problems. Instead of optimising over a single 8 760 hour time-horizon, many shorter time-horizon problems are solved instead. The solution to the full problem is then the combination of solutions to the sub-problems. Boundary information is passed on from one sub-problem to the next to ensure a continuous solution.

The 365 days or 8 760 hours are optimised by stepping through the year with discrete steps, one day at a time, and optimising for each day individually. This approach is called a rolling time-horizon optimisation. This method has been used to develop optimised TES discharge profiles for CSP plants by Madaeni et al. (2012b), Wittmann et al. (2008), and Wagner (2015).

The rolling time-horizon optimisation problem leads to a slightly different formulation of the objective function:

$$min \left\{ \sum_{i=N\times 24}^{N\times 24+\tau} (\dot{Q}_{out} - \dot{x}_i) C_i \right\} \forall\ N = 1, ..., 365, \tag{21}$$

where N represents each day of the year numerically and τ is the optimisation time horizon in hours. The day number is multiplied by 24 to convert to hours of the year. The boundary information connecting each day's optimisation is the level of storage at the end of the previous day.

4.3.4 Optimisation time-horizon length

A problem arises through the implementation of a rolling time-horizon. If each day's dispatch profile is optimised independently of the next, a suboptimal solution is found. This is because the least cost electrical heat for a day is to use as much solar heat as possible. This depletes the TES through the evening resulting in a shortfall in the early morning of the next day when the electrical tariff is at its first peak. An example TES discharge profile is shown in Figure 4.5, this profile has been developed using the rolling time horizon approach, where each day is optimised over only a 24 hour period. This figure contain two sub-figures, the first shows the TES level and available receiver thermal power. The second shows the electric tariff, the TES discharge and the electrical heat used. All figures are shown over the same time frame. Notice that the TES is depleted through the night and electrical heat is required to meet the demand during the tariff's early morning peak.

An optimal discharge profile would hold back the low cost solar heat overnight, rather use the low tariff electric heat through the night and then meet the early morning tariff peak by discharging from the TES. A simple solution to achieve this, whilst using a rolling time-horizon approach, is to optimise each day with an extended time-horizon. For example, optimise a Thursday by optimising for 48 hours, Thursday and Friday. Then only keep the results for the first 24 hours. This method provides the optimiser with future knowledge of available solar resource and the electric tariff. This approach ensures the optimiser holds back lower cost solar heat overnight to meet the demand in the early morning when the electrical tariff is at peak rate.

Figure 4.6 shows the rolling time horizon implementation with an extended time horizon of 48 hours. It can be seen that the TES level remains steady throughout the night. Low cost electrical heat is used to meet the demand during these times. The TES then

discharges in the early morning to meet the demand during the electrical tariff peak. This leads to a minimized cost of provided heat.

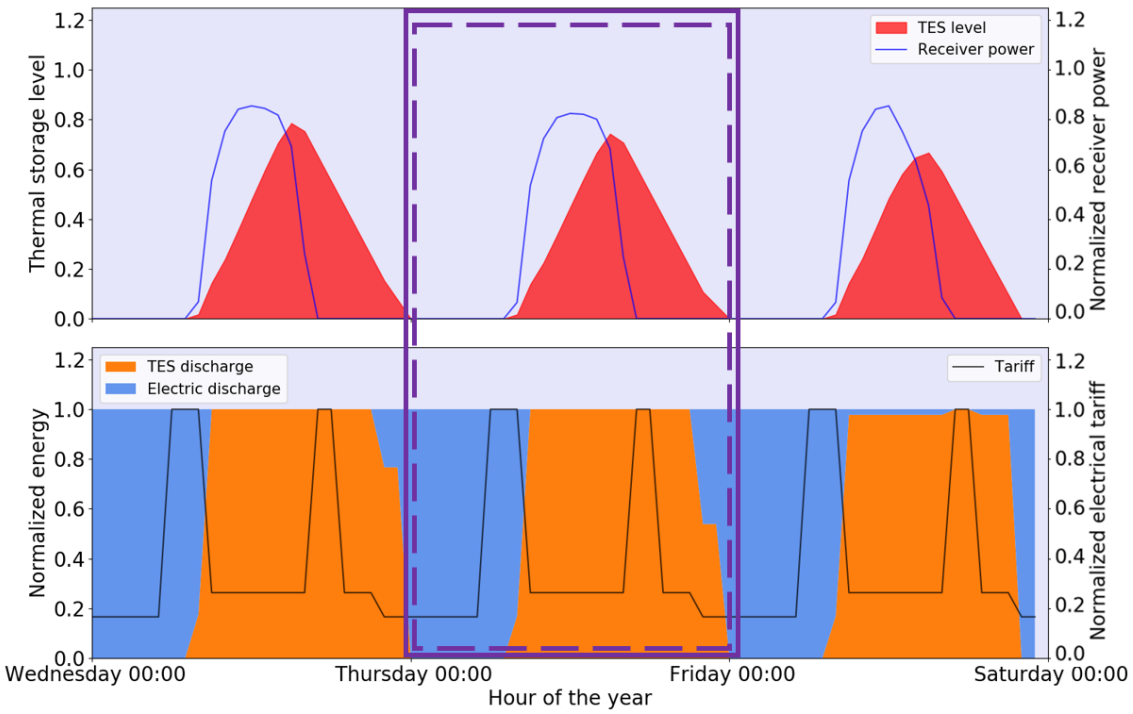

Figure 4.5: Optimal dispatch profile for Thursday (dashed purple block) using a 24 hr time-horizon (solid purple block).

4.3.5 Optimisers comparison on rolling time-horizon

Previously a variety of optimisers were tested on the single time horizon optimisation problem. It was shown that some algorithms outperformed others, however this does not necessarily indicate which algorithms will perform best on the rolling time-horizon approach. The dimensionality difference may affect the algorithm's performance. For this reason all algorithms were tested again on this new approach.

Each algorithm was tested by determining the dispatch profile for a full year, using the rolling time-horizon approach. The initial values for this scenario are random. The results are summarised in Table 4.2. Again the results are normalized with the heuristic strategy's value. From the table it can be seen that the SLP and SLSQP optimisers perform best in terms of objective function, but SLSQP is considerably faster. MMFD performs slightly worse in terms of objective function compared to both, but comparable to SLSQP in terms of execution time. As the dispatch optimisation will form part of the function evaluation for the field layout optimisation, it is important to consider computational expense.

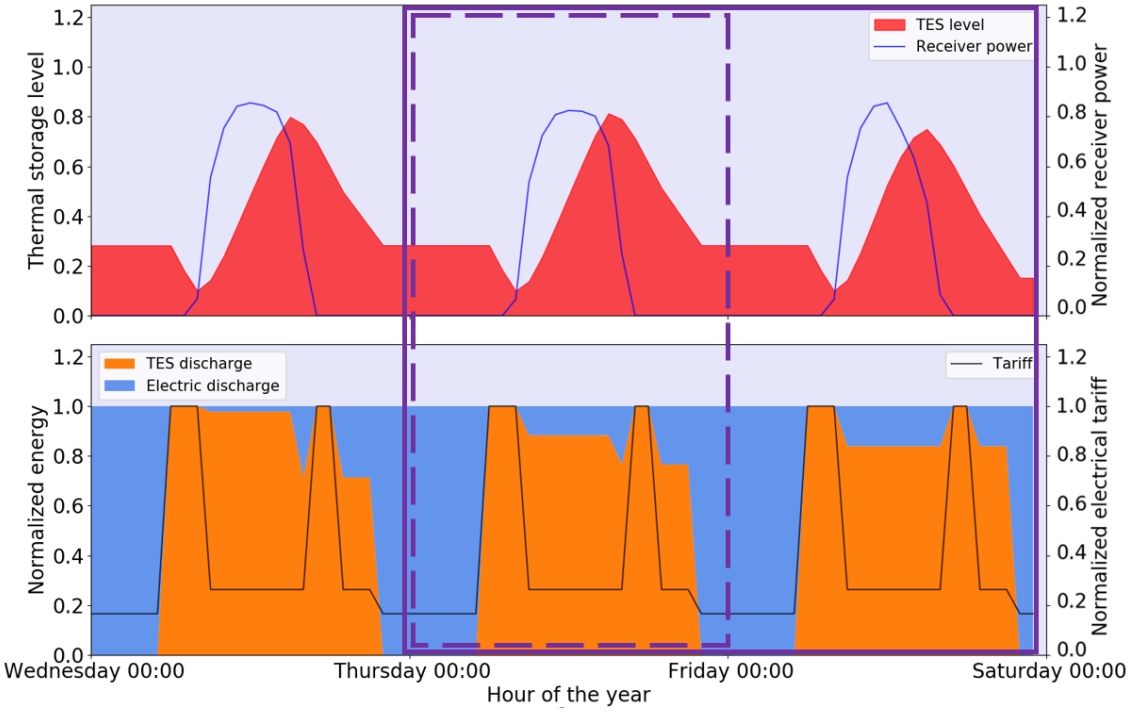

Figure 4.6: Optimal dispatch profile for Thursday (dashed purple block) using a 48 hr time-horizon (solid purple block).

Table 4.2: Performance of various optimisers on a 72 hour rolling time-horizon problem.

Optimiser	Source	Execution time	Normalized electrical heat cost
MMFD	DOT	39.07 s	0.679
SLP	DOT	114.7 s	0.640
SQP	DOT	71.17 s	0.716
trust-constr	Scipy	660.2 s	0.788
SLSQP	Scipy	32.55 s	0.641
Heuristic	-	-	1

An interesting phenomena occurs when comparing the results obtained by the various optimisers. There is a significant difference in terms of the shape of the final discharge profile. In Figure 4.7 the dispatch profiles for the SLSQP and MMFD optimisers are shown over the same time period. Nothing is different besides the selected optimiser. It can be seen that when the electric tariff is low and constant there is a significant difference between the resulting profile for the two optimisers. This is especially noticeable from Saturday evening through early Monday morning, which represents the longest period of low off-peak electric tariff from the Megaflex tariff. The results shown represent only a small portion of the year, but this pattern was repeated throughout the year.

The fluctuation in SLSQP's resulting discharge profile is undesirable as it would lead to unrealistic operation of the electric backup heaters. The significant and rapid fluctuation of TES discharge would require rapid cycling of the electric heaters.

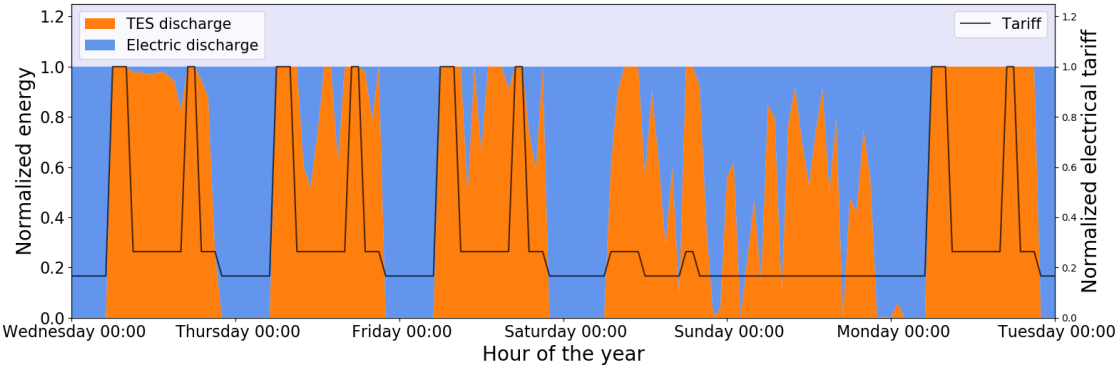

(a) SLSQP results.

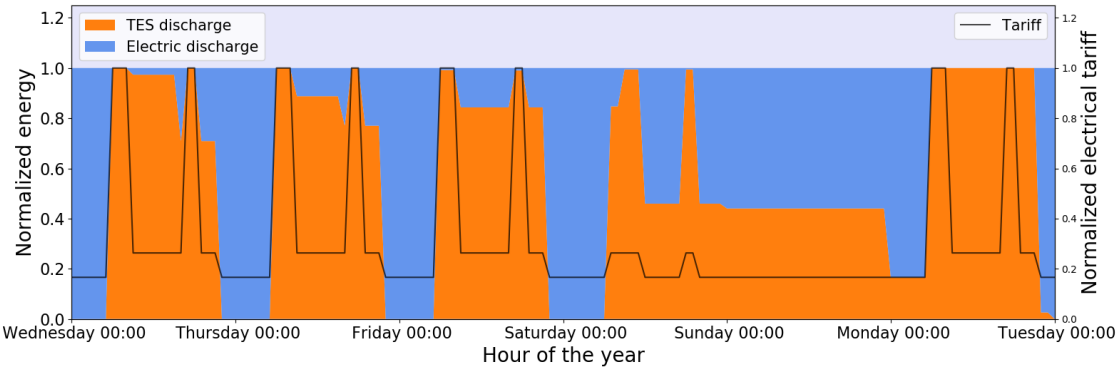

(b) MMFD results.

Figure 4.7: Comparing the optimised TES discharge profile of SLSQP and MMFD for the same initial values (randomised).

This phenomena shows that execution time and objective function value are not the only important indicators for selecting the optimiser. As the dispatch optimiser will be applied to many different problems, various plant configurations, a robust solution is required.

4.3.6 Effect of initial values

In this section different initial values are investigated for the dispatch optimisation problem. The primary reason for investigating the initial values are due to the use of gradient based optimisers. As these algorithms can yield varying optimal results based on the starting position, and without knowledge of the shape of the multi-dimensional design space, trying to find a global optimum requires multiple initial starting positions to be considered.

A number of different initial guesses were tested: all zeros, heuristic values and random scaling. The heuristic value guesses take the discharge profile from the heuristic strategy as the starting values. The random scaling sets the starting values equal to a random number between the upper and lower bound of the allowed discharge amount.

From the performance summarised in Table 4.2, SLSQP and MMFD are selected for further investigation, as they provide good results for the least computational effort. However

for the same starting values (random) they returned dispatch profiles that differed significantly around the low tariff periods.

The resulting SLSQP dispatch profiles with the starting values indicated, for the various starting positions is shown in Figures 4.8 to 4.10. Observing the low tariff periods, specifically Saturday evening to Monday early morning, shows that the optimizer does not move far away from the starting values during these periods. Therefore the undesirable fluctuations seen are possibly a result of the starting values for these time periods.

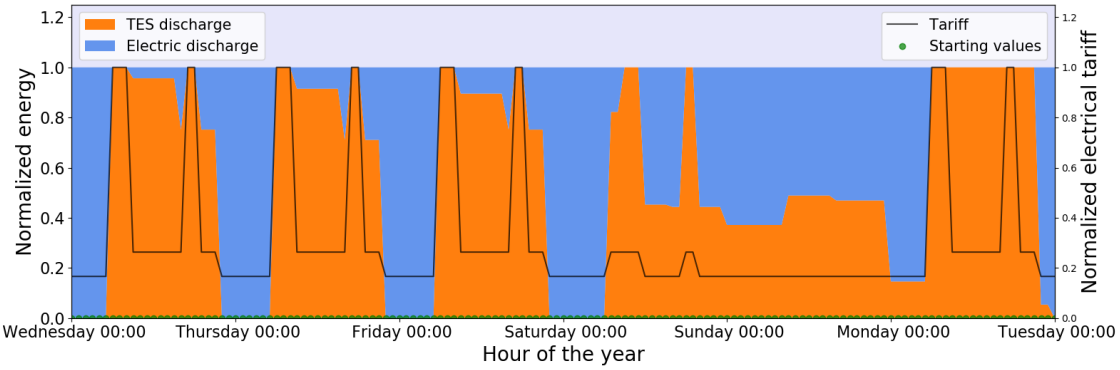

Figure 4.8: SLSQP with initial values set to zero (optimised each day shown with a rolling time-horizon of 72 hr).

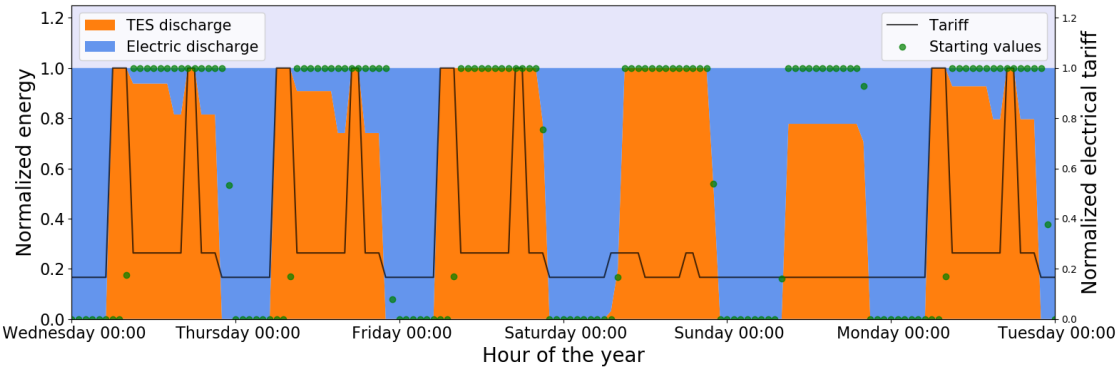

Figure 4.9: SLSQP with initial values set to the heuristic strategy's results (optimised each day shown with a rolling time-horizon of 72 hr).

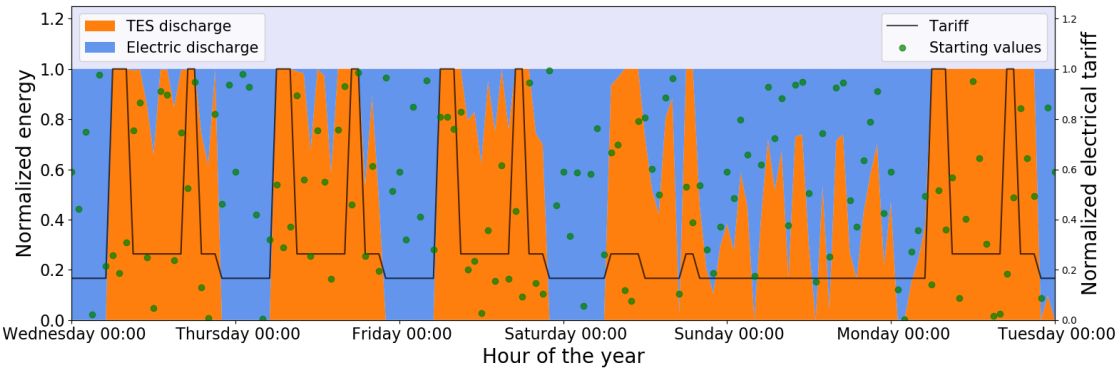

Figure 4.10: SLSQP with initial values set to randoms between the upper and lower bounds (optimised each day shown with a rolling time-horizon of 72 hr).

A dispatch profile is developed by using a set of initial values which follow a sinusoidal pattern. This is chosen as it represents a clear geometric pattern that represents the availability of the solar resource. Figure 4.11 shows the results for SLSQP with the sinusoidal initial values. It is clear from this figure that for the extended low tariff periods, the SLSQP optimiser follows the shape of the initial guesses. A possible explanation is that these low tariff periods are regions of low gradients, and therefore the optimiser does not search these variables extensively as there is little to be gained. Therefore for the low tariff periods many different profile shapes would yield similar objective function results. The low gradients are a result of the tariff being significantly lower than the high tariff periods. Conversely for the high tariff periods the optimiser returns the same result for all different starting values as these are regions with steeper gradients.

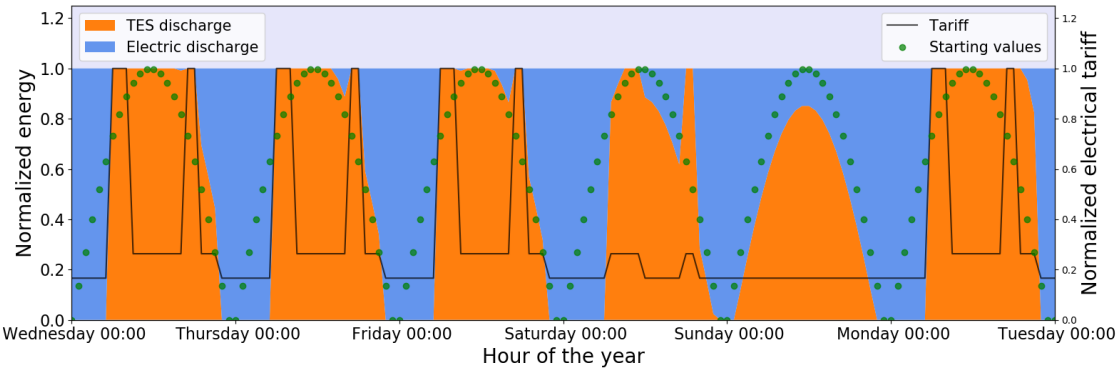

Figure 4.11: SLSQP with initial values set to a sinusoidal pattern (optimised each day shown with a rolling time-horizon of 72 hr).

The same investigation was performed for the MMFD optimiser. This optimiser returned the same discharge profile for all initial values. This indicates that MMFD searches the low gradient regions in a more robust manner than SLSQP. Interestingly, however, as was seen in Table 4.2, SLSQP outperforms MMFD in terms of the objective function value at the optimum. An investigation of why SLSQP outperforms MMFD is given in Appendix A.1.

4.3.7 Rolling time-horizon optimisation implementation

In the previous section it was shown that SLSQP returned a very good optimal solution with the lowest execution time. However the shape of the resulting dispatch profile was strongly influenced by the starting values for periods of low tariff. In some scenarios this lead to an unrealistic dispatch profile requiring rapid cycling of the electric heaters. MMFD delivered the same dispatch profile irrespective of starting value. The dispatch profile shape was also more realistic, with smoother transitions between TES and electric heat discharge values. However MMFD's optimal result was 6 % worse than SLSQP.

The final implementation of the dispatch optimisation was to combine the two optimisers. MMFD is first applied to robustly search through the design space. Next SLSQP is then applied to fine tune the optimum point, using the corresponding MMFD result as the starting values. This provides a refined search resulting in a better final result and a dispatch profile that is realistic.

An alternative approach was investigated to achieve a desirable dispatch profile where a penalty term was added to the objective function. The penalty value increases as the total sum of gradients over the dispatch profile increases. This approach causes smoother profiles to have lower objective function values. As SLSQP yielded the best optimum and execution time for the test scenario, the penalty method was implemented with this as the optimiser. This approach is compared to the MMFD + SLSQP approach, these results are shown in Table 4.3. The two approaches are compared in terms of execution time, objective function result and the sum of gradients of the resulting dispatch profile (used as a surrogate for 'smoothness'). From Table 4.3 it is seen that the double optimiser method yields a lower objective function result, in half the time, while still maintaining a desirable profile shape. For this reason it was chosen as the dispatch optimisation method.

Table 4.3: Comparison of final dispatch optimisation implementation.

Optimiser	Execution time	Electrical heat cost	Sum of gradients
MMFD + SLSQP	45 s	0.642	121.4
SLSQP + penalty	93 s	0.656	120.6
Heuristic	-	1	-

A more detailed discussion of the penalty method implementation can be found in Appendix A.2.

Figure 4.12 shows the results for MMFD and SLSQP when used together. This is how the dispatch optimisation is implemented for the rest of this thesis. It can be seen that SLSQP with MMFD's starting values results in a realistic discharge profile, without any unrealistic discharge cycling. From the first subfigure it can be seen that the dispatch optimisation successfully stores solar energy overnight for use during early morning peak tariff periods. The TES discharge is successfully optimised to ensure peak tariff period's full thermal demand is frequently met with solar energy rather than electric. This can be seen in the second subfigure by looking at the peak tariff periods and the TES discharge.

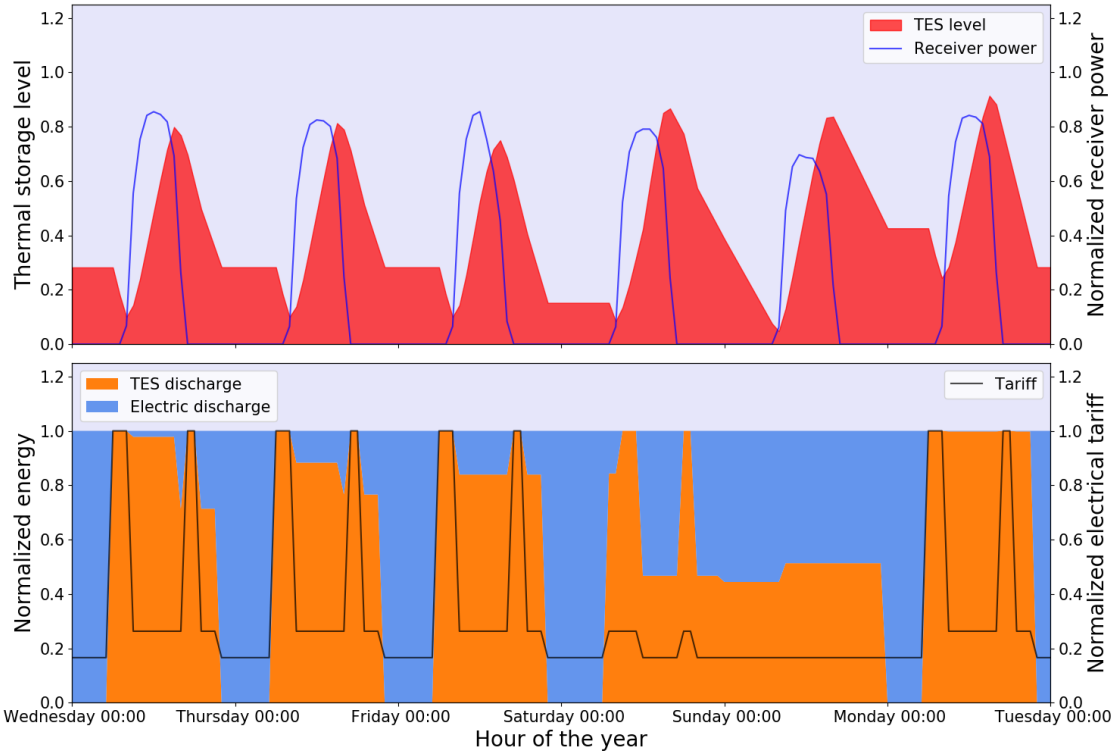

Figure 4.12: MMFD and SLSQP used together.

4.3.8 Time-horizon length parametric study

The rolling time-horizon approach requires a time-horizon of sufficient duration to ensure an optimal dispatch profile is found. There is a trade off between computational expense (a longer time horizon represents an optimisation problem with more design variables) and including sufficient future knowledge of the electrical tariff and the solar resource. Additionally as this approach assumes perfect foresight, a judgement must be made on the length of time for which solar resource data can be accurately predicted.

To investigate the effect of the time horizon length a parametric study was performed. For a test scenario the dispatch profile for the entire year was optimised using the rolling time-horizon approach. This was completed a number of times for different time horizon lengths. Figure 4.13 shows the annual cost of electrical heat against the time horizon length. Also shown is the computational expense of each annual optimisation. The cost of electrical heat is normalized by the highest value as the relative difference is of interest. From the figure it can be seen that the longer time horizons lead to lower costs of electric heat. The result converges at approximately 100 hours. However a majority of the asymptote value is achieved around 50 hours. The computational expense increases exponentially for long time horizons. For the remainder of this thesis where the dispatch optimisation is used a time-horizon of 48 hours will be used. This is selected as it provides a good amount of foresight to optimise the dispatch profile without being unrealistic in terms of predicting the weather forecast for a real plant. This is the same time-horizon used by Wagner (2015).

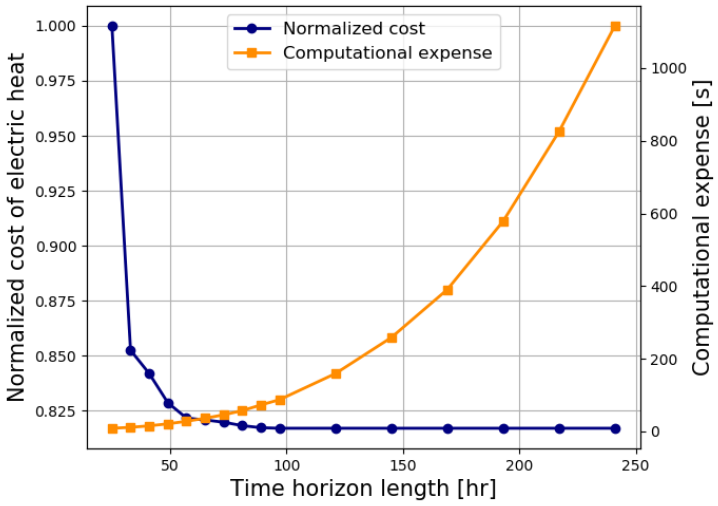

Figure 4.13: Time horizon length parametric study.

4.4 Dispatch optimisation performance

It was shown in the previous section that the dispatch optimisation significantly outperforms the heuristic strategy. In this section the difference is investigated. This also serves to show the dispatch optimisation behaves as desired, resulting in the improved performance. The figures presented in this section are inspired by those of Wagner (2015).

Figure 4.14 shows the weekday variation of the TES level, against the electric tariff. Each blue line represents a separate weekday of the year. Figure 4.14a shows how the heuristic strategy charges through the day when solar energy is available, and then discharges throughout the evening. This means the heuristic strategy can never meet the early morning demand with low cost solar energy and therefore must purchase electric heat during this high tariff period. Figure 4.14b shows how the optimal strategy holds back solar energy throughout the evening, to more frequently meet the early morning demand during the high tariff period. This is seen by the steady TES level throughout the night.

Figure 4.15 shows the hourly variation of TES discharge for every weekday of the year. This is shown for the heuristic and optimal strategies. These figures take the annual dispatch profile, break it down into 24 separate datasets, each representing the dispatch profile for the i^{th} hour of a weekday. For each hour's TES discharge dataset a box and whisker plot is shown, this represents the variation of the TES discharge over this weekday hour for the entire year. The whiskers show the range of the data, the box bounds the first and third quartile, the median is shown as a solid orange line and the mean as a black dotted line.

From Figure 4.15a it can be seen that around midday the boxes are very small, indicating the variation is low and for these hours the TES discharge is high throughout the year. The mean lines show the discharge is highest at these hours, then decreases throughout the evening. The early morning tariff peak hours have high variation, indicated by the large boxes, and lower mean values. This indicates the heuristic strategy almost never meets the demand during these periods with lower cost solar-derived heat.

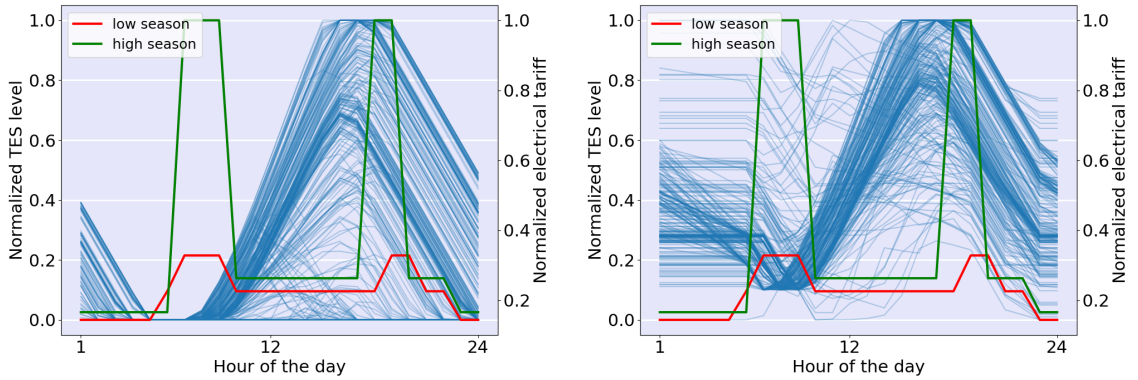

(a) Heuristic strategy.

(b) Optimal strategy.

Figure 4.14: Comparing variation in weekday TES level between heuristic dispatch strategy and optimal dispatch profile. TES dispatch shown in blue, electric tariff in green and red.

From Figure 4.15b it can be seen that the boxes are very small over the peak tariff periods. This means the TES discharge variation for these hours is low. Additionally the mean is near the full load discharge value. This means the optimal strategy frequently meets the full load during the high tariff periods with low cost solar-derived heat. Furthermore the discharge around midday has more variation for the optimal strategy than the heuristic. This is where the optimal strategy charges and stores energy to meet future high tariff period demands.

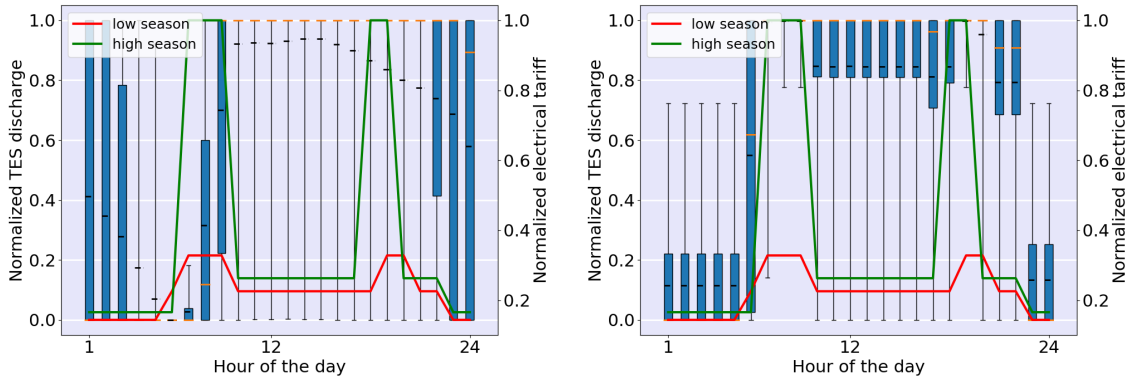

(a) Heuristic strategy.

(b) Optimal strategy.

Figure 4.15: Comparing variation in weekday TES level between heuristic dispatch strategy and optimal dispatch profile. TES dispatch shown in blue, electric tariff in green and red.

From Figure 4.15b a small deviation from the low variation discharge over peak tariff hours can be seen for the first peak tariff hour of the high season curve for the evening peak. Here the box is not as small as other peak tariff hours. This is simply because the peak tariff hours shift an hour forward in the day between the low and high demand season. There are only three high demand months in the year, the rest are low demand.

Therefore this box is influenced by the fact that this hour is a lower tariff period during the low demand season.

Figures 4.14 and 4.15 show where the developed optimal dispatch profile outperforms the heuristic strategy. In Table 4.3 the results showed that for the test scenario the rolling time horizon optimisation outperforms the heuristic strategy by nearly 40 % in terms of cost of bought electrical heat. These results show a good TES dispatch profile has been developed, which outperforms the heuristic strategy.

5 HelioPod™ field layout optimisation

The HelioPod™ technology has to date only been implemented as part of the Helio100 pilot plant project (Kotzé et al., 2016). This field contains 120 heliostats. For this small field a simple pod layout, shown in Figure 2.24a proved sufficient. In a field layout optimisation investigation Domínguez-Bravo et al. (2016) showed for this size HelioPod™ field an optimised field did not perform significantly better than the simple arrangement. Lubkoll et al. (2018) investigated the HelioPod™ technology as a component to provide process heat to a Manganese sinter plant. This work required a significantly larger field, with 2 220 heliostats. Lubkoll et al. (2018) applied a heuristic approach for the field design. In this design consecutive rows of tessellated HelioPods™ were placed within a bounding circle, this field is shown in Figure 2.26. This is the only investigation into pod field designs known to the author. For this reason an investigation into the design of larger HelioPod™ fields was undertaken.

It has been shown by Lutchman et al. (2014) that free-variable optimised heliostat fields do not perform significantly better that pattern-based approaches. Furthermore free-variable optimisation is extremely computationally expensive due to high dimensionality. For these reasons a pattern-based field design approach was followed in this study. Here the pattern parameters that define the field layout were optimised rather than each individual HelioPod's™ position. This approach leads to a dimensionality reduction of the optimisation problem and thereby computational expense.

Literature on pattern-based heliostat field layouts are aimed at fields of individual heliostats (free-form field), not pods. For this reason new patterns-based algorithms are developed to design the HelioPod™ fields. This process starts by using the heliostat field design tool SolarPilot to investigate resulting optimised free-form field layouts when changing a number of different parameters. The effect of tower height, receiver tilt and the distance of the tower relative to the field were investigated. For each parameter value investigated, SolarPilot designed an optimised radial stagger field. This was only possible for free-form fields but the understanding of the effect of these parameters on the resulting field designs guided the development of the HelioPod™ field layout algorithm. This algorithm parametrizes the pod field layout and uses an optimisation routine to design an optimal layout. This mimics the philosophy of pattern-based heliostat field layout optimisation.

5.1 SolarPilot free-form field designs

In this section SolarPilot was used to design optimised free-form heliostat fields using pattern-based methods. A number of plant design parameters were investigated to determine their significance on the field optical performance. The important parameters were then investigated further during the HelioPod™ field designs. Less import parameters were fixed for the HelioPod™ field designs. The goal of this section was to determine important parameters and the shape of optimal fields. These insights were then used to develop the HelioPod™ field layout algorithm.

SolarPilot allows three different pattern-based field layouts; cornfield, traditional radial stagger and dense radial stagger. Mutuberria et al. (2015) showed that a dense radial staggered field layout performed well against other field designs for a variety of field sizes.

Therefore this field layout was used. The dense radial stagger layout determines a radius around the tower at which heliostats track sufficiently 'flat' such that blocking and shading effects are minimal. Within this radius the heliostats are densely packed. Outside this radius the traditional radial stagger layout is implemented to reduce blocking and shading. The reader is referred to section 2.7.1 for a discussion of the radial stagger layout method.

For the SolarPilot field designs the general plant parameters are shown in Table 5.1. These parameters were inspired by the CentRec© plant design implemented by Lubkoll et al. (2018). This work utilizes a square receiver aperture as SolarPilot cannot simulate a circular plane, such as the one used to model the CentRec© receiver aperture. For each set of plant parameters SolarPilot designs a dense radial stagger field. Each heliostat's focal length was modelled as two times the slant range (distance between the heliostat and receiver centres). This means each heliostat's curvature is idealised for its position relative to the receiver (Dereniak and Dereniak, 2008). For parameters not under investigation the values from Table 5.1 are applicable.

Table 5.1: Reference plant design parameters.

Plant design parameter	Value
Location	Northern Cape
Design load at solar noon on equinox	2.5 MW_{th}
Tower height*	40 m
Receiver tilt angle*	45°
Receiver geometry	Tilted flat plate
Receiver aperture size	1.5 m × 1.5 m
Focal length	2×Slant range

* variable when this parameter is under investigation, fixed to this value when not.

The next few subsections investigate the effect of tower height, receiver orientation and tower distance to field, on the resulting field layout.

5.1.1 Tower height parametric study

The DLR have published numerous papers evaluating a CentRec© based CST plant for process heat generation for different industries (Amsbeck et al., 2015) , (Amsbeck et al., 2014b) and (Amsbeck et al., 2017). The proposed tower height varies across all these publications. For this reason varying tower heights were investigated to determine the effect on the field's performance.

Figure 5.1 shows some of the resulting field layouts for various tower heights generated by SolarPilot. From these figures it can be seen that a taller tower allows for the design of a more compact field without incurring optical penalties. The 15 m tower field's layout is mainly radial stagger, whereas the 90 m tower is completely densely packed. This is due to changes in the tracking angle of the heliostats for different tower heights. For taller towers the heliostat field tracks 'flatter', causing less blocking and shading, therefore a denser field is best. For the 15 m tower it can be seen that the radial stagger layout increases the distance between successive radial rows of heliostats as the row is further from the tower,

this minimizes blocking and shading (see Figure 2.16b). Furthermore Figure 5.1 shows that the denser fields have higher optical efficiencies. This is to be expected as the spillage and attenuation are reduced for denser and smaller fields.

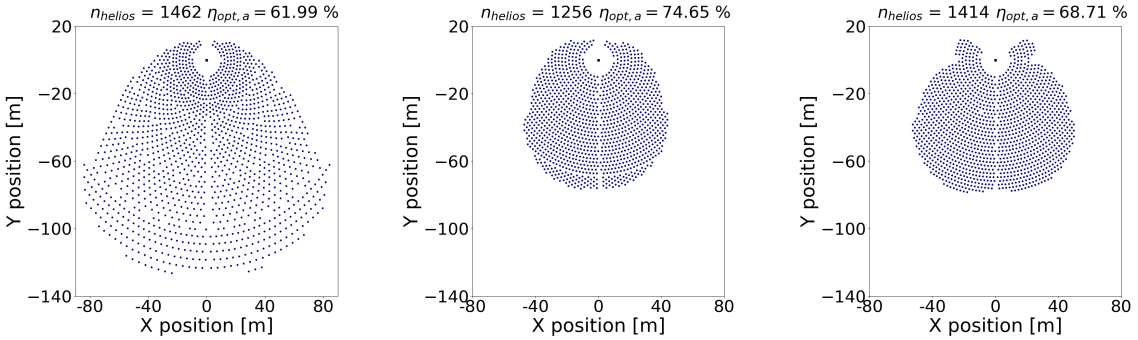

(a) 15 m tower. (b) 45 m tower. (c) 90 m tower.

Figure 5.1: Resulting field designs for various tower heights.

5.1.2 Receiver tilt angle parametric study

The CentRec© receiver tilt angle has also varied across publications on the technology. Amsbeck et al. (2014b) reported a tilt angle of 65°, Lubkoll et al. (2018) modelled 45° and in the development of a FEM heat transfer model for the receiver Wu et al. (2015b) reported the receiver can be tilted between zero and 90° (relative to the horizontal). For these reasons a parametric study of the resulting field for a range of tilt angles was performed.

Figure 5.2 shows the resulting fields for various tilt angles. It can be seen that the closer the tilt angle is to the horizontal (0°) the less densely packed the field becomes. Conversely, for a vertical downward tilt angle (90°), the entire field is densely packed. The field transitions from polar (entire field north or south of the tower) to surround, as the tilt moves from horizontal to vertical. Comparing the two extremes, near horizontal and vertical, the results are fairly similar in terms of optical efficiency. The surround field of the vertical tilt suffers from worsening cosine losses for heliostats north of the tower (see Figure 2.12b), but improved spillage and attenuation as the average heliostat slant range is reduced. For a tilt angle which is near horizontal the field has heliostats at a greater distance from the receiver, therefore the spillage and attenuation losses are greater. However the cosine losses are improved as the field is polar. As the tilt changes some optical losses increases, and some decrease, this seems to balance and provide similar performance irrespective of tilt angle. For these reasons it is concluded that the tilt angle does not affect the optical performance significantly.

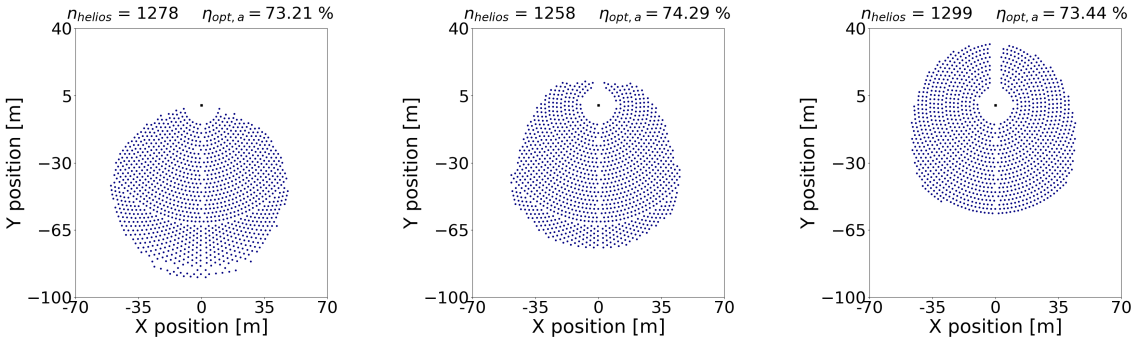

(a) 15° tilt angle. (b) 45° tilt angle. (c) 90° tilt angle.

Figure 5.2: Resulting field designs for various receiver tilt angles.

5.1.3 SolarPilot investigation results

The results for the various parameters that were investigated are summarised in Figure 5.3. These figures shows each parameter's tested values and the resulting field optical efficiency. The distance between the tower and the nearest heliostat was also investigated. Here the tower was simply moved in increments nearer or further from the field along the y axis. As expected, the further away the tower is from the field, the worse the field optical efficiency is. This is because the spillage and attenuation losses increase as the distance to the tower increases.

Comparing the effect of the various parameters, tower height shows the most significant effect on the field optical performance. This parameter will be investigated further for the HelioPod™ fields. The tilt angle and tower position will be fixed to 45° and 0 m, respectively, as the investigation shows these parameters do not effect the results as significantly.

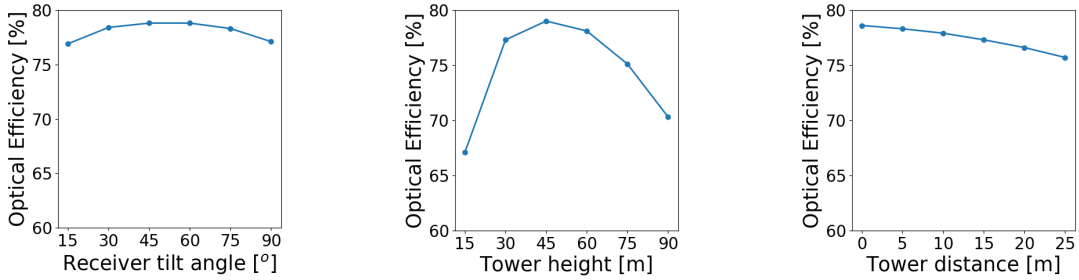

(a) Receiver tilt angle. (b) Tower height. (c) Tower distance.

Figure 5.3: Effect of varying; the tower height, receiver tilt angle and tower position relative to start of the field, on the field optical performance.

5.2 HelioPod™ field layout algorithm

Two HelioPod™ field layout algorithms were developed. One based on radial rows of pods, the other on straight rows of pods (cornfield). From heliostat field layout design optimisation literature it is known that radial rows are better but the practicality of straight rows makes this pattern relevant.

The fields are divided into rows, a row contains inward-facing and outward-facing tessellated HelioPods™ (this increases the density of pods). Each field layout is described by the number of rows, the width of each row and the pod side lengths in each row. From the SolarPilot fields, it was seen that the field's width varied depending on the distance to the tower. For lower tower heights the fields were designed with a radial stagger layout. For taller tower the fields were predominately densely packed. To replicate these features the optimisation parameters for the pod fields are row widths and row pod side lengths. The row width parameter allows the optimisers to vary the field width at any point. The pod side lengths parameters allows the optimisers to increase the distance between successive rows of heliostats. The greater the pod side length, the greater the distance between the heliostats on that pod. As a radial stagger layout increases the distance between rows as the rows are further from the tower, increasing the pod side lengths for pod rows further from the tower could replicate this effect.

The distance between consecutive rows is a function of the pod sizes of the two rows, to ensure no collision. For the cornfield, the placement of adjacent pods is taken from the work of Lubkoll et al. (2018). For the radial field, the placement of adjacent pods ensures a uniform row width while avoiding collision. Figure 5.4a depicts the layout of the cornfield algorithm. L is the pod side length, R is the radius of a circle which passes through each vertex of a single pod, W is the row width and D is the distance separating consecutive rows. Figure 5.4b depicts the layout of the radial algorithm. W_2 is the second row's width in degrees and is measured between the centres of the two pods furthest apart in this row, L_1 and L_2 are the pod side lengths for the respective rows.

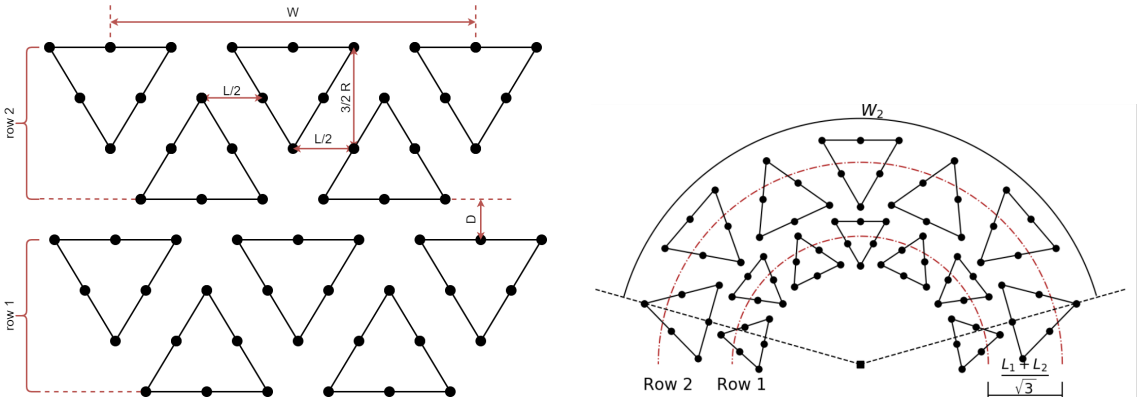

(a) Cornfield layout.

(b) Radial field layout.

Figure 5.4: HelioPod™ layout algorithms.

5.3 Field layout design optimisation

The field layout algorithms parameters are put through an optimisation routine to design a field with high optical performance. The parameters that make up the design variables is the width of each row and the side lengths of pods in each row. For each optimisation routine the number of rows was fixed. By varying the row width the optimiser can replicate the field shapes seen in the SolarPilot layouts, and by varying the pod side length in each row, the optimiser can replicate the benefits of the radial stager pattern by changing the field density.

The objective function for the field layout optimisation is the combined solar-electric levelised cost of heat, $LCOH$, from Equation 17. Utilizing the economic parameter as the objective function leads to larger fields which collect more energy, this provides improved economic performance. The fields are sized to deliver the optimal amount of energy to offset the lifetime costs. For a set amount of TES and output value to the pre-heater, this optimisation will oversize the field and so determine the optimal solar multiple. The decision was inspired by SolarPilot's layout optimisation, which also utilizes an economic parameter as the objective function.

The optimisation problem is defined as:

$$min\ LCOH \tag{22}$$

such that,

$$W_z \geq 0\ \forall\ z = 1, 2, ..., Z \tag{23}$$
$$1 - W_z \geq 0\ \forall\ z = 1, 2, ..., Z \tag{24}$$
$$L_z - 4.6 \geq 0\ \forall\ z = 1, 2, ..., Z \tag{25}$$
$$10 - L_z \geq 0\ \forall\ z = 1, 2, ..., Z \tag{26}$$

where W_z are the design variables associated with row widths, L_z are design variables associated with row pod side lengths, subscript z denotes the relevant row and Z is the number of rows. Equations 23 and 24 constrain the row widths to be non-negative and less than a normalized maximum. The maximum width for the cornfield row is 160 m. The maximum width for the radial row is 180°. Equations 25 and 26 constrain the pod side lengths to a minimum of 4.6 m and a maximum of 10 m. The represents the smallest possible pod for the heliostats used. The upper limit is double this minimum size (rounded up).

The choice of objective function results in a multi-level optimisation problem. For every field design function evaluation the dispatch optimisation routine is called. This process is depicted in the flow diagram of Figure 5.5. The optimisation runs are shown in red. The various models are shown in blue and the boundary information passed between models shown adjacent to the arrows.

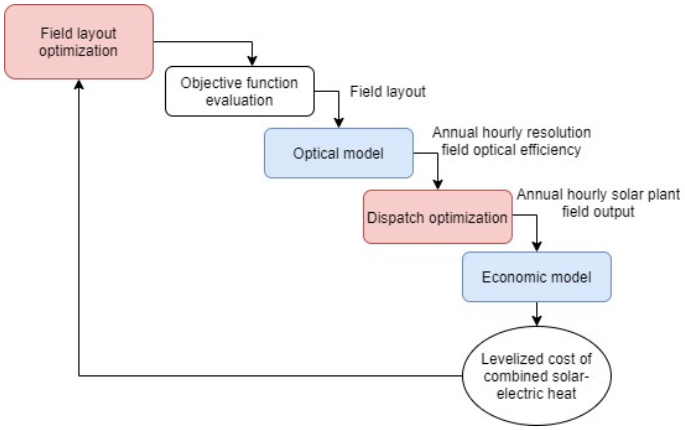

Figure 5.5: Field design optimisation routine.

The optimised field layout is dependent on the thermal requirements of the plant. Therefore the amount of TES available and required thermal output from the plant to the process are set before the field layout optimisation is performed. The field layout optimisation will then design a heliostat field to minimize the objective function for these thermal requirements. For the field layout development and work presented in this chapter a reference plant with 14 hours of TES and an output to the pre-heater of 0.85 MW_{th} is used. These reference plant values are taken from Mckechnie et al. (2020). Once the field layout optimisation tool is developed these plant values will be determined through a parametric study in the next chapter.

The algorithms are tested for a number of different initial values, number of rows and tower heights. Gradient based optimisers are used, therefore to try find a global optimum different initial values are investigated. The initial values tested are a field with no heliostats, a full field, where each row has the maximum width and minimum pod size and finally a random field, where each row's length and pod size are randomized. Several different optimisation algorithms were also tested. The results presented in this chapter use the SLSQP algorithm which performed the best in these tests. The reader can see the comparison of the various optimisation algorithms in Appendix C. Figure 5.6 depicts the full field starting position for both cornfield and radially stacked field layouts.

Two different tower heights were tested as the SolarPilot investigation showed this parameter has a significant influence on the resulting field performance and shape. A shorter tower of 20 m and a taller tower of 40 m were considered. For the two parameters investigated (number of rows and starting position) the results for the taller and the short tower, and both field layout algorithms are shown.

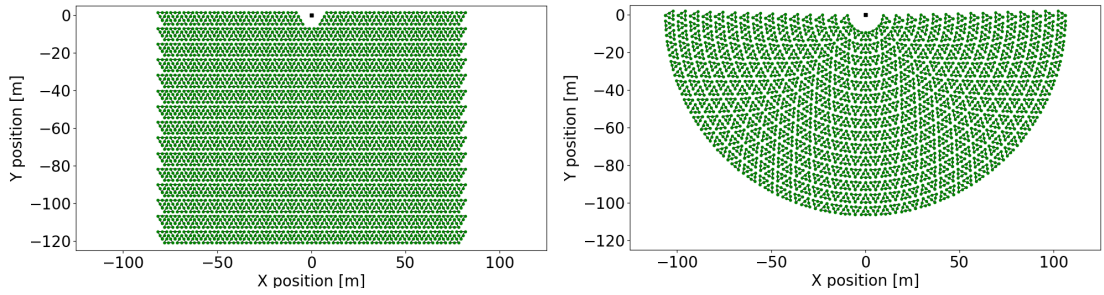

(a) Cornfield layout.

(b) Radial field layout.

Figure 5.6: Full field starting positions.

5.4 Starting value investigation

Due to the use of gradient based optimisers and their sensitivity to starting values for the design variables, a number of different starting values are tested.

The results for the starting values, for both field types, are first presented and discussed for the 20 m tower, then for the 40 m tower, before a brief conclusion on the impact of the starting values.

5.4.1 The 20 m tower results

Table 5.2 summarises the results for the three different starting values and the two different field layouts for the 20 m tower. From these results it can be seen that for the shorter tower the best radial field outperforms the best cornfield. Furthermore, the different starting positions do yield different results. For both field layouts the no heliostats starting values yield the worst result. The random and full field yield similar results for both field types.

Table 5.2: Results for 20 m tower for different starting values.

Layout	Starting values	Optimum # heliostats	$\eta_{opt,a}$	min $LCOH$
Radial	No heliostats	2 130	44.34 %	43.20 \$/MWh$_{th}$
	Random no. heliostats	2 190	47.69 %	41.04 \$/MWh$_{th}$
	Full field	2 274	46.64 %	41.06 \$/MWh$_{th}$
Cornfield	No heliostats	2 136	44.23 %	43.34 \$/MWh$_{th}$
	Random no. heliostats	2 340	44.93 %	41.76 \$/MWh$_{th}$
	Full field	2 280	45.62 %	41.64 \$/MWh$_{th}$

Figures 5.7 and 5.8 show the resulting field layouts for the radial and cornfield layouts, respectively. All fields show a distinct dense region, where the pod side lengths are at their minimum, and then increasing pod side lengths toward the furthest away rows. Comparing the two different field designs, it can be seen that the furthest pods of the radial fields are nearer to the tower than for the cornfield layouts. This would result in reduced spillage and attenuation losses for the radial field relative to the cornfield, as these losses are a function of heliostat distance to the receiver.

When initializing the cornfield with no heliostats (Figure 5.8a), the optimisation algorithm gives a field with significant width reduction toward the rear of the field and most pods are small. When initializing with a full field start (Figure 5.8c) the width remains constant and the pod sizes grow toward the rear of the field. Reducing the field width towards the rear would reduce the number of heliostats with poor spillage and attenuations performance. Even so this field (Figure 5.8a) still performs worse than the full field start (Figure 5.8c). This indicates that at this tower height, monotonically increasing pod sizes toward the rear of the field provides greater reduction in blocking and shading losses than the increase in attenuation and spillage caused by placing heliostats further away from the receiver.

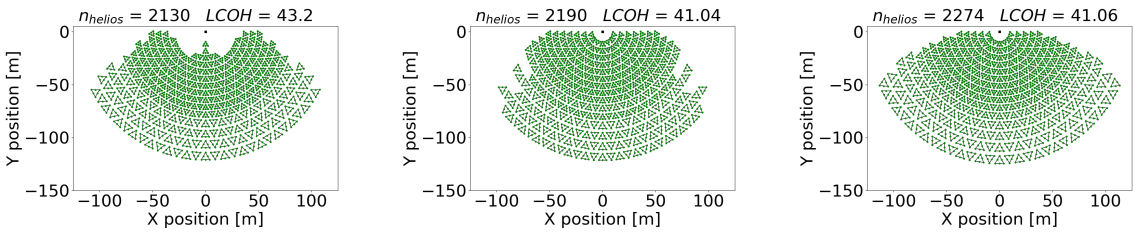

(a) No heliostats start. (b) Random field start. (c) Full field start.

Figure 5.7: Resulting radial field layout for different starting positions with a 20 m tower.

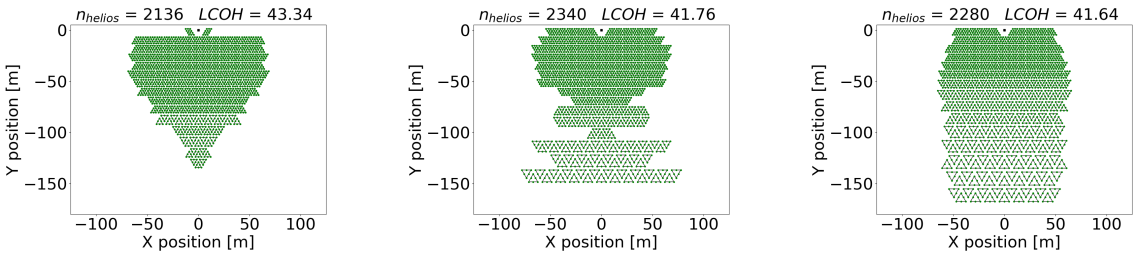

(a) No heliostats start. (b) Random field start. (c) Full field start.

Figure 5.8: Resulting cornfield layout for different starting positions with a 20 m tower.

5.4.2 The 40 m tower results

Table 5.3 summarises the results for the three different starting values and the two different field layouts for the 40 m tower. From these results it can be seen that for the taller tower the cornfield layouts perform slightly better than the radial fields. Again, the different starting positions yield different results for both field types, with the full field start yielding the best results. The 40 m tower fields perform better than the 20 m tower fields, requiring a smaller field with a reduced LCOH.

Table 5.3: Results for 40 m tower for different starting values.

Layout	Starting values	Optimum # heliostats	$\eta_{opt,a}$	min $LCOH$
Radial	No heliostats	2 010	54.62 %	40.01 \$/MWh$_{th}$
	Random no. heliostats	1 914	59.05 %	38.90 \$/MWh$_{th}$
	Full field	1 938	60.16 %	38.57 \$/MWh$_{th}$
Cornfield	No heliostats	1 884	61.35 %	38.42 \$/MWh$_{th}$
	Random no. heliostats	1 956	61.58 %	38.24 \$/MWh$_{th}$
	Full field	1 920	61.60 %	38.29 \$/MWh$_{th}$

Figures 5.9 and 5.10 show the resulting field layouts for the radial and cornfield layouts, respectively. For the radial fields the majority of the field contains pods with the minimum side length, leading to a denser field, compared to the 20 m tower fields. This is the same result seen in the SolarPilot investigation, where the taller tower fields were mostly densely packed, and shorter tower fields mostly radial stagger (see Figure 5.1).

The 40 m tower cornfield layouts are similar in shape to the 20 m tower cornfield layouts, but narrower. Again the cornfield layouts have heliostats significantly further from the tower than the radial fields, this results in a more prominent increasing of pod side lengths to minimize blocking and shading for the heliostats further away. Comparing Figures 5.10a and 5.10c, the resulting field shape is quite different, but the performance is very similar, unlike what was seen for the shorter tower (for the same field type and initial values), where the performance difference was more significant. This, and the fact that the performance is similar for all these 40 m tower fields, indicates that at 40 m the tower is sufficiently tall to provide good line of sight to most heliostats, with little blocking and shading, and therefore the exact field layout has a smaller impact on performance.

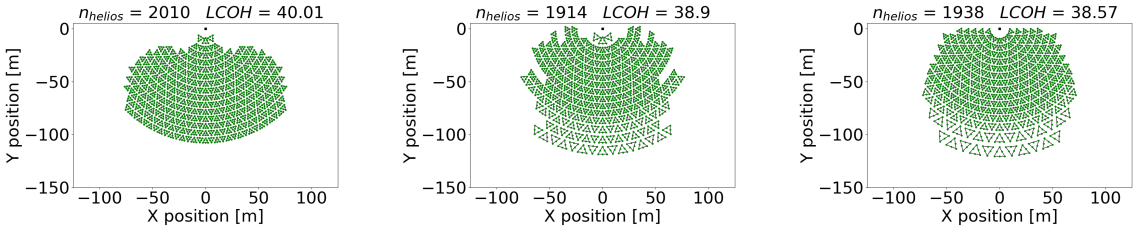

(a) No heliostats start. (b) Random field start. (c) Full field start.

Figure 5.9: Resulting radial field layout for different starting positions with a 40 m tower.

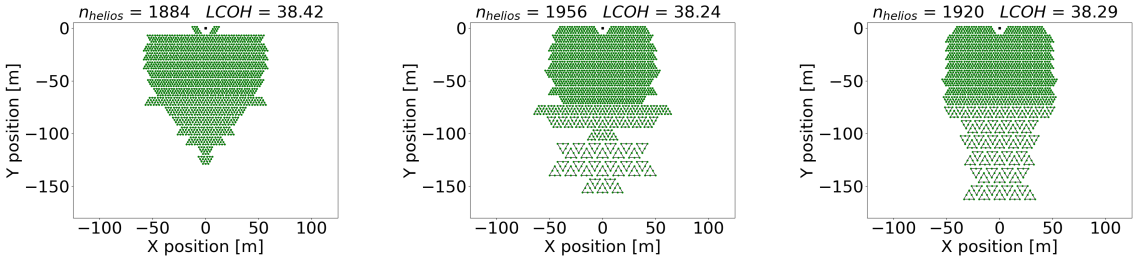

(a) No heliostats start. (b) Random field start. (c) Full field start.

Figure 5.10: Resulting cornfield layout for different starting positions with a 40 m tower.

5.4.3 Conclusion on the starting value investigation

The different starting values have a significant influence on the resulting field layout, its optical performance and resulting $LCOH$. In all cases the no heliostats start resulted in the worst performing fields. The full field start performed best or near-best for both radial and cornfield layouts. Furthermore, this starting value results in fields with a monotonic increase of pod side length across the rows, just as the optimised free-form radial stagger layout increases the distance between successive rows monotonically as the row is further from the tower. The fields for the shorter tower require more heliostats than fields for the taller tower. The results indicate that for a 40 m tower a good field layout requires the heliostats to be densely packed. The 20 m tower requires a more sophisticated field design due to the field being more spread out.

In Appendix C.3. a line search through the multi-dimensional design space is shown from the no heliostats and full field initial values to the returned optimum, for each starting value. This illustrates that the no heliostats start begins far from the optimum, whereas the full field begins near to the optimum. This is another reason the full field start is preferred.

5.5 Number-of-rows investigation

The field design optimisation problem is set up to determine the optimal design given a maximum allowed number of rows. This section investigates the impact on the field performance for various maximum allowed rows: 10, 15 and 20 rows. From the previous

section it was seen that the full field start resulted in the best or near best performing fields. For this reason all fields presented in this section utilize this initial value.

The results for the initial positions, for both field types, are first presented and discussed for the 20 m tower, then for the 40 m tower, before a brief conclusion on the effect of the maximum allowed number of rows.

5.5.1 The 20 m tower results

Table 5.4 summarises the results for the three different sized fields and the two different field types for the 20 m tower. The radial fields again outperform the cornfield layouts for this tower height. The results for the radial fields vary significantly for the smallest field relative to the two larger fields. The difference in performance is less for the cornfield layouts, across the different size fields. For both field types the number of heliostats increases with the number of rows. The 15 row fields perform best for both field types.

Table 5.4: Results for a 20 m tower given the maximum number of rows.

Layout	Starting values	Optimum # heliostats	$\eta_{opt,a}$	min $LCOH$
Radial	10	1 440	53.05 %	45.71 \$/MWh$_{th}$
	15	2 274	46.64 %	41.06 \$/MWh$_{th}$
	20	2 400	45.61 %	41.12 \$/MWh$_{th}$
Cornfield	10	2 070	47.51 %	41.94 \$/MWh$_{th}$
	15	2 280	45.62 %	41.64 \$/MWh$_{th}$
	20	2 622	41.43 %	42.52 \$/MWh$_{th}$

Figures 5.11 and 5.12 show the resulting field layouts for the radial and cornfield layouts, respectively. For both radial and cornfield layouts, as the number of rows increases, so does the size of the field (in terms of number of heliostats). All fields except the 10 row radial field, show a monotonically increasing pod size toward the rear of the field. The 10 row radial field is completely dense, with all pod sizes at the minimum. This means for the allowed rows it has the maximum number of heliostats possible, which is significantly fewer than the 15 and 20 row fields. The poor performance of the 10 row fields indicate the CAPEX reduction due to less heliostats has a smaller effect on the $LCOH$ than the reduction in collected energy due to the smaller field size.

The larger radial and cornfield layouts show distinct dense regions and then monotonically increasing pod sizes for rows further from the tower, similar to the short tower results seen in the starting value investigation and the SolarPilot free-form investigation in section 5.1.1. The 15 row fields yield the best results for both field types. This indicates that the 20 row fields are too large, with too many heliostats in poorer positions.

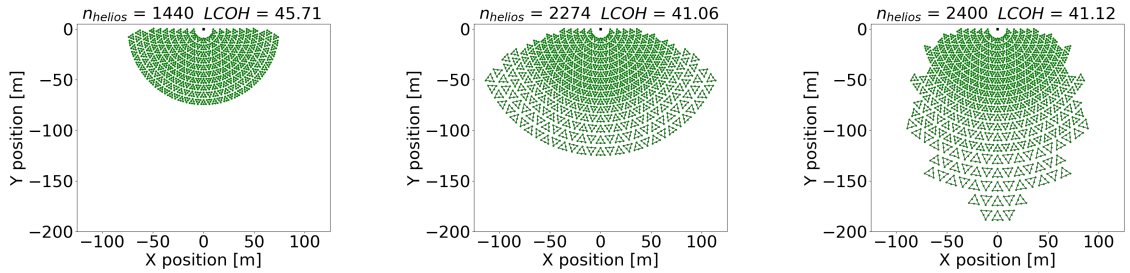

(a) 10 row field. (b) 15 row field. (c) 20 row field.

Figure 5.11: Resulting radial field designs for various rows with a 20 m tower.

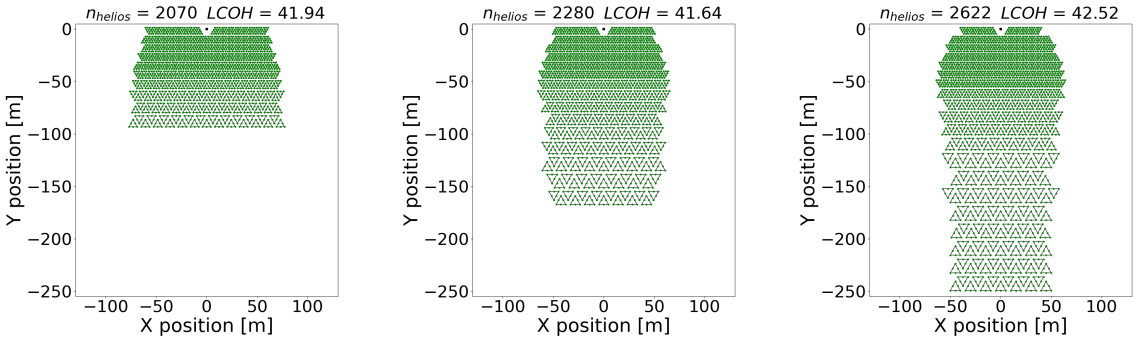

(a) 10 row field. (b) 15 row field. (c) 20 row field.

Figure 5.12: Resulting cornfield designs for various rows with a 20 m tower.

5.5.2 The 40 m tower results

Table 5.5 summarises the results for the three different sized fields and the two different field types for the 40 m tower. The 10 row radial field is again the worst performer, for the same reason as previously discussed. The rest of the fields perform comparably, again indicating at this tower height the exact field layout is less important, and packing the pods in a dense manner is sufficient to achieve a good layout.

Table 5.5: Results for 40 m tower given the maximum number of rows.

Layout	Starting values	Optimum # heliostats	$\eta_{opt,a}$	min $LCOH$
Radial	10	1 452	63.41 %	41.29 \$/MWh$_{th}$
	15	1 938	60.16 %	38.57 \$/MWh$_{th}$
	20	1 944	58.89 %	38.76 \$/MWh$_{th}$
Cornfield	10	1 758	64.23 %	38.21 \$/MWh$_{th}$
	15	1 920	61.60 %	38.29 \$/MWh$_{th}$
	20	1 950	59.16 %	38.81 \$/MWh$_{th}$

Figures 5.13 and 5.14 show the resulting field layouts for the radial and cornfield layouts, respectively. The radial fields are either fully dense or mostly dense (for the larger fields). The cornfield layouts contain larger dense regions than for the fields of the 20 m tower.

The taller tower leads to heliostats tracking 'flatter' (relative to the ground) which gives reduced blocking and shading losses in the field. This leads to the optimal field being dense (as blocking and shading is reduced) to avoid increased attenuation and spillage losses.

In Figures 5.13 and 5.14 the fields are mostly densely packed and therefore they yield similar results, irrespective of the exact layout. This is seen in Figure 5.13c where the optimiser reduced the size of the last three rows. Even for Figures 5.14b and 5.14c, where the field footprint is large, 79 % and 75 % of heliostats are located on pods with side lengths set to the minimum length in the first 10 rows. Figure 5.14a with only 10 rows has the best result, and all of its pods have the minimum side length. Compared to Figures 5.14b and 5.14c, these larger fields have heliostats collecting more energy but the added CAPEX that results from more heliostats balances the *LCOH*.

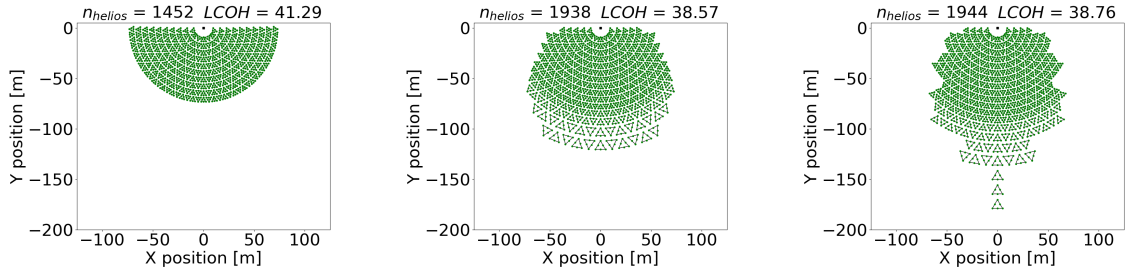

(a) 10 row field. (b) 15 row field. (c) 20 row field.

Figure 5.13: Resulting radial field designs for various rows with a 40 m tower.

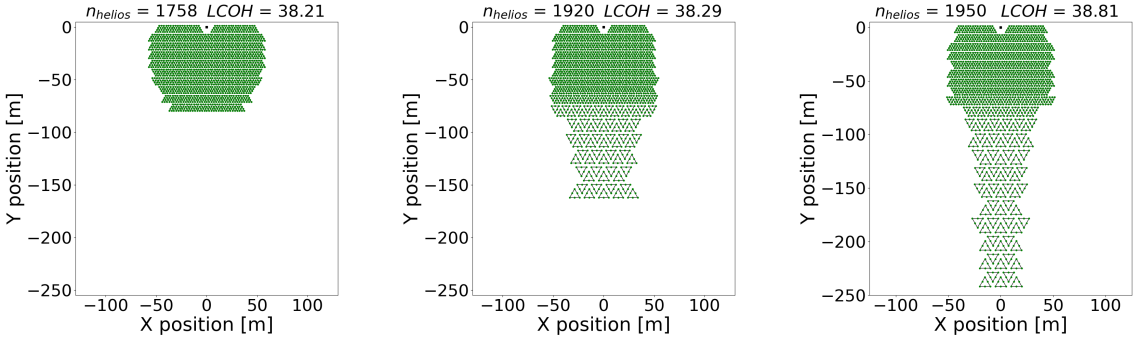

(a) 10 row field. (b) 15 row field. (c) 20 row field.

Figure 5.14: Resulting radial field designs for various rows with a 40 m tower.

5.5.3 Conclusion to number of rows investigation

From the results of this section it was shown that the size of the allowed field influences the final shape of the field. For the larger allowed fields the optimiser did not remove 'surplus' rows but rather adapted the field for the number of allowed rows. It is especially interesting that the 20 row cornfield for the 40 m tower did not reduce row widths to near zero for rows near the back of the field. It has been seen that for this tower height a dense field is best, therefore these far away rows seem unnecessary. A possible explanation might be

that the optimiser reduced the number of heliostats for these far away rows by increasing the pod side lengths to near maximum. This would also reduce the total heliostat surface area in these rows, similar to decreasing the row widths. This theory is supported by the fact that the majority of the heliostats in these fields are within the first 10 rows.

For the 20 m tower, if the field was larger than the dense region, all fields showed that monotonically increasing pod sizes leads to the optimal fields. This indicates that increasing pod sizes as the pods are placed further from the tower mimics the benefits offered by the radial stagger layout. The 40 m tower fields yield better results than the 20 m tower. Theses fields are mostly dense, requiring fewer different HelioPod™ sizes. This would likely simplify manufacturing. The 20 m tower fields are more spread out, requiring more sophisticated field layout designs.

5.6 Comparison of newly developed to existing HelioPod™ field layouts

The newly developed HelioPod™ field layouts were compared to the heuristic field layout methodology developed by Lubkoll et al. (2018). This was done for a 20 m and a 40 m tower. For the 20 m tower the radial field layout with 15 rows was used (Figure 5.11b). For the 40 m tower the cornfield layout with 10 rows was used (Figure 5.14a). These were the best performing fields developed in this thesis for the respective tower heights. These fields were compared with the same number of heliostats in the circular fields. This allows a fair comparison of field performance. The heuristic fields are shown in Figure 5.15.

Table 5.6 summarises the results comparing the different fields for the same tower heights. The relative difference column shows the difference between the $LCOH$ for the two field design methodologies with the same tower height. For both tower heights the newly developed field layout methodology outperforms the heuristic methodology. The difference is more significant for the shorter tower. This is to be expected, as all results presented have shown that the taller tower only requires a dense field, which the heuristic methodology produces. For the shorter tower more spacing is required for pods that are further away, to minimize blocking and shading, therefore the heuristic methodology is expected to perform worse.

Table 5.6: Comparison of heuristic to newly developed HelioPod™ field design methodology.

Tower height	Field	# heliostats	$\eta_{opt,a}$	min $LCOH$	Relative difference
20 m	Heuristic	2 274	40.41 %	45.65 \$/MWh$_{th}$	-
	Optimised radial	2 274	46.64 %	41.06 \$/MWh$_{th}$	11.18 %
40 m	Heuristic	1 758	60.21 %	39.39 \$/MWh$_{th}$	-
	Optimised cornfield	1 758	64.23 %	38.21 \$/MWh$_{th}$	3.09 %

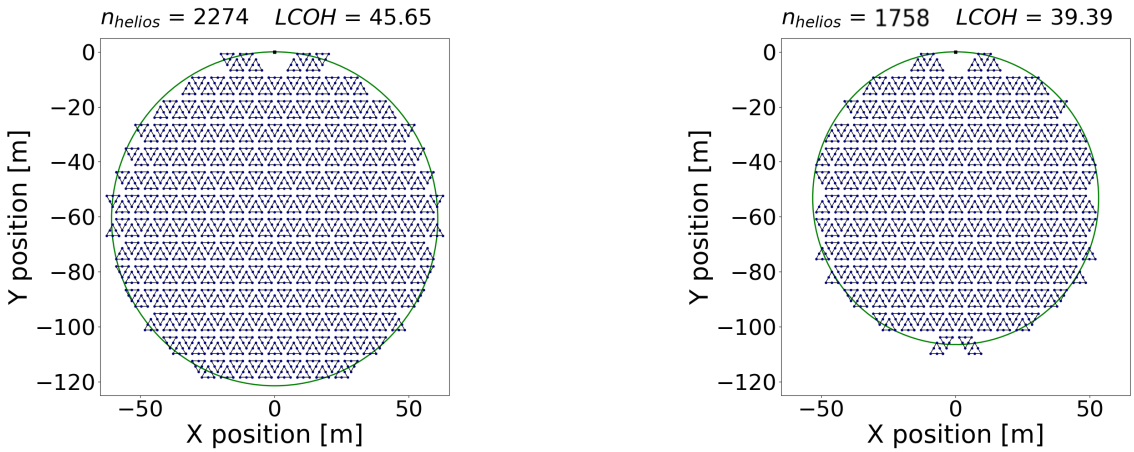

(a) 20 m tower field.

(b) 40 m tower field.

Figure 5.15: Heuristic HelioPod™ field layouts.

5.7 HelioPod™ field layout conclusion

In this chapter the field layout design tool SolarPilot was used to investigate what optimised individual heliostat radial stagger field layouts look like for different tower and receiver parameters. These results inspired the development of two algorithms for the design of pod field layouts. These algorithms attempted to replicate the benefits offered by the radial stagger pattern field layout approach. The developed algorithms parametrised the field width and pod sizes, which through an optimisation routine was used to design optimised HelioPod™ layouts for a reference plant.

The algorithms were implemented and a number of different parameters affecting the design of the pod fields were investigated: tower height, allowed field size and field starting values. From these investigations it was determined that the shorter tower requires a more spread out field. This requires a sophisticated field layout to minimize blocking and shading. It was shown for these fields that monotonically increasing the pod sizes as the distance between the pod and tower increases, improved the field's optical performance. For a taller tower a densely packed field layout performed well and consequently different sized pods were not required.

For the reference plant the economics was such that a taller tower and dense field lead to the best economic performance. The reduced CAPEX of a shorter tower is outweighed by the improved optical performance of the field for the taller tower. However the work presented provides a reference for future HelioPod™ field designs, where shorter towers may be studied further. The work showed that the algorithms that were developed could adapt the HelioPod™ field to varying plant parameters, such as tower height, to improve performance. This is seen in the differing designs of the best performing fields for the two different tower heights.

6 Case study: CST plant to provide process heat to a Manganese smelter

In this section a case study for a CST plant providing high-temperature process heat to a Manganese ore smelter is developed. The case study provides the necessary details from which a CST plant can be sized and modelled using the methodology developed in previous chapters.

The CST plant is sized for a hypothetical 30 MW_e smelter. Compared to the overview of smelting operations in South Africa provided in section 2.1.5, this represents a medium sized smelter by South African standards. For a smelter operating at 40 ton/hr, where the ore is pre-heated to 600 °C, Hockaday et al. (2020) determined this would require a constant thermal power supply of 13.6 MW_{th} to the pre-heater unit. The CST plant with backup electrical heaters are sized to meet this load.

As discussed in section 2.1 the region around Hotazel in the Northern Cape contains the largest land based Manganese reserves in the world. This region also experiences world class solar resource (see the world DNI map in Figures 2.7). The Northern Cape also has extensive existing rail infrastructure to the Manganese export terminals at Saldanha Bay and Port Elizabeth, with plans existing to upgrade these lines (Transnet, 2018). Figure 6.1b shows the relevant existing rail lines. The combination of high quality solar resource, existing transport infrastructure and the ore reserves make the Northern Cape region around Hotazel an attractive location for a Manganese smelter with CST based pre-heating. For these reasons the case study will investigate the performance of a plant near Hotazel, the location is shown as a yellow star in Figure 6.1a.

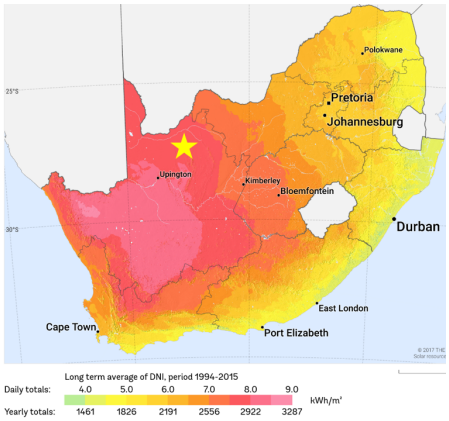

(a) DNI solar resource map of RSA (SolarGIS, 2019).

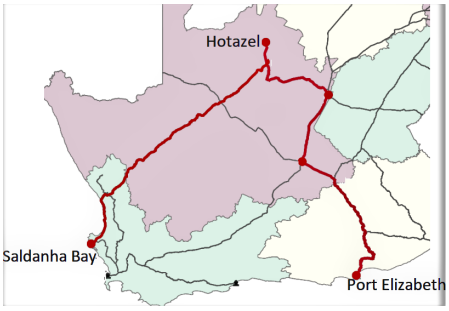

(b) Existing minerals export rail infrastructure (Transnet, 2017).

Figure 6.1: Location of proposed smelter.

In section 2.1.6 the challenges facing the Manganese sector in South Africa were discussed. Two of these being rising electric tariffs and electricity availability. A Manganese smelter with CST derived process heat for pre-heating could alleviate these challenges to some extent by reducing the electrical energy required by the smelter. Furthermore, as discussed in section 2.1.4, South Africa exports the majority of its Manganese as ore, before any beneficiation process. This means lower export revenue per kilogram of exported mineral,

compared to exporting ferroalloy. For these reasons it might be an attractive proposition to invest in future Manganese smelters in the Northern Cape region.

6.1 CST plant design

Designing the CST plant entails designing the heliostat field layout, selecting an appropriate amount of TES and a solar multiple (SM). Following the design, the solar plant model can be used to evaluate the optical, energy and economic performance of the plant. However, it is not obvious a priori what size field or which combination of TES and SM parameters lead to an optimal CST plant.

To determine the best combination of TES and SM, ten heliostat fields are designed with increasing size using the field layout optimisation methodology developed in Chapter 5. An additional constraint is implemented to cap the field size by constraining the field power at solar noon on equinox (the solar design condition) between an upper and lower bound. For each of the ten fields these bounds are incremented to provide ten fields of increasing size in terms of number of heliostats and annual collected energy. For each field a parametric study is implemented to investigate the effect of varying both TES and SM on the resulting *LCOH*. The SM is a function of both the output to process and the field's design power, see Equation 14. For each of the ten fields the design power is fixed and the output to process varied, through this the SM is parametrized.

The optimum combination of TES and SM will vary depending on the size of the field. Such studies are typical for CST plant designs, an example of which can be found in the work of Sioshansi and Denholm (2010). In Chapter 5 it was shown that a 40 m tower with a dense field produced the best economic performance. Therefore these fields will be designed with this tower height and a 10 row cornfield layout field.

Figure 6.2a depicts the lowest *LCOH* result from the parametric study performed on each of the ten different sized fields, as well as the size of the field in terms of power at the design condition (x axis) and total annual solar energy captured at the receiver by each field (right y axis). The reported *LCOH* is for the best combination of TES and SM for each field, and may differ between fields. From Figure 6.2a it can be seen the field delivering 3.3 MW_{th} at the design condition yields the lowest *LCOH*. This is the field selected for the case study scenario. Figure 6.2b shows the 3.3 MW_{th} field layout, the other fields can be seen in Figure D1 in Appendix D.1. Figure 6.3a shows the results for the TES and SM parametric study for the 3.3 MW_{th} field. The lowest *LCOH* is achieved with 14 hours of TES and a SM of 3.67. This corresponds to providing 0.9 MW_{th} to the pre-heater. For each of the ten fields designed such a surface was produced from the parametric study to determine the lowest *LCOH*.

Until now all results presented assumed all heliostats in the field have ideal focal length (mirror curvature). This is unrealistic due to the practical implications of requiring the equipment to manufacturing a unique focal length for each heliostat. In reality a heliostat field has a finite set of different focal lengths. A parametric study was performed to evaluate the economic effect of varying the number focal lengths in the field. More focal lengths leads to improved optical performance, and therefore collecting more energy. The result of this study is shown in Figure 6.3b. The results show that the field's performance converges to the ideal scenario result (each heliostat having perfect focal length for its position) as the number of focal lengths increase. This does not include the added manufacturing cost

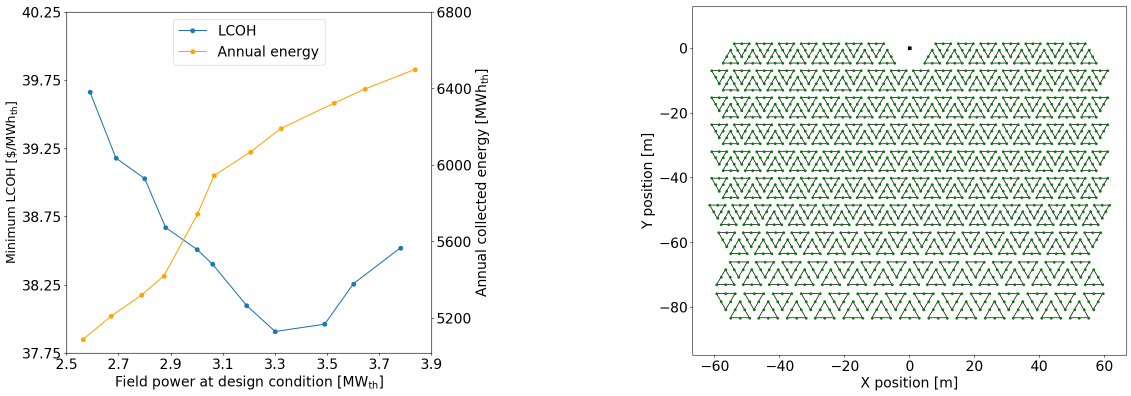

(a) Performance of the various fields. (b) 3.3 MW_{th} field layout.

Figure 6.2: 3.3 MW_{th} CST plant design results.

of producing multiple focal lengths. More detail on this topic can be found in Appendix D.2.

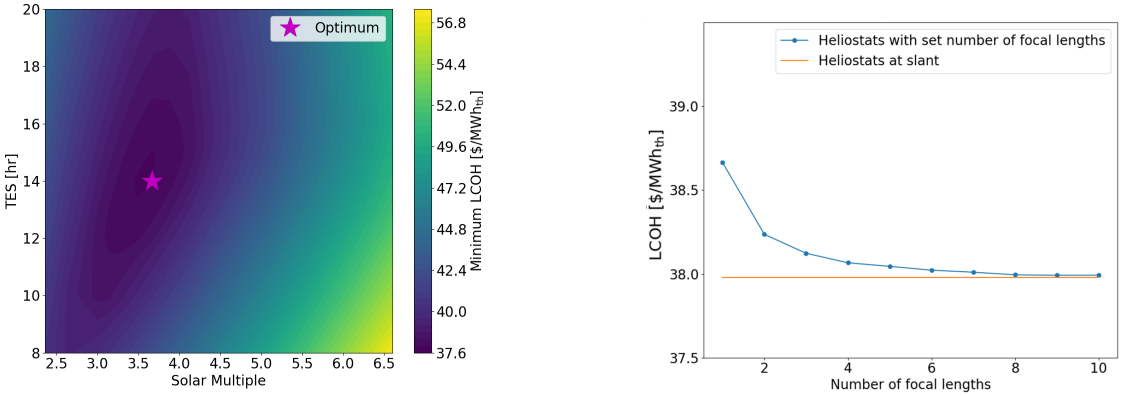

(a) TES and SM parametric study. (b) Focal length parametric study.

Figure 6.3: 3.3 MW_{th} CST plant design study results.

6.2 Summary of case study results

Table 6.1 summarises the results and parameters for the CST plant, smelter, location, optical, energy and economic performance of the concept. To satisfy a thermal demand greater than the CentRec© thermal rating of 2.5 MW_{th} a multi-tower plant is required, this is the approach used by Amsbeck et al. (2014b) and Amsbeck et al. (2015). In section 6.1 it was determined that the best performing CentRec© plant would provide 0.9 MW_{th}, 15 of these tower field units are required to meet the pre-heater demand. The details for the single tower field unit is provided under the heading "Single tower CST unit"; here the total reflective surface area, annual optical performance, solar multiple and total annual collected energy are provided.

From Table 6.1 it is seen that each tower plant provides 6 149 MWh of solar energy, for all 15 plants this corresponds to a solar capacity factor of 77 %. The shortfall is met with

electrical backup heaters. The total thermal demand is met by the solar plant with backup electric heaters, with a final $LCOH$ of 37.96 \$/MWh$_{th}$, this is if the optimal operating strategy is implemented. For the heuristic operating strategy the $LCOH$ would increase to 43.03 \$/MWh$_{th}$. If the full pre-heater thermal demand was met with electric heaters only the LCOH$_{e,total}$ would be 62.08 \$/MWh$_{th}$. Compared to this, the optimal solar-electric system provides energy with a 38.85 % cost reduction. This only considers the cost of electricity and not the electric heating system CAPEX (as discussed in section 3.3.1).

Table 6.1: Summary of case study results.

	Parameter	Value
Smelter	Smelter rating	30 MW$_e$
	Pre-heater rating	13.6 MW$_{th}$
	Pre-heat temperature	600°C
Site	Latitude	27.240 S
	Longitude	22.902 E
	Annual DNI	2 796 kWh $\cdot$ m^{-2}
Single tower CST unit	A$_{sf,single}$	4 343 m^2
	$\eta_{opt,a}$	62.7 %
	TES	14 hrs
	SM	3.67
	$\dot{Q}_{out}$	0.9 MW$_{th}$
	$Q_{s,a}$	6 149 MWh$_{th}$
Total CST plant	Towers	15
	A$_{sf,total}$	65 145 m^2
Economics	LCOH$_s$	36.69 \$/MWh$_{th}$
	LCOH$_e$	41.98 \$/MWh$_{th}$
	Optimal $LCOH$	37.96 \$/MWh$_{th}$
	Heuristic $LCOH$	43.03 \$/MWh$_{th}$
	LCOH$_{e,total}$[1]	62.08 \$/MWh$_{th}$
	Savings[2]	38.85 %

1: if all heat required for pre-heating is supplied by the electric heaters only
2 : $(LCOH - \text{LCOH}_{e,total})\,/\text{LCOH}_{e,total}$

Hockaday (2019) investigated the costs of several common sources for process heat for application in minerals processing. In the author's findings the cost of diesel and coal derived process heat amounted to: 143.45 \$/MWh$_{th}$ and 19.30 \$/MWh$_{th}$ respectively. Compared to the findings in this thesis for the optimised combined solar-electric plant the cost is 37.96 \$/MWh$_{th}$. Therefore coal is still lower cost, but the CST plant outperforms diesel combustion. This is relevant as some Manganese sinter plants in the Northern Cape burn diesel for process heat (Lubkoll et al., 2018). It is possible that the gap between the cost of CST derived process heat and coal may close in the future. Driven by technological advancements, globally the cost of CSP, in terms of levelised cost of electricity, declined 47 % between 2010 to 2019 (IRENA, 2020). Another halving of costs would put CST on parity with coal. Additionally potential future carbon tax on coal combustion would increase the LCOH of coal combustion. It is possible these factors will lead to CST derived process heat being competitive against both diesel and coal in the future.

7 Conclusion

This chapter provides an overview of the work undertaken, a summary of the findings, recommendations for future work and some concluding remarks. The purpose of this thesis was to investigate the potential for CST technologies to provide high-temperature process heat to the minerals processing industry, with specific application to Manganese smelting. The objectives outlined to achieve this were:

1. Develop an optical, energy and economic model for the CST plant to predict the plant performance.
2. Determine the optimal operating strategy of the CST plant that minimizes the cost of the provided energy.
3. Investigate optimised large HelioPod™ field layouts.
4. Conduct a case study for a CST plant providing process heat to a Manganese smelter in South Africa.

7.1 Overview of work

The investigation of this thesis required the development of a model for the CST plant. The model considered the plant's optical, energy and economic performance. For the optical model the Sunflower ray tracing software was used to evaluate the solar radiation collected by the heliostat field. The energy model applied energy balances on the receiver and TES to determine available energy and power. In these energy balances the thermal losses from the receiver and TES were modelled as hourly efficiencies. The receiver efficiency was taken from published data of a FEM heat transfer model of the receiver. The TES efficiency was taken from published data of simulations for particle TES.

Smelters operate under steady conditions and therefore the addition of pre-heating should not disrupt the steady operation. To ensure a constant heat supply to the ore pre-heater unit backup electric heaters are coupled to the CST plant to supplement the heat supply if the solar system experiences a shortfall. This electric energy is priced using a time-of-use tariff. The TES dispatch profile was developed to minimize the cost of the backup electrical heat by shifting TES dispatch to periods of high electric tariff. This was the operating strategy developed for the CST plant. Previous studies have been completed on the application of CST technologies to provide process heat for the minerals processing industry but these studies typically implemented heuristic or simple operating strategies. It was shown that compared to such an heuristic strategy the optimised discharge profile significantly reduced the plant's LCOH.

The thesis investigated the use of a novel heliostat technology, the HelioPod™, which has six individual heliostats on a common supporting structure. The majority of existing literature on optimal heliostat field layout is aimed at individual free standing heliostats and is therefore not directly applicable to the design of HelioPod™ fields. Previous studies of HelioPod™ based applications consisted of small fields (where layout is less import) or assumed heuristic fields layouts. Therefore an effort was made to develop optimised HelioPod™ layouts for the larger fields required in this study. The work focussed on transferring the benefits offered by the popular radial stagger layout to HelioPod fields. This was achieved by parametrising the HelioPod's size as a way to induce decreasing field

density away from the tower. This was a unique approach to pod field design and proved effective for large field sizes with shorter towers.

A case study was developed for a CST plant to provide high-temperature process heat to a Manganese smelting operation. The optimisation methods developed in the work were used to design the optimal CST plant for this application. The Northern Cape was selected as the location. This location has excellent solar resource and is in close vicinity to existing rail infrastructure for exporting the ferroalloy product. The location has the potential to benefit from expanded future electric infrastructure due to new renewable energy plants in the region. The case study results generated provide an economic performance parameter which can be used to compare against competing process heat sources and technologies.

7.2 Summary of findings

There are three sets of findings in this thesis; the optimised operating strategy, the design of optimised HelioPod™ field layouts and the economic performance of CST derived process heat for a smelter.

In chapter 4 an optimised TES dispatch profile was developed to ensure the cost of electric backup heat (used to cover any shortfall in solar derived heat) is minimized. This dispatch profile was compared to a simple heuristic strategy. For the optimised dispatch profile it was shown that using the TES to hold back solar derived heat during periods of low electric tariff, in order to meet the smelter demand during periods of high electric tariff, lead to reduced cost of electric backup heat. Compared to the heuristic strategy which uses the solar heat as available and until the TES is depleted, the cost of the produced heat decreased from 43.03 \$/MWh$_{th}$ to 37.96 \$/MWh$_{th}$.

In chapter 5 the layout of HelioPod™ fields was investigated. Previous work on HelioPod™ fields were aimed at small fields of 20 pods, whereas fields in this thesis required in excess of 250 pods. The work sought to incorporate the understanding from the existing body of literature on optimised heliostat field layouts for free-form fields, to the design of pod fields. The central concept was to vary pod sizes to replicate the reduction in blocking and shading provided by the radial stagger layout method for free-form fields. The results showed that for a shorter tower (20 m) this leads to improved optical performance compared to only one pod size in the field. However for a taller tower (40 m) this was not necessary for the size fields required in this work. This is because the increased tower height leads to the heliostats tracking orientation being 'flatter' to the ground, thereby reducing blocking and shading. For a tall tower a densely packed field provides good optical performance. This work has generated new understanding for good design of larger HelioPod™ fields.

In chapter 6 a case study for a CST plant providing process heat to a Manganese smelter was completed. The CST plant was modelled using the operating strategy and HelioPod™ field layout methods developed. It was shown that these methods improved the economic performance for the CST plant compared to heuristic operating strategies and field layout methods. In the case study numerous sized fields were designed, and for each a parametric study was completed to determine each field's optimal combination of TES size and SM which results in the minimal LCOH. From this the best performing field was selected for the case study. The economic performance of this CST plant was compared

to the cost of coal and diesel derived process heat, these values were taken from literature. It was shown that the cost for CST process heat is lower than diesel but still significantly more than coal based process heat.

7.3 Recommendations for future work

The CST technology (particles as HTF) upon which the plant in this thesis is based on is still in the research phase. Therefore as this technology progresses to the pilot plant and eventually commercial phase the concept should be re-evaluated based on updated economics as the technologies mature.

As discussed in chapter 6, CST derived process heat is still costlier than coal derived process heat. However this does not take into account any potential carbon tax on fossil fuel derived process heat or other favourable legislation aimed at promoting alternative and sustainable energy sources. These factors should be investigated as they may improve the outlook for CST derived process heat.

Over the last decade the cost of photovoltaic (PV) systems has drastically decreased and a large uptake of the technology has been experienced. In South Africa large energy users such as the mining and chemical processing industries are starting to consider large embedded generation PV systems to meet their energy demand. This is occurring in the context of rising electric tariffs from the national energy utility. Given this existing interest a PV system providing electrical energy as a heat source (potentially via heat pumps), coupled to TES might provide a competitive alternative to CST derived process heat. This is similar to the Carnot-battery concept. A study on this topic resulting in the LCOH of this PV-TES system could prove interesting.

7.4 Concluding remarks

In this thesis the concept of CST derived process heat for a Manganese smelter was investigated. Effort was focussed in determining how this CST plant could optimise the operation of its TES to maximise the plant's economic performance. Further effort was made to investigate how to design optimised large HelioPod™ fields by leveraging ideas from the existing literature on individual heliostat field optimised designs. The knowledge gained through these studies was incorporated into a case study for a new smelter with CST derived ore pre-heating, located in the Northern Cape region of South Africa. The LCOH of this concept was determined and compared to common existing sources of process heat, coal and diesel. It was shown that CST process heat was competitive against diesel but significantly worse than coal. However if the price reduction of CST continues on the same trend as the previous decade it is possible CST will reach cost parity with coal. The addition of carbon tax on fossil fuel combustion may serve to reduce the time for CST to reach this parity.

This thesis has shown that CST should be considered as a source of high-temperature process heat. It is already more cost effective than the more expensive fossil fuels (diesel) and within a similar order of magnitude to low cost fossil fuels (coal). The results developed in this thesis can be used to compare CST derived process heat to any other process heat source.

Appendix A Dispatch optimisation

A.1. SLSQP vs MMFD

The difference between the results of MMFD and SLSQP can be assessed by comparing their TES dispatch profiles relative to the electric tariff. This is difficult to present for a full year. A representation style of this data is taken from Wagner (2015) and shown in Figure 4.7. These figures show the dispatch profile variation for the SLSQP and MMFD optimisers, respectively, over all combined weekday hours of the year. These figures take the annual dispatch profile, break it down into 24 separate datasets, each representing the dispatch profile for the i^{th} hour of a weekday. For each hour's TES discharge dataset a box and whisker plot is shown. The whiskers show the range of the data, the box bounds the first and third quartile, the median is shown as a solid orange line and the mean as a black dotted line.

Comparing Figures 4.7 it can see that MMFD has more variation over the early morning peak tariff periods (hours 7, 8 and 9) than SLSQP, which has virtually no variation over this period. For the evening peak tariff periods (hours 19 and 20) SLSQP again shows less variation than MMFD. These results indicate when the tariff is high, SLSQP more frequently than MMFD, meets the full thermal demand using lower cost solar heat, and therefore provides a lower objective function value.

A.2. Dispatch optimisation with penalty function

As discussed in section 4.3.6, the solution to the initial formulation of the dispatch optimisation problem yielded some interesting phenomena for periods of low electric tariff. The dispatch profile would follow the shape of the initial values. This lead to unrealistic profiles for these time periods.

The optimiser was tested with several initial values, all leading to different shapes over the low tariff periods, but all following the shape of the initial values. Interestingly, although the dispatch profile varied for these periods the resulting objective function value change was negligible.

This was an indication that in these regions the gradients of the design space were low, and therefore the optimiser would not move significantly further from the initial starting values. Additionally as the objective function is inherently poorly scaled due to the fluctuation of the electric tariff, these low tariff periods contribute less to the objective function that the high tariff periods. However it is undesirable to have a dispatch profile which fluctuate frequently as this would require impractical operation of the electric heaters.

One solution to remove this behaviour is to update the objective function with a penalty function aimed at removing this behaviour. The penalty function is the summations of the square of all the gradients. This is an indication of profile 'smoothness'. The more the dispatch profile fluctuates the greater the penalty function value will be. Therefore forcing the optimiser to seek out a 'smoother' profile. The updated objective function is shown below:

$$min \left\{ \sum_{i=1}^{8760} (\dot{Q}_{out} - \dot{x}_i) C_i + \rho \sum_{i=1}^{8760} (\dot{x}_i - \dot{x}_{i+1})^2 \right\}, \tag{27}$$

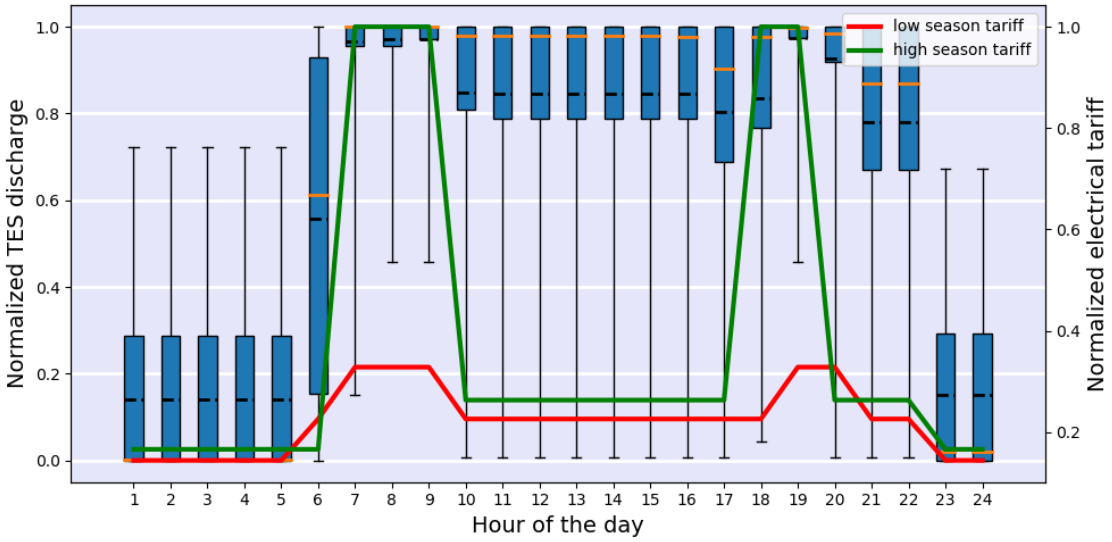

(a) MMFD results.

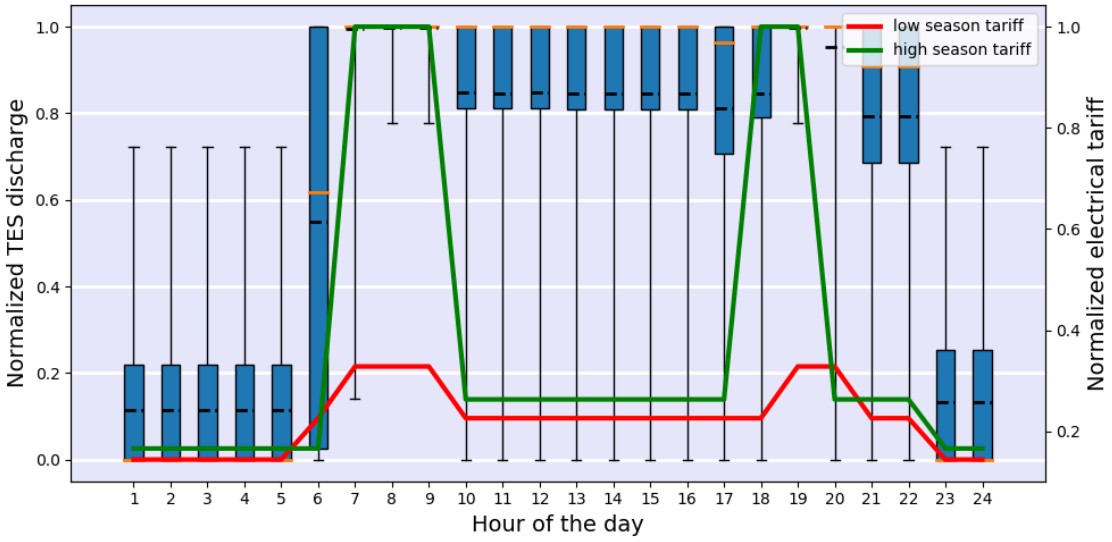

(b) SLSQP results.

Figure A1: Box and whisker plots representing the variation of TES discharge for all combined weekday hours.

where the first term in the braces represents the cost of electrical heat and the second term is a penalty function implemented to reduce fluctuations in the discharge. From the first term; $\dot{Q}_{out}$ is the heat required by the process, $\dot{x}_i$ is the design variable (TES discharge), C_i is the electrical tariff for the specific hour. From the second term, ρ is the penalty constant and the terms in parenthesis represents the sum of all finite difference gradients between successive time-steps. The denominator is always one as the change in the x direction is one hour.

The penalty function succeeds in 'smoothing' the dispatch profile over the low tariff peri-

ods, irrespective of the initial values. This is shown in in Figure A2. Here the resulting dispatch profile is shown for a number of different starting values, against the electric tariff. Notice over the extended low tariff periods (around hours 4 000 and 4 200) how most starting values yield similar dispatch profiles. This is in contrast to the results without the penalty function. There is some difference between some of the starting values, notably around hour 4 200 for the heuristic starting values. It is possible this difference is caused by new local minima created through the addition of the penalty function.

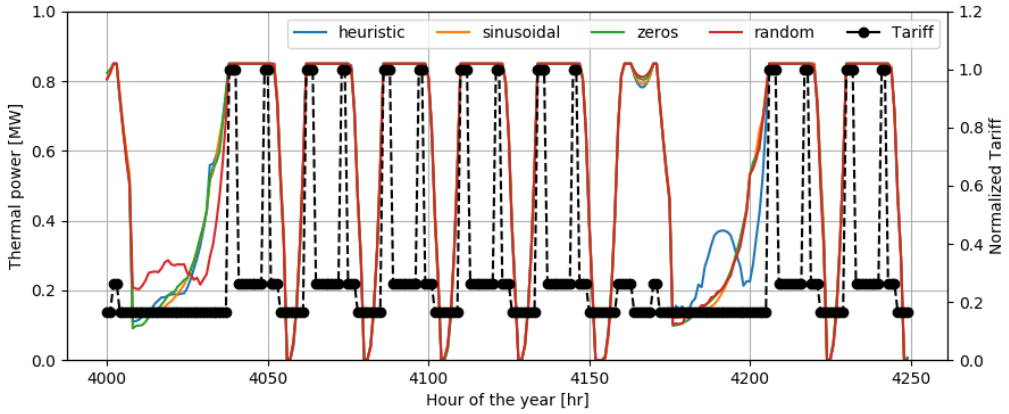

Figure A2: Results of adding penalty function to SLSQP.

The penalty function's constant, ρ, is determined through a parametric study. The aim is to find a constant whose value produces the minimal effect on the objective function while providing the desired 'smoothing'. The results of this are shown in Figure A3. The three lines represent the execution time, objective function value at the optimum and the sum of the gradients (an indicator for 'smoothness'). All lines have been normalized by their maximum value in order to display on a single plot. It can be seen that as the penalty value increases the execution time increases in a near linear manner. The objective function of the optimum remains steady. The sum of gradients experiences an initial sharp decreases, then slows significantly. From these results it is concludes a lower penalty value of 0.1 is sufficient to remove the undesirable dispatch fluctuation over periods of extended low tariff without worsening the objective function. This does come at an increase in computational expense.

The implementation of SLSQP with a penalty function is compared to the MMFD + SLSQP implementation (as used in the main text). Both solutions provide a similar sum of gradients, i.e. both return desirable dispatch profiles. The comparison of the implementations are summarised in Table A1. It can be seen that the penalty function implementation requires double the execution time for a similar result.

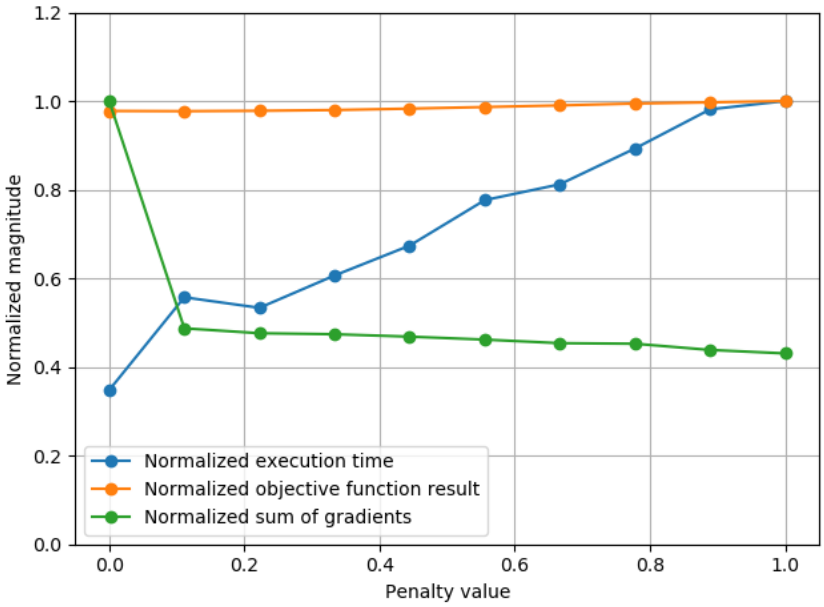

Figure A3: optimising dispatch profile with added penalty function for varying values of the penalty parameter.

Table A1: Comparison of dispatch optimisation implementation.

Parameter	MMFD + SLSQP	SLSQP + penalty function	Relative difference[1]
time-horizon	72 hours	72 hours	-
execution time	45 s	96 s	-53 %
normalized $f(\mathbf{x}^*)$	1	1.02	-2 %
sum of gradients	121.4	120.6	+0.66 %

[1] $(MMFD + SLSQP - SLSQP + penalty function)/(SLSQP + penalty function)$

To conclude, implementing a penalty function to correct the SLSQP optimiser's behaviour for the low gradient regions is shown to work successfully. However it was shown to introduce local minima and is significantly slower than the double optimiser solution. For these reasons this solution is not implemented as the final dispatch optimisation implementation.

Appendix B Ray tracer validation

The Sunflower ray tracer is validated against two established tools, Tonatiuh and SolarPilot. A test scenario is used to compare the three tools. All three tools are used to analyse the same scenario with the resulting thermal power on the receiver compared.

B.1. Test scenarios

This section describes the test scenarios created to compare the solar ray tracers. Details required for modelling the heliostat field, receiver and tower are provided below. Both a small and larger field are tested. The results are produced for a location near Stellenbosch.

B.1.1. Heliostat fields

Figure B1a shows the field layout of the smaller field. This field is based on the HelioPod™ field layout originally implemented at the Helio100 project (Domínguez-Bravo et al., 2016). The field contains 115 heliostats. The tower is 12.2 m high, with the centre of the receiver at 11.1 m.

Figure B1b showes the field layout for the larger field. Here the HelioPods are placed in consecutive straight rows and the length of each row is determined by a bounding circle. The bounding circle has a 50 m radius, resulting in 269 pods. The tower is 42 m high, with the centre of the receiver at 40 m.

In both scenarios the tower is positioned at (0,0), the receiver is tilted downward at 45° and the receiver is modelled as a 1.1284 m × 1.1284 m square plane.

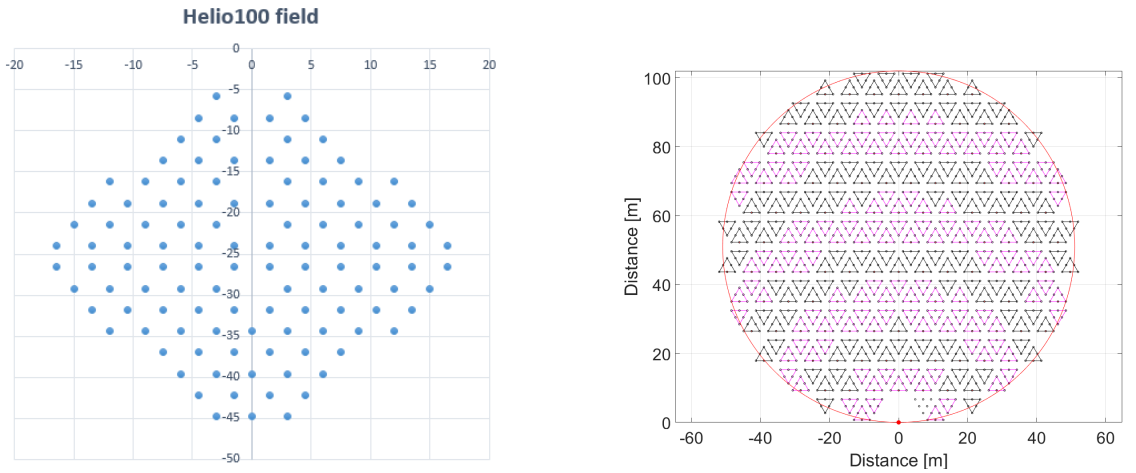

(a) Helio100 field layout.

(b) Densely packed layout.

Figure B1: Test scenarios for solar ray tracer comparison.

B.1.2. Heliostat optics

The optical parameters required for modelling the heliostat field are defined in Table B2. Each field was modelled with a single focal length.

Table B2: Heliostat optical specifications for ray tracer validation.

Parameter	Value	Units
Single facet aperture area	1.83×1.22	m^2
Facet focal length[1]	25	m
Facet focal length[2]	50	m
Combined surface slope and tracking error	1.5	mrad
Reflectivity	88	%

[1] for the smaller field, [2] for the larger field.

B.2. Single moment flux validation

This section compares the flux distribution on the receiver produced by each solar ray tracer for solar noon on the winter solstice.

The resulting thermal flux incident on the receiver is depicted on a contour map of the receiver. Figures B2 and B3 show the resulting flux maps for each ray tracer tool for the two different fields. From the images it can be seen that the shape of the incident flux is similar across all three tools. The SolarPilot simulation results in the highest maximum flux. The Sunflower tool's maximum flux is greater than Tonatiuh and less than SolarPilot.

Table B3 summaries the difference between the three tools in terms of incident flux and total power. The results are similar between all three tools for both fields.

Table B3: Ray tracer receiver flux results.

Tool	Maximum flux	Average flux	Total incident power	% diff
		Helio100		
Tonatiuh	1 177 kW/m^2	144.2 kW/m^2	183.6 kW	-
Sunflower	1 288 kW/m^2	147.2 kW/m^2	187.2 kW	+1.96 %
SolarPilot	1 346 kW/m^2	147.4 kW/m^2	187.7 kW	+2.07 %
		Densely packed		
Tonatiuh	5 282 kW/m^2	1692 kW/m^2	2154 kW	-
Sunflower	5 894 kW/m^2	1729 kW/m^2	2201 kW	+2.18 %
SolarPilot	5 987 kW/m^2	1737 kW/m^2	2211 kW	+2.65%

B.3. Comparison of ray tracers across varying sun angles

The three different solar-tracers were used to simulate the test scenarios across various solar azimuth and elevation angles. Summer and winter solstice and equinox are simulated with hourly resolution.

The results for the Helio100 and densely packed field are shown in Figure B4a and B4b, respectively. The second day can be seen to have low DNI value, this is due to cloud cover. From these figures it can be seen that the ray tracers all perform comparably across a range of solar angles, for both the small field and the large field.

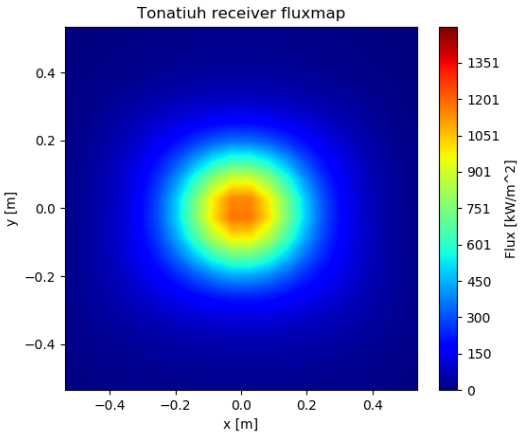

(a) Tonatiuh fluxmap.

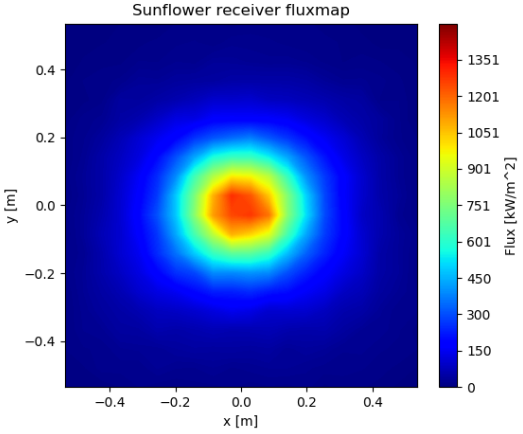

(b) Sunflower fluxmap.

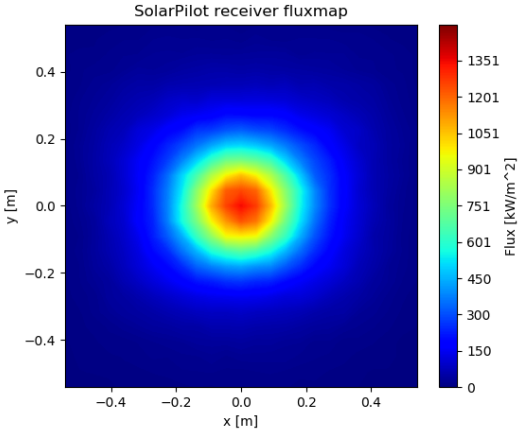

(c) SolarPilot fluxmap.

Figure B2: Resulting receiver fluxmap for the smaller field by different ray tracers.

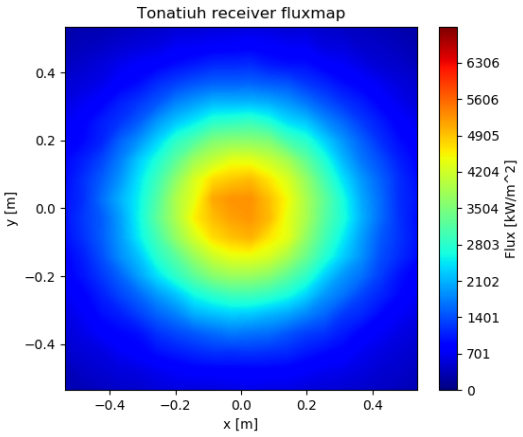

(a) Tonatiuh fluxmap.

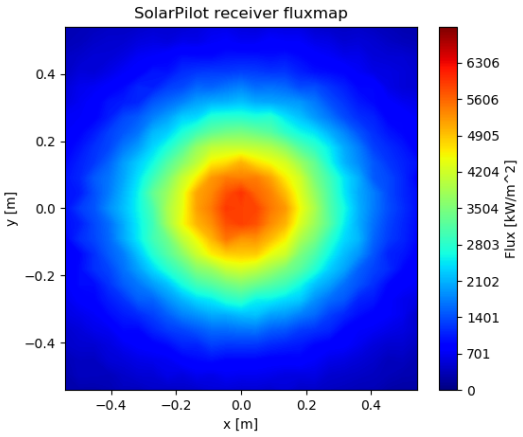

(b) Sunflower fluxmap.

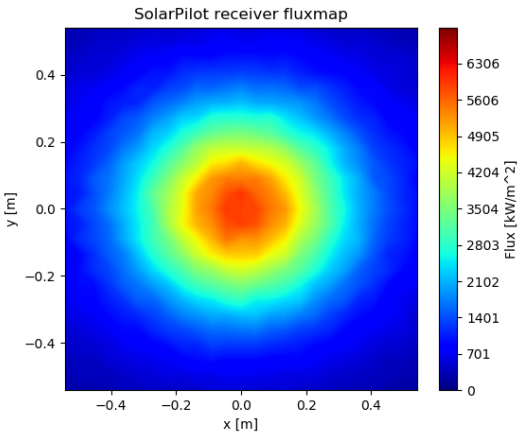

(c) SolarPilot fluxmap.

Figure B3: Resulting receiver fluxmap for the larger field by different ray tracers.

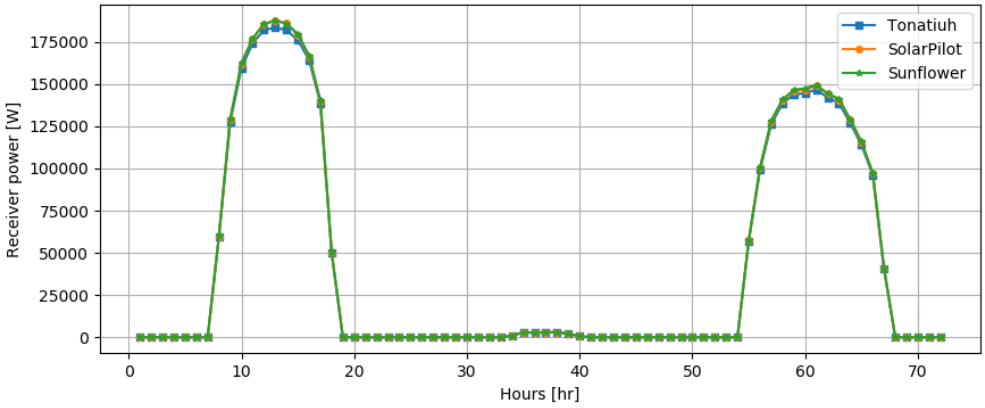

(a) Helio100 field design day simulations by three solar ray tracers.

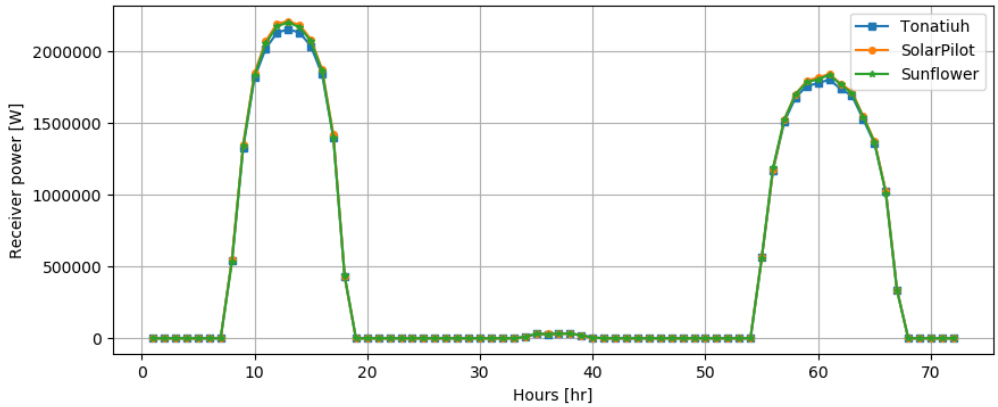

(b) Densely packed field design day simulations by three solar ray tracers.

Figure B4: Comparing three different ray tracers across varying solar angles.

B.4. Annual modelling results

The ray tracers annual optical efficiency is compared by using each to generate an optical efficiency meta-model, as discussed in section 3.1.4. The optical model is used to determine the field's annual optical efficiency. The annual optical efficiency and total power available at the receiver are then used to compare the ray tracers.

The results of the annual modelling is shown in Table B4. Again the results are similar across all three tools.

Table B4: Annual modelling results comparing three different ray tracers.

Ray Tracer	Annual receiver energy	Annual optical efficiency	% diff
	Helio100		
Tonatiuh	372.6 MWh	64.05 %	-
Sunflower	379.1 MWh	65.17 %	+1.75 %
SolarPilot	378.9 MWh	65.13 %	+1.69 %
	Densely packed		
Tonatiuh	4 164 MWh	51.00 %	-
Sunflower	4 210 MWh	51.56 %	+1.09 %
SolarPilot	4 246 MWh	52.00 %	+1.97 %

B.4. Ray tracer validation conclusion

From Figures B2 and B3 it can concluded that there is some difference in terms of maximum incident flux between the three tools, but as summarised in Table B3 and can be seen in Figure B4 the total incident power on the receiver is very similar. The total incident power is of greater importance than the resulting flux distribution as this is used in the plant energy balance.

Appendix C Field layout optimisation alternative algorithms performance

It is known that performance of an optimisation algorithm is problem dependent. Therefore multiple optimisation algorithms were tested on the field layout optimisation problem. The results presented in Chapter 5 utilise the best performing algorithm. This section provides an overview of the comparative performance of the other algorithms tested.

The SLSQP optimiser from SciPy was used to solve the field layout problem. Two other algorithms were tested on the same problem, both from DOT; Fletcher-Reeves and BFGS. The tower height significantly influences the design of the field, with the shorter tower requiring a more sophisticated design. Therefore results are presented for both a 20 m and 40 m tower. The SLSQP results are repeated for ease of comparison.

C.1. The 20 m tower field design

In this section the results for the field layout optimisation using the radial field layout with a tower height of 20 m and 15 rows of HelioPods™ are presented and discussed. Each optimiser is started from two different sets of initial values; no heliostats and a full field.

The optimisers results are summarised in Table C5. All optimisers return a better performing field starting from the full field. SLSQP returns better results than either DOT optimiser, for both starting positions.

Table C5: Radial field layout optimisation results for 20 m tower with 15 rows.

Algorithm	Starting position	# heliostats	$\eta_{opt,a}$	minimum $LCOH$
SLSQP	no heliostats	2 130	44.34 %	43.20 \$/MWh$_t$
	Full field	2 274	46.64 %	41.06 \$/MWh$_t$
Fletcher-Reeves	no heliostats	2 022	45.23 %	43.55 \$/MWh$_t$
	Full field	2 286	45.44 %	41.63 \$/MWh$_t$
BFGS	no heliostats	2 118	36.75 %	49.50 \$/MWh$_t$
	Full field	2 394	45.17 %	42.16 \$/MWh$_t$

Figure C1 depicts the resulting field layouts for the DOT optimisers. For each optimiser the results from both initial field starting values are presented. It can be seen that the resulting fields, with the no heliostats starting values (Figures C1a and C1c), are quite different to any other resulting field seen before in this work. The economic and optical performance of these fields are poor. The optimiser has not converged to a minimum. For the full field starting values (Figures C1b and C1d) the resulting fields are similar to that of SLSQP. These fields performance are similar to SLSQP. SLSQP outperforms both of the DOT optimisers from both starting values for this tower height.

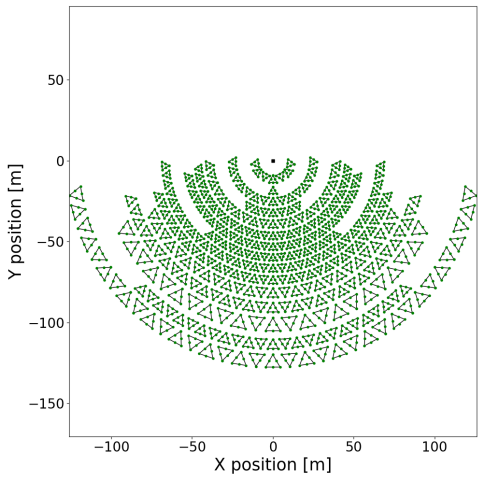

(a) Fletcher-Reeves from no heliostats as initial values.

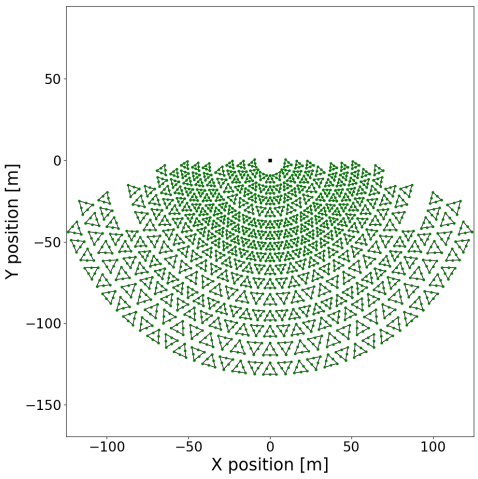

(b) Fletcher-Reeves from full field initial values.

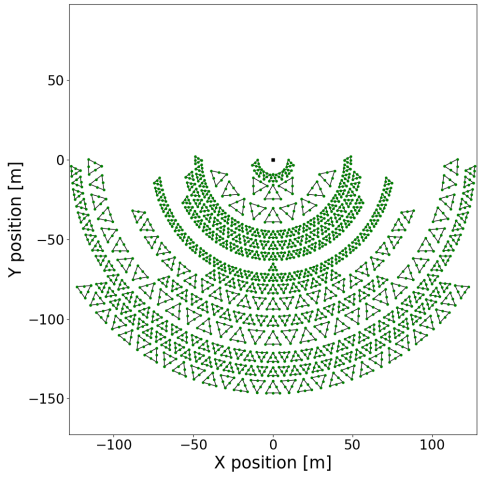

(c) BFGS from no heliostats as initial values.

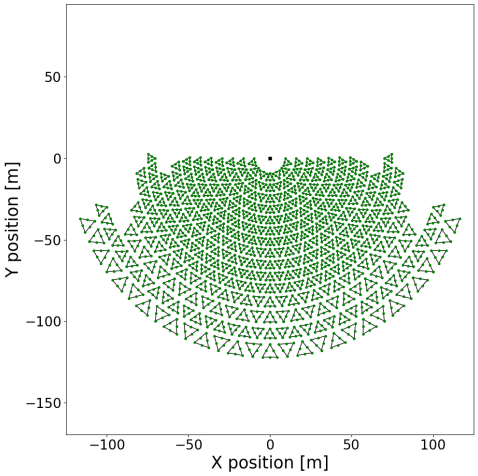

(d) BFGS from full field initial values.

Figure C1: Radial field designs for a 20 m tower with 15 rows using DOT optimisers.

C.2. The 40 m tower field design

The results for the DOT optimisers from a full field start, for the 40 m tower, are summarised in Table C6. Compared to SLSQP both optimisers perform worse. All three optimisers have similar number of heliostats.

Table C6: Radially stacked layout optimisation results for 40 m tower - 15 rows.

Algorithm	Starting position	# heliostats	$\eta_{opt,a}$	$LCOH$
SLSQP	Full field	1 938	60.16 %	38.57 \$/MWh$_t$
BFGS	Full field	1 962	56.52 %	39.46 \$/MWh$_t$
Fletcher-Reeves	Full field	1 926	57.23 %	39.40 \$/MWh$_t$

The resulting field layouts for the DOT optimisers are shown in Figure C2. Both DOT fields have a distinct separation between a dense and sparse region. Compared to the relevant SLSQP field (Figure 5.13b) which is mostly densely packed. Interestingly for the DOT fields, the pods in the sparsely packed region are all of maximum or near maximum size. Heliostat's optical performance reduces as the distance between it and the receiver increases. Therefore the optimisation would try to find the best trade-off between high blocking and shading losses for a dense field, with the high attenuation and spillage losses for a sparse field. The DOT optimisers may have reduced the number of heliostats being placed far from the receiver by increasing the pod sizes in theses regions to the maximum. This would limit the number of heliostats possible for these far away rows. The same effect could be achieved by decreasing these rows width's if the pod sizes are smaller, which is how the SLSQP optimiser designed the field.

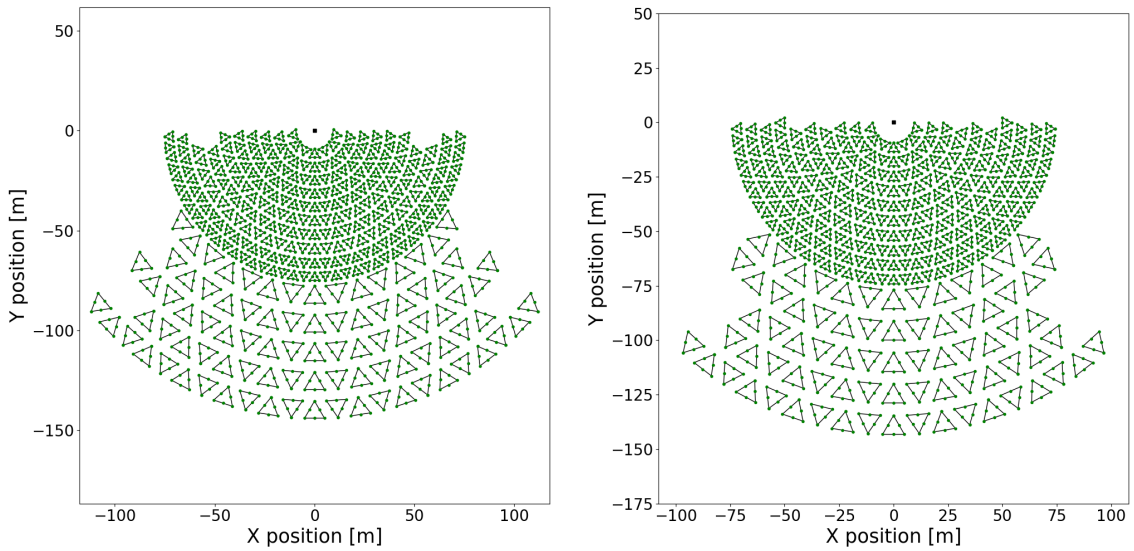

(a) BFGS from full field.

(b) Fletcher-Reeves from full field.

Figure C2: SLSQP field designs for 40 m tower.

C.3. Alpha cuts

To investigate the effect of the two starting values on the results a one-dimensional search is undertaken through the multi-dimensional design space. The search represents a straight line from the starting point to the returned optimum, with a number of steps in between. The purpose of this is to investigate the design space.

Figure C3 shows the objective function results, for a straight line through the multi-dimensional design space, starting at the initial value and ending beyond the returned optimum. An alpha value of zero represents the initial value and a value of one represents the returned optimum. The two curves represent the two start locations; no heliostats and full field. From the figure it can be seen that the starting value of the full field is a much better initial field, the optimisers starts closer to the optimum result. Starting with no heliostats converges to some local minima. Starting with a full field converges to a better result, but this is not guaranteed to be a global optimum. Similar results were seen for all

optimisers.

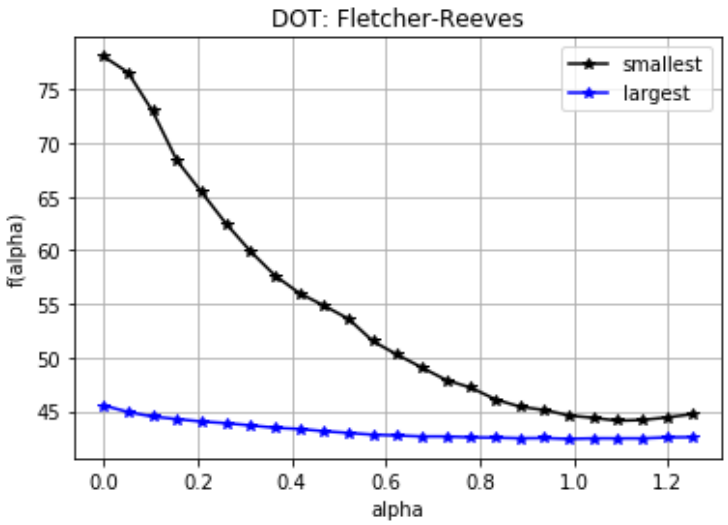

Figure C3: Alpha cut from initial guess to final optimum for the Fletcher-Reeves results.

Appendix D Case study heliostat fields

This chapter provides further detail for the heliostat fields developed for the case study in chapter 6.

D.1. Ten different sized fields

Figure D1 shows the ten fields of varying size designed for the case study using the field layout optimisation methodology developed. The caption for each field provides the thermal power provided by the field at solar noon on equinox, this is an indication of the fields size. A larger thermal power rating at this solar design condition is proportional to more heliostats and more annual collected energy.

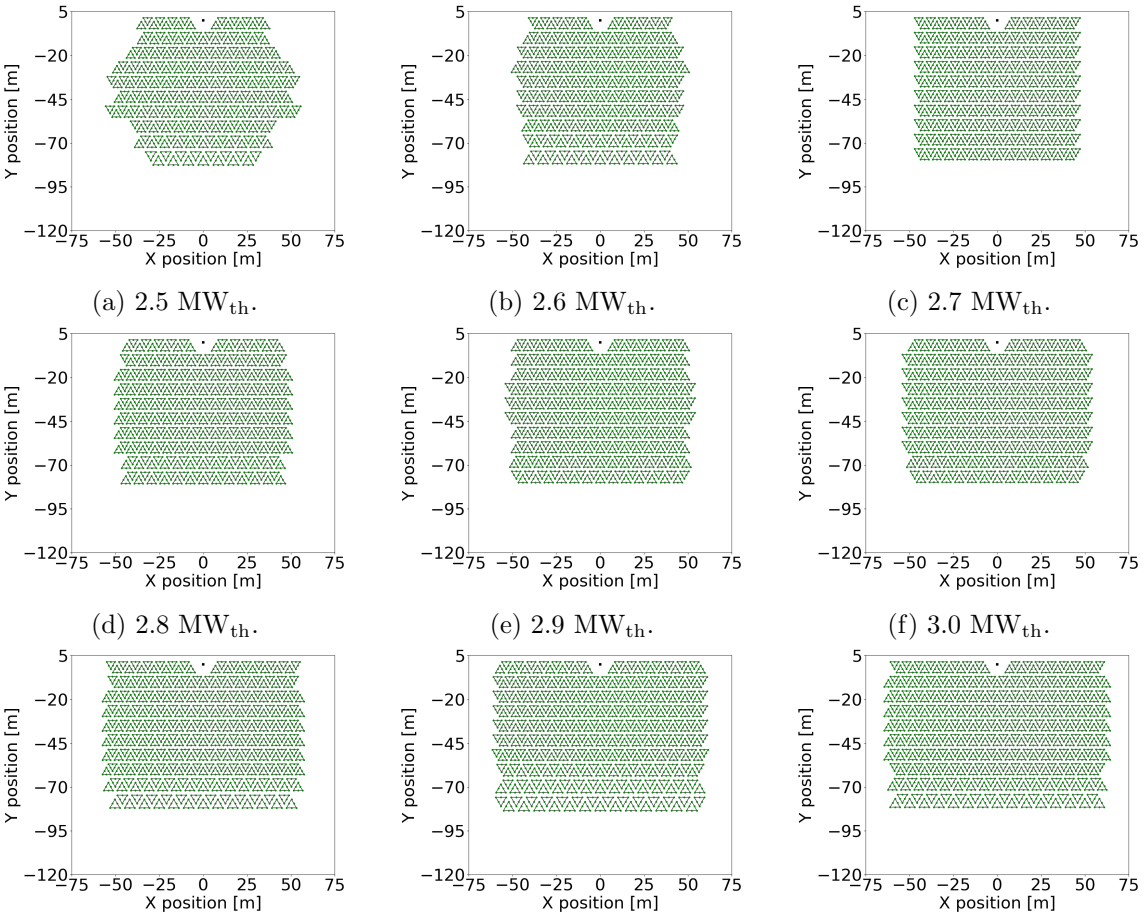

(a) 2.5 MW_{th}. (b) 2.6 MW_{th}. (c) 2.7 MW_{th}.

(d) 2.8 MW_{th}. (e) 2.9 MW_{th}. (f) 3.0 MW_{th}.

(g) 3.1 MW_{th}. (h) 3.3 MW_{th}. (i) 3.5 MW_{th}.

Figure D1: Ten fields designed for the case study.

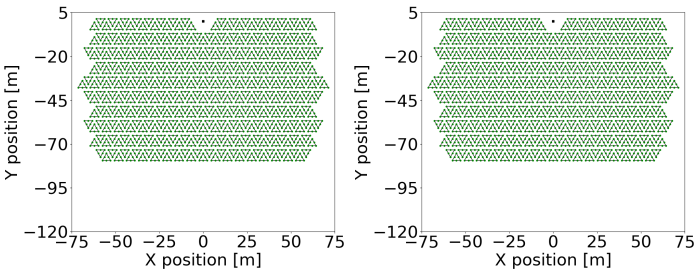

(j) 3.6 MW_{th}. (k) 3.8 MW_{th}.

Figure D1: Ten fields designed for the case study.

D.2. Varying focal lengths in field

From the optical theory of spherical mirrors it is known that the focal length for such a mirror is half it's radius of curvature (Dereniak and Dereniak, 2008). An idealised heliostat field would have every heliostat curved with a radius twice the distance between the heliostat and the receiver (known as slant range) in order to reflect the smallest image possible onto the receiver, thereby reducing spillage. In practise this is not feasible as it requires specialised equipment to manufacture just one curvature of mirror. Therefore heliostat fields have a finite set of focal lengths available for the heliostat field. In order to account for the deviation from the idealised field a simple strategy is developed for selecting focal lengths in the field for the case study. Figure D2 illustrates the parameters defining the reflection of spherical mirrors.

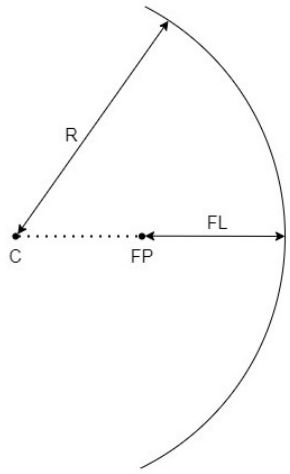

Figure D2: Parameters defining reflection of spherical mirrors; C - sphere center, R - sphere radius, FP - focal point and FL - focal length.

A parametric study was completed to show the effect on the optical and economic performance of the field, by increasing the number of allowed focal lengths in the fields. For the field sized for the case study ten different sets of focal lengths were modelled, each with one extra allowed focal length. The focal lengths were determined as follows for n allowed focal lengths: a bounding sphere with origin at the receiver center and with radius to the

furthest heliostat is determined, this sphere is then divided into n equal width sections, where the width of each section is the sphere radius divided by $n-1$, for each section the focal length is then the average slant range for all heliostats in this section. A parametric study was then completed on the field for a number of different allowed focal lengths. Figure D3 shows the resulting sections for the varying allowed number focal lengths for the 10 row cornfield layout field used in the case study.

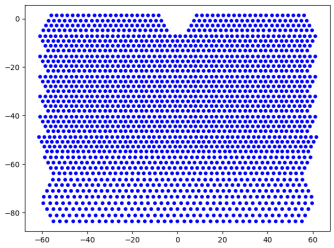

(a) 1 Focal length.

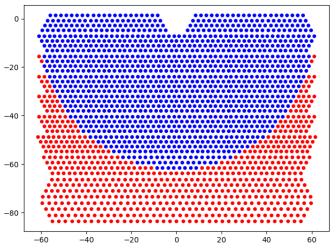

(b) 2 Focal length.

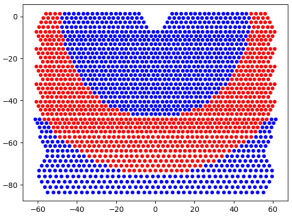

(c) 3 Focal length.

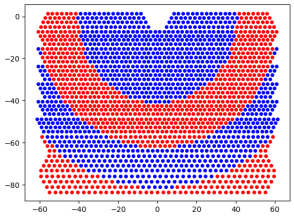

(d) 4 Focal length.

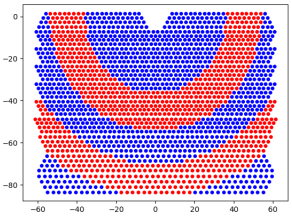

(e) 5 Focal length.

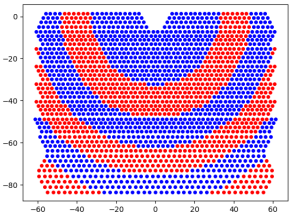

(f) 6 Focal length.

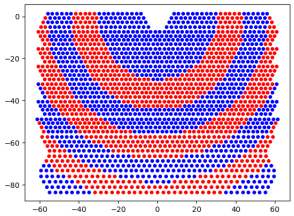

(g) 7 Focal length.

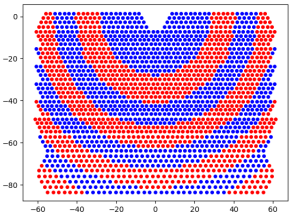

(h) 8 Focal length.

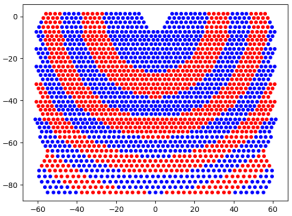

(i) 9 Focal length.

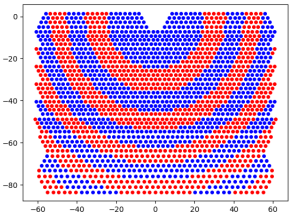

(j) 10 Focal length.

Figure D3: Equal focal length regions shown for a different number of allowed focal lengths. Alternating colours show start/end of new focal length region.

Figure D4 shows the resulting economic performance for the parametric study of allowed number of focal lengths. The figure shows the economic performance for each field with its number of allowed focal lengths. It can be seen as the number of allowed focal lengths

increase the result converges to the ideal case where each mirror has ideal focal length. This study does not include the added cost of manufacturing more focal lengths. However this result can be used to determine the cost-benefit of the improved optical performance (and thereby economic performance) by adding more focal lengths vs the additional cost required for manufacturing tooling.

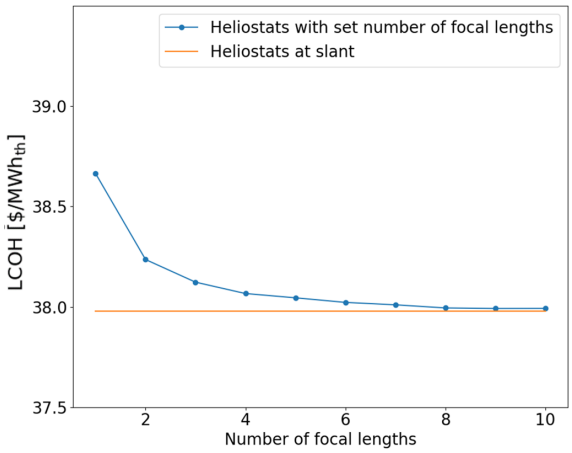

Figure D4: Focal length parametric study.

Appendix E Gradient based optimisers

The optimisation algorithms used in the work are Gradient based optimisers. A general overview of these class of algorithms is provided.

Gradient based optimisers start with a set of initial values, also known as design variables. These design variables are then iteratively updated until some convergence criteria is met. Once convergence is reached this result is taken to be the optimum. There is generally no guarantee this optimum is a global optimum. The iterative process consists of determining a search direction from the current design variable vector and then performing a one-dimensional search along this direction to determine the step-length to the minimum along this search direction. The search direction and step-length are then used to update the design variable vector. After each update the results are checked for convergence. If the result has not converged then the iterative process is repeated. Different gradient based optimisers differ in their approach to determining the search direction. The iterative process is described by Equation 28:

$$x^{k+1} = x^k + \alpha^k s^k, \tag{28}$$

where x is the design variables vector, k is the iteration number, α is the step length and s is the search direction.

The optimisation work in this thesis relies heavily on the use of the SLSQP and MMFD algorithms. Further detail of these algorithms are provided.

The SLSQP algorithm is a modified approach to solving a Sequential Quadratic Programming (SQP) problem. SQP is a method for solving constrained optimisation problems. Lagrangian multipliers are used to formulate a new objective function which incorporates the constraints. The solution to the new problem is determined by meeting the Karush–Kuhn–Tucker conditions. Newton's method is then applied to determine the design variables and Lagrangian multipliers. Each step of this iterative process can be represented by a quadratic problem. This iterative or sequential process is therefore called Sequential Quadratic Programming. Equation 29 shows the formulation of the quadratic sub-problem solved at each Newton step (Snyman, 2005):

$$min\ \frac{1}{2} s^{\mathrm{T}} \mathbf{B}^k s + \nabla^{\mathrm{T}} f(x^k) s + f(x) \tag{29}$$

where $\mathbf{B}$ is the Hessian of the Lagrange function of the optimisation problem. Note the bold text represents a matrix.

SLSQP solves the same problem by replacing the quadratic sub-problem with a linear least squares problem which is solved using a $\mathbf{LDL}^{\mathrm{T}}$ factorisation of $\mathbf{B}$:

$$min\ ||(\mathbf{D}^k)^{1/2}(\mathbf{L}^k)^{\mathrm{T}} s + (\mathbf{D}^k)^{-1/2}(\mathbf{L}^k)^{-1} \nabla f(x^k|| \tag{30}$$

Further details of the SLSQP algorithm can be found in Kraft (1998).

The MMFD algorithm implements and adaptive approach to determining the search direction. The algorithm chooses a search direction for each iteration based on whether

constraints are active or not, and violated or not. If there are no active or violate constraints the search direction is set to the steepest descent (only for iteration 1) or the conjugate search direction. If there are active constraints but no violated constraints the search direction is determined to be parallel to the active constraint. Specifically this is found through a sub-problem of minimizing the cosine between the gradient and the new search direction. If there are violated constraints then the search direction is determined to leave the infeasible region, by heading in the opposite direction of the previous search. In essence MMFD finds a constraint and follows the constraints toward the minimum. Further details of the MMFD algorithm can be found in the DOT manual (Vanderplaats Research and Development, n.d.).

References

A.SPIRE (2019). *Energy efficient, primary production of manganese ferroalloys through the application of novel energy systems in the drying and pre-heating of furnace feed materials.* URL: `www.spire2030.eu/prema` (visited on 2019-12-11).

Abengoa (2020). *Multimedia gallery: Energy.* URL: `www.abengoa.com/web/en/noticias_y_publicaciones/galeria_videos/galeria_imagenes/energia/` (visited on 2020-05-27).

Amsbeck, L, B Behrendt, T Prosin, and R Buck (2014a). "Particle tower system with direct absorbtion centrifugal receiver for high temperature process heat". In: *Proceedings of the SolarPACES International Conference.*

– (2014b). "Particle tower system with direct absorption centrifugal receiver for high temperature process heat". In: *Proceedings of the SolarPACES International Conference.*

Amsbeck, L, R Buck, and T Prosin (2015). "Particle tower technology applied to metallurgic plant and peak-time boosting of steam power plants." In: *Proceedings of the SolarPACES International Conference.*

Amsbeck, L, R Buck, T Rehbock, T Prosin, and P Schwarzbozl (2017). "Solar sludge drying demonstration plant". In: *4th International Symposium on Inovation and Technology in the Phosphate Industry.*

Al-Ansary, H, E Djajadiwinata, A El-Leathy, S Danish, and Z Al-Suhaibani (2014). "Modelling of transient cyclic behavior of a solid particle thermal energy storage bin for central receiver applications." In: *Proceedings of the SolarPACES International Conference.*

Barker, I.J. (2011). "Some considerations on future developments in ferroalloy". In: *Journal of the Southern African Institute of Mining and Metallurgy.*

Blair, Nate, Nicholas Diorio, Janine Freeman, Paul Gilman, Steven Janzou, Ty W. Neises, and Michael J. Wagner (2018). *System Advisor Model (SAM) General Description.* Tech. rep. NREL/TP-6A20-70414. National Renewable Energy Laboratory. URL: `www.nrel.gov/publications`.

Bode, Sebastian-James and Paul Gauché, eds. (2012). *Review of optical software for use in concentrating solar power systems.* Proceedings of South African Solar Energy Conference.

Buie, D., A. G. Monger, and C. J. Dey (2003). "Sunshape distributions for terrestrial solar simulations". In: *Solar Energy* 74.2, pp. 113–122.

Cannon, W.F., B.E. Kimball, and L.A. Coarthers (2017). *Manganese.* Tech. rep. United States Geological Survery. URL: `https://pubs.er.usgs.gov/publication/pp1802L`.

Chamberlain, K (2020). *Abengoa to install first retrofit concentrating solar power storage pilot.* URL: `http://helioscsp.com/abengoa-to-install-first-retrofit-concentrated-solar-power-storage-pilot/` (visited on 2020-06-22).

Collado, Francisco J and Jesus Guallar (2012). "Campo: Generation of regular heliostat fields". In: *Renewable Energy* 46, pp. 49–59.

Collado, Francisco J. and Jesús Guallar (2013). "A review of optimized design layouts for solar power tower plants with campo code". In: *Renewable and Sustainable Energy Reviews* 20, pp. 142–154.

Cruz, N C, J L Redondo, M Berenguel, J D Alvarez, and P M Ortigosa (2017). "Review of software for optical analyzing and optimizing heliostat fields". In: *Renewable and Sustainable Energy Reviews* 72, pp. 1001–1018.

Department Mineral Resources (2016). *South Africa's Mineral Industry 2014/2015*. Tech. rep. Department Mineral Resources. URL: https://www.dmr.gov.za/LinkClick.aspx?fileticket=z2XyeVTH7RE%3D&portalid=0.

Department of Mineral Resources (2013). *South Africa's Manganese Industry Developments 2004-2011*. Tech. rep. URL: https://www.dmr.gov.za/LinkClick.aspx?fileticket=g2xSDGAbOug%3D&portalid=0.

Dereniak, Eustace L. and Teresa D. Dereniak (2008). "8.2 Spherical Mirrors". In: *Geometrical and Trigonometric Optics*. Cambridge University Press, p. 201.

Domínguez-Bravo, Carmen Ana, Sebastian James Bode, Gregor Heiming, Pascal Richter, Emilio Carrizosa, Enrique Fernández-Cara, Martin Frank, and Paul Gauché (2016). "Field-design optimization with triangular heliostat pods". In: *AIP Conference Proceedings* 1734.February 2019.

Duffie, John A and William A Beckman (1991). *Solar engineering of thermal processes*. Wiley New York.

Ebert, M, L Amsbeck, J Rheinlander, A Jensch, J Hertel, D Trebing, R Uhlig, and R Buck (2016). "Upscalling, manufacturing and test of a centrifugal particle receiver". In: *10th international conference on energy sustainability*.

Ebert, M, L Amsbeck, J Rheinlander, B Schlogl-Konthe, S Schmitz, M Sibum, R Uhlig, and R Buck (2018). "Operational experience of a centrifugal particle receiver prototpye". In: *Proceedings of the SolarPACES International Conference*.

Eglinton, Thomas, Jim Hinkley, Andrew Beath, and Mark Dell'Amico (2013). "Potential applications of concentrated solar thermal technologies in the Australian minerals processing and extractive metallurgical industry". In: *JOM* 65.

Eskom (2019). *Tariffs and Charges Booklet 2019/2020*. Tech. rep. Eskom. URL: http://www.eskom.co.za/CustomerCare/TariffsAndCharges/Pages/Tariffs_And_Charges.aspx.

Farjana, Shahjadi Hisan, Nazmul Huda, M A Parvez Mahmud, and R Saidur (2018). "Solar process heat in industrial systems A global review". In: *Renewable and Sustainable Energy Reviews* 82, pp. 2270–2286.

Glance, A T A (2011). *Coalinga at a glance*. Tech. rep. URL: http://www.brightsourceenergy.com/coalinga%7B%5C#%7D.XvdRQSgzaHs.

Guedez, Rafael, Monika Topel, Ines Conde, Francisco Ferragut, Irene Callaba, James Spelling, Zhor Hassar, Carlos David Perez-Segarra, and Bjorn Laumert (2016). "A Methodology for Determining Optimum Solar Tower Plant Configurations and Operating Strategies to Maximize Profits Based on Hourly Electricity Market Prices and Tariffs". In: *Journal of Solar Energy Engineering, Transactions of the ASME* 138.2, pp. 1–12.

Ho, Clifford (2016). "A review of high-temperature particle receivers for concentrating solar power". In: *Applied Thermal Engineering* 109, pp. 958–969.

Ho, Clifford K. (2017). "Advances in central receivers for concentrating solar applications". In: *Solar Energy* 152, pp. 38–56.

Ho, Clifford K. and Brian D. Iverson (2014). "Review of high-temperature central receiver designs for concentrating solar power". In: *Renewable and Sustainable Energy Reviews* 29, pp. 835–846.

Hockaday, Lina (2019). "Solar thermal applications in minerals processing in South Africa." In: *Proceedings of the 6th South African Solar Energy Converence*.

Hockaday, Lina, Tristan McKechnie, Martina Neises von Puttkamer, and Matti Lubkoll (2020). "The Impact of Solar Resource Characteristics on Solar Thermal Pre-heating of Manganese Ores". In: *Energy Technology 2020: Recycling, Carbon Dioxide Management, and Other Technologies*. Cham: Springer International Publishing, pp. 3–13.

Hockaday, S A C, F Dinter, and T M Harms (2016). "Opportunities for concentrated solar thermal heat in the minerals processing industry". In: *4th Southern African Solar Energy Conference (SASEC) 2016*.

Hockaday, S A C, F Dinter, Thomas M Harms, and Matti Lubkoll (2018). "Barriers to introducing solar thermal heat into minerals processing: A case study on replacing a diesel burner at a sinter plant". In: *Proceedings of SASEC 2018 (submitted)*.

Hogan, Barbara (2010). *Eskom's top hundred users•*. URL: `https://www.politicsweb.co.za/party/eskoms-top-hundred-users` (visited on 2019-07-30).

IRENA (2020). *Renewable Power Generation Costs in 2019*. Report. International Renewable Energy Agency.

Islam, Md Tasbirul, Nazmul Huda, A. B. Abdullah, and R. Saidur (2018). "A comprehensive review of state-of-the-art concentrating solar power (CSP) technologies: Current status and research trends". In: *Renewable and Sustainable Energy Reviews* 91.April, pp. 987–1018.

Jafrancesco, David, Joao P Cardoso, Amaia Mutuberria, Erminia Leonardi, Inigo Les, Paola Sansoni, Franco Francini, and Daniela Fontani (2018). "Optical simulation of a central receiver system: Comparison of different software tools". In: *Renewable and Sustainable Energy Reviews* 94.

Jiang, Kaijun, Xiaoze Du, Yanqiang Kong, Chao Xu, and Xing Ju (2019). "A comprehensive review on solid particle receivers of concentrated solar power". In: *Renewable and Sustainable Energy Reviews* 116.October, p. 109463.

Kotzé, Johannes P., Philip Du Toit, Sebastian J. Bode, James N. Larmuth, Willem A. Landman, and Paul Gauché (2016). "Solar augmentation for process heat with central receiver technology". In: *AIP Conference Proceedings* 1734.

Kraft, Dieter (1998). *A Software Package for Sequential Quadratic Programming*. Technical Report. Deutsche Forschungs und Versuchsanstalt fur Luft-und Raumfahrt.

Kuravi, Sarada, Jamie Trahan, D Yogi Goswami, Muhammad M Rahman, and Elias K Stefanakos (2013). "Thermal energy storage technologies and systems for concentrating solar power plants". In: *Progress in Energy and Combustion Science* 39.4, pp. 285–319.

Laplace Conceil (2013). "Impacts of energy market developments on the steel industry". In: *74th Session of the OECD Steel Committee*.

Larmuth, James N., Willem A. Landamn, and Paul Gauché (2016). "A top-down approach to heliostat cost reduction". In: *AIP Conference Proceedings* 1734.

Lauterbach, C, B Schmitt, U Jordan, and K Vajen (2012). "The potential of solar heat for industrial processes in Germany". In: *Renewable and Sustainable Energy Reviews* 16.7, pp. 5121–5130.

El-Leathy, A, S Jeter, H Al-Ansary, S Abdel-Khalik, J Roop, M Golob, S Danish, A Alrished, E Djajadiwinata, and Z Al-Suhaibani (2013). "Experimental study of heat loss from a thermal energy storage system for use with a high-temperature falling particle receiver system". In: *Proceedings of the SolarPACES International Conference*.

Lipps, F. W. and L. L. Vant-Hull (1978). "A cellwise method for the optimization of large central receiver systems". In: *Solar Energy* 20.6, pp. 505–516.

Liu, Ming, N. H. Steven Tay, Stuart Bell, Martin Belusko, Rhys Jacob, Geoffrey Will, Wasim Saman, and Frank Bruno (2016). "Review on concentrating solar power plants and new developments in high temperature thermal energy storage technologies". In: *Renewable and Sustainable Energy Reviews* 53, pp. 1411–1432.

Lovegrove, Keith and Wes Stein (2012). *Concentrating solar power technology : principles, developments and applications*. Cambridge, UK : Woodhead.

Lubkoll, M, S. A. C. Hockaday, T. M. Harms, T. W. von Backström, L Amsbeck, and R Buck (2018). "Integrating solar process heat into manganese ore pre-heating". In: *Southern African Solar Energy Conference, Durban, South Africa, 25 – 27 June*.

Lutchman, S L, A A Groenwold, P Gauche, and S Bode (2014). "On Using a Gradient-based Method for Heliostat Field Layout". In: *Proceedings of the SolarPACES International Conference*, pp. 1429–1438.

Madaeni, S H, R Sioshansi, and P Denholm (2012a). "How Thermal Energy Storage Enhances the Economic Viability of Concentrating Solar Power". In: *Proceedings of the IEEE* 100.2, pp. 335–347.

– (2012b). "How thermal energy storage enhances the economic viability of concentrating solar power". In: *Proceedings of the IEEE*.

Mahony, C.S. and J.M. Baartmanm (2018). "Tariff developments for electricity intensive industry in South Africa". In: *Journal of the Southern African Institute of Mining and Metallurgy*.

Mckechnie, Tristan, Craig McGregor, and Gerhard Venter (June 2020). "Concentrating Solar Thermal Process Heat for Manganese Ferroalloy Production: Plant Modelling and Thermal Energy Storage Dispatch Optimization". In: vol. ASME 2020 14th International Conference on Energy Sustainability. Energy Sustainability. V001T14A001. URL: https://doi.org/10.1115/ES2020-1635.

Mehos, Mark, Craig Turchi, Judith Vidal, Michael Wagner, Zhiwen Ma, Clifford Ho, William Kolb, Charles Andraka, and Alan Kruizenga (2017). "Concentrating Solar Power Gen3 Demonstration Roadmap". In: *Nrel/Tp-5500-67464* January, pp. 1–140. URL: https://www.nrel.gov/docs/fy17osti/67464.pdf%7B%5C%%7D0Ahttp://www.nrel.gov/docs/fy17osti/67464.pdf.

Meteotest (n.d.). *Meteonorm Software*. URL: https://meteonorm.com/en/.

Mutuberria, A., J. Pascual, M. V. Guisado, and F. Mallor (2015). "Comparison of Heliostat Field Layout Design Methodologies and Impact on Power Plant Efficiency". In: *Energy Procedia* 69, pp. 1360–1370.

National Renewable Energy Laboratory (2015). *SolarPILOT's user manual*.

– (2020a). *Gemasolar thermalsolar plant*. URL: solarpaces.nrel.gov/gemasolar-thermosolar-plant (visited on 2020-03-26).

– (2020b). *Ivanpah Solar Electric Generating System*. URL: https://solarpaces.nrel.gov/ivanpah-solar-electric-generating-system (visited on 2020-06-22).

– (2020c). *Planta Solar 10*. URL: solarpaces.nrel.gov/planta-solar-10 (visited on 2020-03-26).

Nithyanandam, K. and R. Pitchumani (2014). "Cost and performance analysis of concentrating solar power systems with integrated latent thermal energy storage". In: *Energy* 64, pp. 793–810.

Noone, Corey J, Manuel Torrilhon, and Alexander Mitsos (2012). "Heliostat field optimization: A new computationally efficient model and biomimetic layout". In: *Solar Energy* 86.2, pp. 792–803.

Oliphant, T E (2007). *Python for Scientific Computing*.

Palacios, A, C Barreneche, M E Navarro, and Y Ding (2019). "Thermal energy storage technologies for concentrated solar power A review from a materials perspective". In: *Renewable Energy*.

REN21 (2018). *Advancing the global renewable energy transistion*. Tech. rep. Renewable energy policy network for the 21st Century. URL: `http://www.ren21.net/GSR`.

Richter, Pascal, Gregor Heiming, Nils Lukas, and Martin Frank (2018). "SunFlower: A new solar tower simulation method for use in field layout optimization". In: *AIP Conference Proceedings*. Vol. 2033. 1. AIP Publishing LLC, p. 210015.

Ricklin, P., M. Slack, D. Rogers, and R. Huibregtse (2014). "Commercial readiness of eSolar next generation heliostat". In: *Energy Procedia* 49, pp. 201–208.

Sánchez, Marcelino and Manuel Romero (2006). "Methodology for generation of heliostat field layout in central receiver systems based on yearly normalized energy surfaces". In: *Solar Energy* 80.7, pp. 861–874.

Short, Walter, Daniel J Packey, and Thomas Holt (1995). *A manual for the economic evaluation of energy efficiency and renewable energy technologies*. URL: `https://www.nrel.gov/docs/legosti/old/5173.pdf`.

Sioshansi, Ramteen and Paul Denholm (2010). "The value of concentrating solar power and thermal energy storage". In: *IEEE Transactions on Sustainable Energy* 1.3, pp. 173–183.

Sithole, N.A, N Rambuda, J.D. Steenkamp, D.A. Hayman, and C Hockaday (2018). "Silicomanganese production at Mogale Alloys". In: *Journal of the Southern African Institute of Mining and Metallurgy*.

Snyman, Jan A (2005). *Practical mathematical optimization*. Springer.

SolarGIS (2019). *Global Solar Atlas*. URL: `https://globalsolaratlas.info` (visited on 2019-04-20).

South Africa Department of Energy (2019). *Integrated resource plan*.

Stats SA (2018). *Statistical release P0441: Gross domestic product*.

Steenkamp, J.D., W.G. Bam, E Ringdalen, M Mushwana, S.A.C. Hockaday, and N.A. Sithole (2018a). "Working towards an increase in manganese ferroalloy production in South Africa - a research agenda". In: *Journal of the Southern African Institute of Mining and Metallurgy*.

Steenkamp, J.D. and J. Basson (2013). "The manganese ferroalloys industry in southern Africa". In: *Journal of the Southern African Institute of Mining and Metallurgy* 113.8, pp. 667–676.

Steenkamp, J.D., C.J. Hockaday, and J.P. Gous, eds. (2016). *Analysis of electrical energy dissipation in submerged arc furnaces producing silicomanganese*.

Steenkamp, J.D., P Maphutha, O Makwarela, W.K. Banda, I Thobadi, M Sitefine, J Gous, and J.J. Sutherland (2018b). "Silicomanganese production at Transalloys in the twenty-tens". In: *Journal of the Southern African Institute of Mining and Metallurgy*.

Stine, W B and M Geyer (2001). *Power from the sun*. URL: `http://www.powerfromthesun.net/book.html`.

Tangstad, M, K Ichihara, and E Ringdalen, eds. (2015). *Pretreatment unit in ferromanganese production*.

Taylor, Alan (2014). *The Ivanpah Solar Electric Generating System*. URL: `www.theatlantic.com/photo/2014/03/the-ivanpah-solar-electric-generating-system/100692/` (visited on 2020-05-27).

Transnet (2017). *Transet long term planning framework*. URL: www.transnet.net/BusinessWithUs/ (visited on 2019-12-05).

– (2018). *Freight Rail 2018*. URL: https://www.transnet.net/InvestorRelations/AR2018/TFR.pdf (visited on 2019-12-05).

Tupkary, R.H. and V.R. Tupkary (2018). *Modern Iron Making Handbook*. Mercury Learning and Information.

Uhlig, R, L Amsbeck, R Buck, B Grobereit, and P Schwarzbozl (2015). "Potential high temperature industrial process heat applications for concentrating solar technology in South Africa." In: *South African Solar Energy Conference*, pp. 537–542.

USGS (n.d.). *Manganese Statistics and Information*. URL: https://www.usgs.gov/centers/nmic/manganese-statistics-and-information.

van Zyl, H.J., W.G. Bam, and J.D. Steenkamp, eds. (2016). *Indentifying barriers faced by key role players in the South African Manganese industry*.

Vanderplaats Research and Development (n.d.). *DOT optimization*. URL: http://www.vrand.com/products/dot-optimization/.

Wagner, Michael J (2015). "Optimization of stored energy dispatch for concentrating solar power systems". PhD. Colorado School of Mines.

Wagner, Michael J and Tim Wendelin (2018). "SolarPILOT: A power tower solar field layout and characterization tool". In: *Solar Energy* 171, pp. 185–196.

Wittmann, M, M Eck, T Hirsch, and R Pitz-Paal (2008). "Theoretical Economic Potential of the Spanish Premium Tariff for Solar Thermal Power Plants". In: *Proceedings of the SolarPACES International Conference*. MARCH, p. 8.

Wu, W, L Amsbeck, R Buck, R Uhlig, and R Ritz Paal (2013). "Proof of concept test of a centrifugal particle receiver". In: *Proceedings of the SolarPACES International Conference*.

Wu, W, D Trebing, L Amsbeck, R Buck, and R Ritz Paal (2015a). "Prototype testing of a centrifugal particle receiver for high-temperature concentrating solar applications". In: *Journal of Solar Energy Engineering*.

Wu, W, R Uhlig, R Buck, and R Pitz-Paal (2015b). "Numerical simulation of a centrifugal particle receiver for high-temperature concentrating solar applications". In: *Numerical heat transfer, Part A: Applications*.